Creation of ultracold polar ground-state RbCs molecules

MOLONY, PETER,KENNETH

MOLONY, PETER,KENNETH (2016) *Creation of ultracold polar ground-state RbCs molecules* , Durham theses, Durham University. Available at Durham E-Theses Online: http://etheses.dur.ac.uk/11781/

Creation of ultracold polar ground-state RbCs molecules

Peter Kenneth Molony

A thesis submitted in partial fulfilment
of the requirements for the degree of
Doctor of Philosophy

Department of Physics
Durham University

October 13, 2016

Creation of ultracold polar ground-state RbCs molecules

Peter Kenneth Molony

Abstract

This thesis reports the creation and trapping of ^{87}RbCs molecules in the absolute ground state with a temperature of 1 μK.

We build a tunable narrow-linewidth laser system at 1550 nm and 980 nm, using a single high-finesse optical cavity as a reference for both colours. We use fibre-coupled electro-optic modulators to continuously tune both lasers. These allow a novel measurement of the free spectral range of the cavity to better than 1 part in 10^6.

We perform one- and two-photon spectroscopy on ^{87}RbCs Feshbach molecules and identify a suitable intermediate state for transfer to the molecular ground state. We measure the electric dipole moment of the molecular ground state as 1.225(3)(8) D, and demonstrate the highest lab-frame dipole moment of any ultracold molecular system at the time of measurement.

We transfer the molecules to the electronic, rovibrational and hyperfine ground state using stimulated Raman adiabatic passage, with 88% efficiency. We measure the transition strengths and excited state linewidth for this transfer route. We develop a model for the transfer which includes the effect of laser linewidth, and find excellent agreement with experimental data. The molecular sample is trapped in an optical dipole potential, and has a lifetime of 0.89(6) s.

We reference the STIRAP lasers to a novel design of frequency comb which uses difference frequency generation to cancel the carrier-envelope offset. We use this to measure the binding energy of the molecules as $h \times 114\,268\,135.24(4)(3)$ MHz. To our knowledge, this is the most precise determination of the dissociation energy of a molecule to date.

Finally, we report progress toward loading the molecules into a 1D optical lattice at 1064 nm. We develop the tools and methods to characterise a lattice, and demonstrate trapping of Feshbach molecules in both a 1D optical lattice and a harmonic optical potential at 1064 nm.

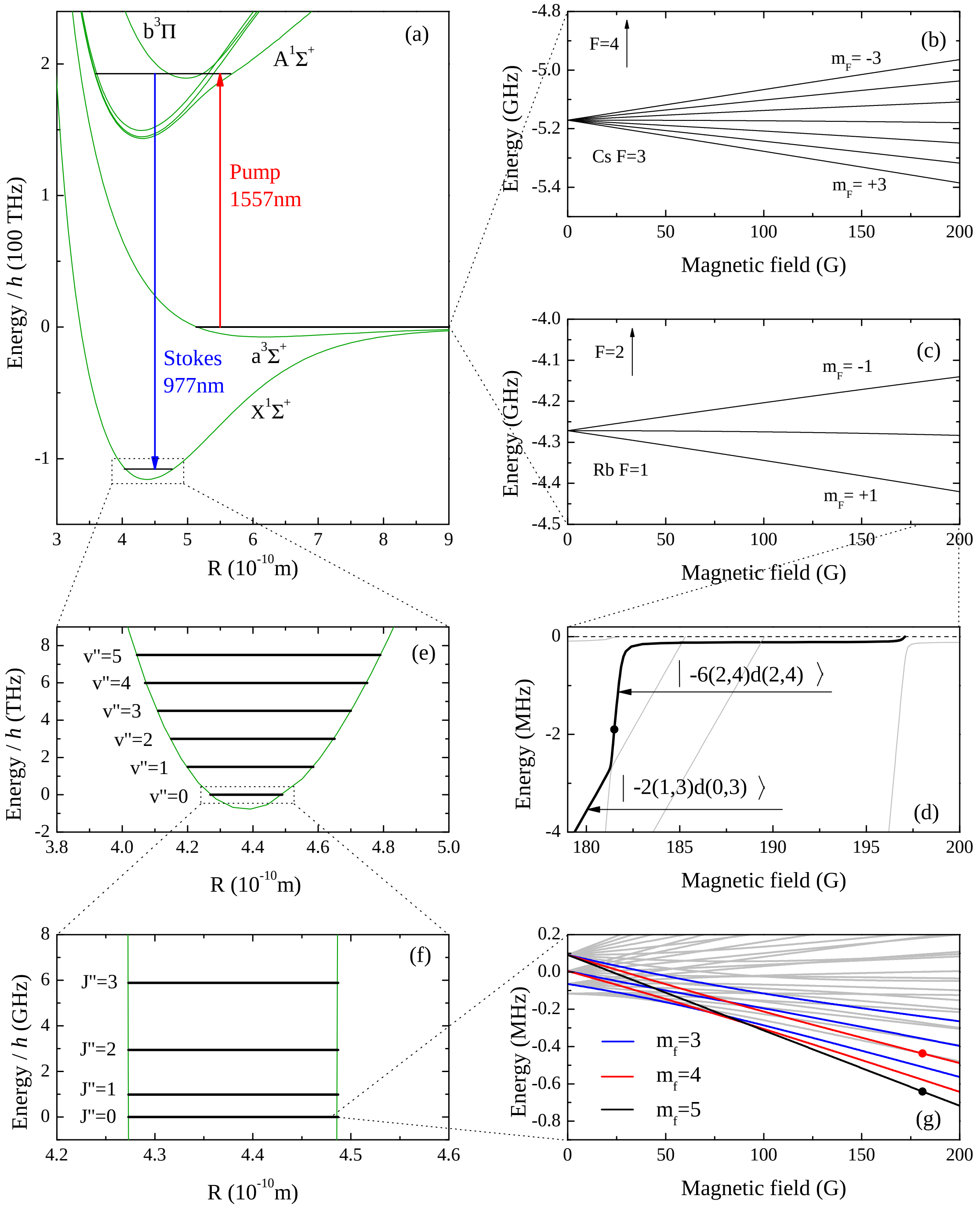

Summary of the relevant energy levels in the RbCs molecule. The initial and final states of the STIRAP transfer are marked with dots. (a) Interatomic potentials and STIRAP laser wavelengths. (b) and (c) The Cs and Rb Breit-Rabi diagrams. The Cs $F = 4$ and Rb $F = 2$ states are not shown. (d) Feshbach states, relative to the combined ^{87}Rb $|F = 1, m_F = 1\rangle$ and Cs $|3, 3\rangle$ energies. (e) Vibrational structure in the $X^1\Sigma^+$ electronic ground state. (f) Rotational levels of the $v'' = 0$ state. (g) Hyperfine and Zeeman structure of the rovibrational ground state.

Declaration

I confirm that no part of the material offered has previously been submitted by myself for a degree in this or any other University. Where material has been generated through joint work, the work of others has been indicated.

Peter Kenneth Molony
Durham, October 13, 2016

All the data from this thesis is available at **doi:10.15128/r2gx41mh85n**.

To Helen, Aidan, Steven and Helen,
for keeping me sane(ish).

Acknowledgements

It is difficult to sum up the emotional thunderstorm that is a PhD. One calls to mind a ship in the southern ocean, or swimming in Niagara Falls. My time in the RbCs lab has been defined by ecstatic highs, usually when we found some exciting new results, and crashing lows when lasers broke or FETs burned out. We usually found the experiment got tired at the end of the day, or ran better after a long break, so making it work every day often felt like persuading a petulent child to do their homework.

Helping me navigate the high seas of experimental physics over the last four years, I have had many wonderful colleagues. My supervisor, Simon Cornish, has been an invaluable help. I have learned much from his guidance and his dedication to physics. I must also thank him, along with Phil Gregory, Ana Rakonjak and Steve Hopkins, for proofreading various drafts of this thesis. Danny McCarron, Bo Lu and Avinash Kumar have all been a great help during their time here. Zhonghua ("Dr Ji") brought with him a relentless enthusiasm that helped me cope with some of the lowest points on my experimental voyage. Eighteen months working with Michael Köppinger were some of the most entertaining of my life. Finally, Phil Gregory's eternally calm, unflappable demeanor and fantastic eye for experimental detail have made him a pleasure to work with.

My thanks go to everyone else in the Cornish section. Stefan, Steve, Kirsteen and Alex; Anna, Ana, Tim, Manfred, and Oliver; all have been wonderful to work alongside. The (original) cake club has shown me many delicious and wonderful ideas, and it is a fantastic way to keep up to date with the other experiments. My baking skills have certainly improved in four years.

AtMol have been a wonderful group to work with. Simon Ball, Mark Zentile, Theodora Ilieva, Kate Whittaker, and Rob Bettles stand out for keeping me sane and dragging me to morning coffee. Ifan's advice on error analysis, the nature of Physics and academic life in general have been fascinating. I must thank Tommy Ogden for writing the core of the STIRAP simulation, and I advise him never to look at what I have done to his beautiful code. I would like to thank Matthew Jones and his group for providing the Sr reference for the wavemeter calibrations. I am extremely grateful for the support and patience of Steve Lishman and everyone

in the mechanical workshop. I hope my ridiculously complex designs didn't annoy you too much!

I owe many thanks to the wonderful housemates I have found over the last four years, Mim, Jess, Nic, Taras, Julia and particularly Chris Wade, who has stopped me panicking through several house disasters, and has coped remarkably well with the floods that have befallen his time in Durham.

My time in Durham could not have been so fun without the continual company of the lovely, crazy people of the University caving club. The weekly trips to the pub have helped to keep me sane, and there is nothing better for forgetting the experimental woes than abseiling down a freezing waterfall with daylight four hours away.

My life has been made infinitely better by Ellie Heyworth, my wonderful girlfriend who has kept me company for the last 18 months of my PhD. Thank you for being the best friend I've ever had.

But most of all I thank my Mum and Dad,
For twenty-seven years of love and care.
Three hundred miles away and ever close,
You owed me naught, and gave me all you had.

Contents

Published work

The following publications were prepared during the work for this thesis. The principal chapters corresponding to each paper are indicated as appropriate.

P. K. Molony *et al.*, *Measurement of the binding energy of ultracold* ^{87}Rb^{133}Cs *molecules using an offset-free optical frequeny comb*, Phys. Rev. A **94**, 022507 (2016).
Chapter 6

P. K. Molony *et al.*, *Production of* ^{87}RbCs *in the absolute ground state: complete characterisation of the STIRAP transfer*, Accepted for publication in ChemPhysChem, DOI: 10.1002/cphc.201600501
Chapter 5

P. D. Gregory *et al.*, *A simple, versatile laser system for the creation of ultracold ground state molecules*, New J. Phys. **17**, 055006 (2015).
Chapters 3 and 4

P. K. Molony *et al.*, *Creation of Ultracold* ^{87}Rb^{133}Cs *Molecules in the Rovibrational Ground State*, Phys. Rev. Lett. **113**, 255301 (2014).
Chapters 4 and 5

M. P. Köppinger *et al.*, *Production of optically trapped* ^{87}RbCs *Feshbach molecules*, Phys. Rev. A **89**, 033604 (2014).

Chapter 1

Introduction

The quest for ultracold samples of trapped polar molecules has attracted considerable attention over the last decade [1, 2]. The permanent electric dipole moments of polar molecules give rise to anisotropic, long-range dipole-dipole interactions which can be tuned by applied electric fields [3]. This property, combined with the exquisite control of ultracold systems, offers exciting prospects in the fields of quantum controlled chemistry [4–6], precision measurement [7–9], quantum computation [10] and quantum simulation [11, 12].

Making cold molecules is a difficult task with no obvious best approach. Direct laser cooling is beginning to show results [13–16], and recent work with microwave rotational cooling [17] and Sisyphus cooling [18] may lead to large trapped samples. However, none of these techniques are currently close to achieving the sub-μK temperatures which are needed to enter the “quantum regime” where only one partial wave contributes to the molecule-molecule dynamics [19].

To reach such low temperatures, the most successful approach so far is to associate ultracold atoms into weakly bound molecules on a Feshbach resonance [20, 21], followed by transfer to the ground state by stimulated Raman adiabatic passage (STIRAP) [22]. Several groups have had success with homonuclear alkali molecules [23–25], but the symmetry of these molecules means they have no dipole moment in the ground state, so considerable work is focussed on making heteronuclear molecules. Pioneering experiments with ^{40}K^{87}Rb molecules have led to a series of ground-breaking studies of quantum state-controlled chemistry [4], spin-lattice models [26] and strongly-interacting many-body dynamics [27]. However, ground-state KRb molecules are energetically unstable as the exchange reaction $2\text{KRb} \rightarrow \text{Rb}_2 + \text{K}_2$ is exothermic [4] and this leads to fast molecule loss [28], unless the molecules are confined in a 3D lattice [29].

There are many methods and techniques being developed to produce ultracold molecules [19]. These can be roughly divided into two categories: direct methods where high-temperature molecules are trapped and cooled, and indirect methods where atoms in a precooled mixture are associated into molecules. Here we give an overview of the main methods and most prominent experiments.

1.1 Direct cooling methods

Direct cooling methods are an attractive approach, as they offer potentially much larger samples than have so far been created with indirect methods. They can also be applied to a very different and often broader range of molecules. However, no direct cooling method has so far reached the sub-μK temperatures which have been achieved with indirect methods. We will now look briefly at the most promising methods for direct cooling of molecules.

1.1.1 Laser cooling molecules

Laser cooling of neutral atoms is well understood [30], and has been achieved for a wide variety of atomic species. It relies on the cooling transition being closed, i.e. excited state atoms decay only to the initial state. Such transitions are available in a variety of atomic species, and have been used to cool all the stable, naturally-occuring alkali metals to a Bose-Einstein condensate or quantum degenerate Fermi gas. This method is difficult to extend to molecules because they do not have closed transitions [31]. This is because molecules can rotate and vibrate: the rovibrational levels of a molecule mean there are many more levels to address, and the lack of selection rules between the vibrational levels mean it is difficult to find closed or nearly-closed transitions suitable for laser cooling. Suitable candidate molecules must have a highly-diagonal Franck-Condon array, where the spontaneous emission rates for $v' = 0 \rightarrow v'' = 1, 2, 3, ...$ are much lower than for $v' = 0 \rightarrow v'' = 0$. Even then, many repump lasers are needed to return molecules from the $v'' = 1, 2, 3...$ to the $v' = 0 \rightarrow v'' = 0$ transition. For example, the recent demonstration of a magneto-optical trap of strontium monofluoride [13] needed three vibrational repumping lasers, each with numerous RF sideband frequencies to address the hyperfine and Zeeman structure of the vibrational levels, to scatter 10^6 photons on the cooling transition. Despite this, a number of diatomic species have been proposed as suitable for laser cooling [31].

To date, only SrF has been cooled in a 3D magneto-optical trap (MOT) [13], to a temperature of 400 μK. This method further requires the use of rapidly alternating magnetic field gradients and laser polarisations to destabilise optical dark states [15]. CaF has been slowed in a molecular beam [16] to near the capture velocity of a MOT [32]. YO has been cooled in a 2D MOT configuration [33] and has a narrow-line transition which may be able to cool the molecules to ~ 10 μK [34].

1.1.2 Other cooling methods

Aside from direct laser cooling, several other cooling and trapping techniques are beginning to show results. Microstructured electrostatic traps have trapped large samples of 10^8 fluoromethane molecules (CH_3F) with a lifetime of 12.2(2) s [35]. The same experimental setup has been used with formaldehyde molecules (H_2CO), and combined with optoelectrical Sisyphus cooling to trap 3×10^5 molecules at a temperature of 420 μK [36]. Sympathetic cooling of molecules by laser-cooled atoms such as Li or Rb has also been suggested as a widely applicable method [37, 38].

1.2 Indirect cooling methods

Currently, the coldest molecules and highest phase-space densities have been made by indirect methods. The details vary, but all are based on the same idea: the constituent atoms are cooled with established methods, and then associated into weakly-bound molecules and transferred to the ground state (or some other stable state). This class of techniques has the advantage that atomic cooling methods are well-established, at least for the alkali metals and a few other species [39], and thus it is relatively easy to reach μK temperatures. However, these indirect methods have several disadvantages. First, the constituent atoms must be amenable to cooling with known techniques such as magneto-optical traps and evaporative cooling. This means the range of molecular species is limited, principally to diatomics made from alkali metals and alkaline-earth-like species. Second, if the atoms are cooled below the recoil temperature, the molecules must be associated and transferred to the ground state using coherent methods, to avoid heating from spontaneous emission.

Photoassociation

The most successful methods to bind cold atoms into molecules so far are magnetoassociation and photoassociation. Photoassociation uses a high-power laser to drive transitions from unbound atomic states to electronically excited bound molecular states. These molecules then decay into lower-lying electronic and vibrational states, or are driven into them using a second laser frequency [40, 41]. Associating from a MOT, this has been done for numerous species including LiCs [42], LiRb [43–45], NaCs [46], KRb [47] and YbRb [48]. ^{41}K^{87}Rb molecules were photoassociated from a magneto-optical trap and allowed to decay into the $X^1\Sigma^+$ electronic state. They were then coherently transferred to the rovibrational ground state using STIRAP [49]. However, when associated from a MOT, the molecules are no longer trapped and quickly escape, which makes it difficult to study the dipolar properties of the molecules.

The technique has been particularly effective for ^{85}RbCs, where a large fraction (7%) of the excited-state molecules decay into a long-lived triplet state ($a^1\Sigma^+$, $v = 37$) [50]. These were held in a quasi-electrostatic trap with a lifetime of 400 ms at a temperature of 250 μK [51]. The triplet molecules have also been optically transferred to the $X^1\Sigma^+$ vibrational ground state [52].

Magnetoassociation

The method we use in this thesis, and the best indirect method so far to create trapped ultracold molecules, is magnetoassociation on a Feshbach resonance [20]. The constituent atoms are first cooled to high phase-space density, and then the magnetic field is ramped down across a magnetic Feshbach resonance. These resonances have been studied extensively in a wide range of homonuclear and heteronuclear atomic mixtures [19], and have led to the creation of a BEC of weakly-bound homonuclear molecules [53–55]. Homonuclear molecules were first associated in 2003 with Li_2 [56–58], Na_2 [59], K_2 [60], Rb_2 [61] and Cs_2 [62]. Heteronuclear molecules have been associated from ultracold mixtures to form KRb [63], LiK [64, 65], ^{87}RbCs [66, 67], NaK [68], NaLi [69] and NaRb [70].

1.2.1 Transfer to the ground state

The Feshbach molecules created by magnetoassociation occupy states near the dissociation threshold, and are weakly bound by only a few MHz. The large internuclear separation also means there is very little charge transfer between the constituent atoms in these molecules. Thus the molecules have a negligible electric dipole moment [71]. It is thus necessary to transfer the molecules to a more stable deeply-bound state, and preferably the absolute electronic, vibrational, rotational and hyperfine ground state. The large binding energy of the ground state, which is usually ~ 100 THz, means that the transfer must use a coherent method such as STIRAP to avoid heating the sample.

Homonuclear molecules

To create homonuclear molecules only one atomic species needs to be cooled, so it is experimentally simpler to reach the high phase-space densities that are required for efficient association [20]. However, homonuclear molecules have no electric dipole moment, so they cannot be used to study the anisotropic, long-range, tunable interactions that make heteronuclear molecules an interesting topic [3].

Coherent transfer to the rovibrational ground state has been achieved for several bialkali homonuclear species. Rb_2 molecules were transferred to the ground state of the triplet potential using STIRAP [25], while Cs_2 was transferred to the singlet ground state using two successive stages of STIRAP [23, 24]. Both were confined in a 3D lattice. Sr_2 has been photoassociated into the electronic ground state, using STIRAP from a BEC of ^{84}Sr confined in a 3D lattice [72].

Heteronuclear molecules

The principal attraction of ultracold heteronuclear molecules is the fact that most such molecules have a large permanent electric dipole moment [19]. The degeneracy of the rotational states means this dipole moment must be induced in the lab frame by an applied electric field (see section 4.4.3 for a full description) or by creating a superposition of opposite-parity states [26]. In many cases this critical field is low enough that we can induce a substantial dipole moment with experimentally obtainable fields. Table 1.1 shows the theoretical dipole moments, rotational constants and critical fields for all the heteronuclear bialkali molecules.

	d_0 (D)	B_0 (GHz)	E_{crit} (kV cm^{-1})	Chemically stable?
RbCs	1.26	0.51	0.80	Y
KRb	0.62	1.16	3.74	N
KCs	1.92	0.90	1.0	Y
NaK	2.75	2.85	2.0	Y
NaRb	3.33	2.10	1.3	Y
NaCs	4.60	1.74	0.7	Y
LiNa	0.53	11.22	36.1	N
LiK	3.50	7.68	4.3	N
LiRb	4.13	6.45	3.1	N
LiCs	5.48	5.61	2.0	N

Table 1.1: Theoretical dipole moments (d_0), rotational constants (B_0) and critical electric fields (E_{crit}) for all the heteronuclear bialkali molecules. Data from [73–76].

	Na	K	Rb	Cs
Li	-9.83(6)	-16.006(9)	-19(6)	-12.4528(6)
Na		2.227(9)	1.36(1)	7.098(6)
K			-0.26(3)	1.134(4)
Rb				0.87(4)

Table 1.2: Energy changes for the reaction $2XY \rightarrow X_2 + Y_2$, in THz. Negative values indicate the reaction is energetically favourable. Data taken from [73].

Creating heteronuclear molecules presents a greater technical challenge than homonuclear molecules, as the two constituent species must be cooled simultaneously. First, it is obviously necessary to build and maintain two sets of cooling lasers. Second, the cooled atomic clouds must overlap in the same trapping potential. The three inter- and intra-species scattering lengths cannot be optimised independently for both species using Feshbach resonances, which can limit the efficiency of evaporative cooling [77].

When selecting species of heteronuclear molecules, we must consider the chemical stability of the molecules. For some diatomic molecular species XY, the exchange reaction

$$XY + XY \rightarrow X_2 + Y_2 \tag{1.1}$$

may be energetically favourable *i.e.* exothermic. Zuchowski *et al.* [73] compile the energy changes for the exchange reactions from experimentally measured dissociation energies of the lowest vibrational state, and these results are reproduced in table 1.2. We see that KRb and all the dimers which include a Li atom are chemically reactive, while the others are stable.

Zuchowski *et al.* [73] also consider trimer formation reactions of the form

$$XY + XY \rightarrow X_2Y + Y. \tag{1.2}$$

They calculate the binding energies of the possible trimer combinations of alkali atoms, and conclude that all such reactions are substantially endothermic.

The magnetoassociation/STIRAP method was first achieved for a heteronuclear species in 2008 by Ni *et al.*, with the KRb molecule [78]. Since then, Takekoshi *et al.* created and trapped ^{87}RbCs molecules in the absolute ground state in 2014 [79],

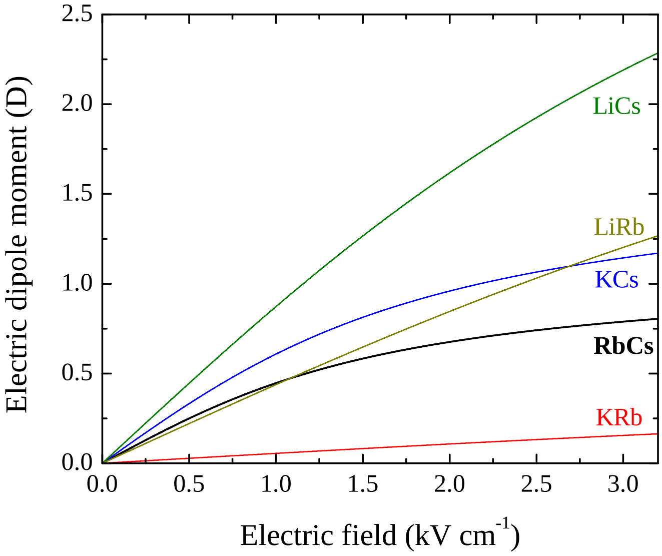

Figure 1.1: Electric dipole moment induced in the laboratory frame by an applied electric field, for a selection of bialkali species.

as did we [80]. ^{23}Na^{40}K was created in 2015 [81] and ^{23}Na^{87}Rb in 2016 [82]. There is also progress toward samples of NaLi [69], KCs [83], YbCs [84], YbRb [85] and YbLi [86, 87].

1.3 RbCs molecules

The RbCs molecule has several advantages over other bialkali species. It has a large permanent dipole moment of 1.26 D (see table 1.1). This can be induced in relatively modest electric fields – the critical field where the laboratory-frame dipole moment is $d_0/3$ is only 0.8 kVcm^{-1}, which is easily attainable in experiments.

The ground state is also chemically stable, as seen in table 1.2. However, the energy of the exchange reaction is only +0.87(4) THz, compared to the vibrational spacing of 1.5 THz [88]. This could let us compare reactive and unreactive species, simply by addressing the $v'' = 1$ vibrational level.

The RbCs molecule has one further advantage: the wavelengths of the STIRAP lasers are unusually convenient. The pump transition we use is 1557 nm, which is within the telecoms C-band, while the Stokes transition is at 977 nm, close to the pump wavelength for an erbium-doped (telecoms) fibre amplifier. These wavelengths are easily accessible by diode lasers at relatively high powers, and optical fibres are readily available and relatively cheap. Acousto- and electro-optic modulators have also been heavily researched and optimised at 1550 nm for the telecoms industry, and are cheap and reliable.

1.4 Thesis summary

At the beginning of the work for this thesis, we had cooled Rb and Cs to degeneracy simultaneously [77]. We had studied in detail the Feshbach structure of ^{85}Rb [89] and mixtures of ^{85}Rb-Cs [90] and ^{87}Rb-Cs [67]. We had also created and trapped ^{87}RbCs Feshbach molecules, and this was presented in a PhD thesis by M. P. Köppinger [93]. In this thesis, we focus on the optical manipulation of these weakly-bound molecules.

We present and characterise the laser system we use to make this transfer. Chapter 3 contains a detailed description of the optical cavity setup used to stabilize and tune the frequencies of the two lasers required for STIRAP.

In chapter 4 we demonstrate the capabilities of the laser system by performing molecular spectroscopy over a wide frequency range, and identifying a suitable route for the STIRAP transfer. The installation of high-voltage electrodes lets us perform Stark spectroscopy on the excited and ground states, leading to a precise measurement of the ground-state permanent electric dipole moment in section 4.4.

We demonstrate STIRAP transfer of ^{87}RbCs molecules from a bound state near dissociation to the rovibrational ground state. We produce a sample of over 2000 ground-state molecules and characterise the transfer route, showing it to be a reliable method for association of polar molecules. We build a model of the transfer including the effects of laser noise, based on [94], and find excellent agreement with experimental measurements of the STIRAP transfer and independent measurements of the laser linewidth and shot-to-shot noise. The ground-state molecular sample has a lifetime of 0.89(6) s. These results are presented in chapter 5.

In chapter 6 we use a novel type of frequency comb, based on difference-frequency generation, to measure the binding energy of the ground-state molecules with a fractional uncertainty of 4×10^{-10}. Finally, we document our progress in constructing a 1D lattice potential to confine the molecules in chapter 7.

In the remainder of this chapter we briefly describe the experimental apparatus and the recent improvements we have made. This is presented here because our method to create Feshbach molecules was mostly characterised before the work for this thesis began, and was presented in earlier theses [91–93].

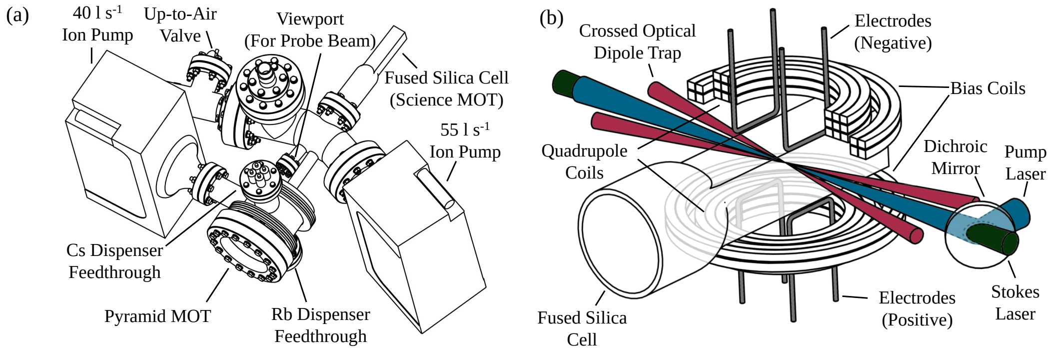

Figure 1.2: Experimental apparatus for the creation of ^{87}RbCs molecules. (a): The vacuum system consisting of two MOTs. A pyramid MOT acts as a cold dual-species atom source for the second labelled as the science MOT. (b) The science MOT, with the locations of magnetic field coils, STIRAP lasers and electrodes shown.

1.5 Experimental setup

Our experimental setup has been extensively documented in other publications [77, 91, 92, 95, 96], and allows us to evaporatively cool ^{87}Rb and Cs to degeneracy in a combined levitated optical potential. Full details of our method for creating Feshbach molecules have also been published [67] and documented in a previous PhD thesis [93]. Here we present a brief overview of this method.

1.5.1 Cooling atoms

The experimental apparatus consists of two magneto-optical traps (MOTs). The first, a pyramid MOT, acts as a dual-species cold atom source for the second, referred to as the science MOT [97]. The vacuum system layout and science MOT apparatus are shown in figure 1.2(a). Following trapping in the science MOT, the ^{87}Rb and ^{133}Cs atoms are optically pumped to the $|F = 1, m_F = -1\rangle$ and $|3, -3\rangle$ low-field-seeking states respectively and subsequently transferred into a magnetic quadrupole trap. The ^{87}Rb atoms are further cooled by forced RF evaporation [95], while interspecies elastic collisions cool the ^{133}Cs atoms sympathetically, until Majorana losses [98] limit further evaporation. We then load the atoms into a magnetically levitated two-beam optical dipole trap ($\lambda = 1550$ nm) [96],

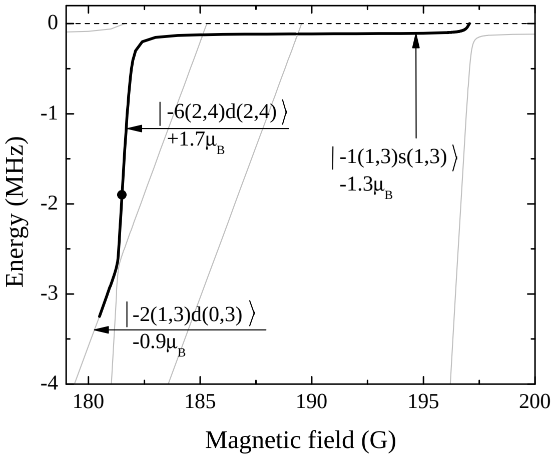

Figure 1.3: Near-dissociation molecular Feshbach states in the magnetic field range we use, relative to the combined ^{87}Rb $|F = 1, m_F = 1\rangle$ and Cs $|3, 3\rangle$ energies. The solid line shows the Feshbach states we can occupy, and the dot shows the state and magnetic field we use for STIRAP. The magnetic moments of each state are labelled.

using RF adiabatic rapid passage to transfer the ^{87}Rb and ^{133}Cs atoms into the $|1, 1\rangle$ and $|3, 3\rangle$ high-field-seeking states respectively. The combination of bias field and quadrupole field is chosen to levitate both of these states against gravity. By reducing the optical trap powers, we routinely evaporate to a nearly-degenerate sample of $\sim 2.5 \times 10^5$ ^{87}Rb atoms and $\sim 2.0 \times 10^5$ ^{133}Cs atoms at a temperature of ~ 300 nK [77], from which we can begin magnetoassociation.

1.5.2 Creating Feshbach molecules

The near-threshold bound states relevant for the magnetoassociation of ^{87}RbCs molecules are shown in figure 1.3. These states are labelled as $|n(f_{\mathrm{Rb}}, f_{\mathrm{Cs}})L(m_{f_{\mathrm{Rb}}}, m_{f_{\mathrm{Cs}}})\rangle$, where n is the vibrational label for the particular hyperfine $(f_{\mathrm{Rb}}, f_{\mathrm{Cs}})$ manifold, counting down from the least-bound state which has $n = -1$, and L is the quantum number for rotation of the two atoms about their centre of mass, following the convention laid out in [66]. Note that all states have $M_{\mathrm{tot}} = 4$, where $M_{\mathrm{tot}} = M_F + M_L$ and $M_F = m_{f_{\mathrm{Rb}}} + m_{f_{\mathrm{Cs}}}$. Magnetoassociation is performed in the magnetically levitated crossed dipole trap by sweeping the bias field down across a Feshbach resonance at 197.10(3) G with a speed of 250 G s^{-1} to produce molecules in the $|{-1}(1,3)s(1,3)\rangle$ state. The bias field is then reduced rapidly, to transfer the molecules into the $|{-2}(1,3)d(0,3)\rangle$ state at 180.487(4) G via the path shown in figure 2.2(b). The magnetic quadrupole field required to levitate the molecules in this state causes the remaining atoms to be over-levitated. This allows us to purify the molecular cloud by using the Stern-Gerlach effect to remove the atoms. The number of molecules we produce is optimized by varying the ratio of ^{87}Rb and ^{133}Cs before association by changing the number of Cs atoms loaded into the science MOT. We find that the molecule production is maximized when the mean phase-space density of the mixture is maximized (see figure 5 in [67]). To detect the molecules, we quickly ramp back across the same resonance to dissociate into atoms. Both species of atoms are detected by absorption imaging, with the probe light propagating along the axis of the vacuum cell. We typically create trapped samples of $\sim$ 2500 molecules with the same temperature as the original atomic sample, and a lifetime in the $|{-2}(1,3)d(0,3)\rangle$ state of 200 ms. We attribute the low conversion efficiency to the large interspecies scattering length of $\sim 650\ a_0$ [66, 77], which limits the phase-space densities of the atomic samples.

Trapping the $|{-2}(1,3)d(0,3)\rangle$ state is convenient in our apparatus, as the quadrupole field which we generate can only magnetically levitate states with a negative magnetic dipole moment (high-field-seeking). However, trapping the neighbouring low-field-seeking $|{-6}(2,4)d(2,4)\rangle$ state is still possible by transferring the molecules into a pure optical trap which is sufficiently deep to support the molecules against gravity. This is achieved through a three stage process. First, the dipole trap power is increased from 200 mW to 1 W, increasing the trap depth to 12.7 μK. The magnetic levitation gradient is then removed, followed by a bias field ramp up to $\sim$ 181.6 G at a speed of 2.3 G ms^{-1}. The critical ramp speed ($\dot{r_c}$), below which the avoided crossing between two states (shown in figure 1.3) is adiabatically followed, is given by

$$\dot{r_c} = \frac{2\pi V^2}{\hbar \Delta\mu}, \tag{1.3}$$

where V is the coupling strength, and $\Delta\mu$ is the difference in the magnetic moment between the two states. The critical ramp speed for this avoided crossing is $\sim$ 70 G ms^{-1}, significantly greater than the ramp speed we use. Hence, we observe

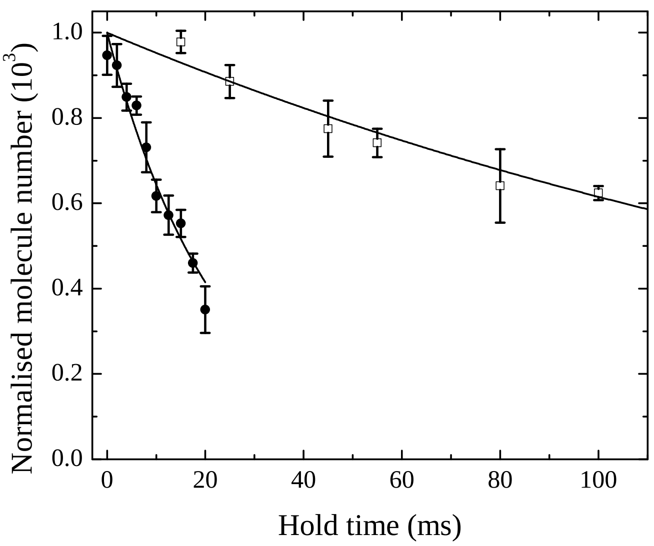

Figure 1.4: Lifetime of the $|{-6}(2,4)d(2,4)\rangle$ Feshbach state in a pure optical trap (closed circles), compared to the $|{-2}(1,3)d(0,3)\rangle$ in a levitated trap (open squares). Fitted exponentials give 23(2) ms and 0.21 s respectively. The latter is the same data as in [93].

the molecules being transferred efficiently between the two states. The transfer to a tighter dipole trap heats the molecules to a temperature of 1.5 μK, due largely to the adiabatic compression of the gas. However, by turning off the magnetic gradient which levitated the $|{-2}(1,3)d(0,3)\rangle$ state we remove the variable Zeeman shift across the cloud which results from the use of a magnetic field gradient.

This transfer reduces the lifetime of the molecules, from 0.21(1) s when they are in the $|{-2}(1,3)d(0,3)\rangle$ state to 23(2) ms in the $|{-6}(2,4)d(2,4)\rangle$ state, as shown in figure 1.4. We believe that this is due to fast collisional losses in the $|{-6}(2,4)d(2,4)\rangle$ state, because the lifetime increases to 0.89(6) s when we transfer to the ground state in chapter 5, but we have not investigated this in detail. The shorter lifetime is still easily adequate for all the experiments presented in this thesis.

1.5.3 Improvements to imaging

We analyse our atoms with standard absorbtion imaging. In this, we shine a beam of resonant light at the atoms and photograph the shadow with a CCD camera. A pair of lenses between the atoms and the CCD form a microscope with a magnification of 1.84, giving a resolution of 8.4 µm/px. We image the Cs and Rb atoms sequentially with the same camera. The imaging scheme is described in detail in [97].

To photograph the atoms, we release them from the optical trap and simultaneously turn off the magnetic field. A pair of shim coils makes a small quantisation field along the axis of the imaging beam. We image with a 50 µs pulse of light tuned to the $F = 4 \rightarrow F = 5$ ($F = 2 \rightarrow F = 3$) cooling transition in Cs (Rb). We turn on the MOT repump beams throughout the imaging pulse to keep the atoms in the closed cooling transition. When working with molecules, we dissociate them into atoms and take an image with each species. The Cs image is taken first, and the Rb image 4.92 ms later. The gap between the images is limited by the acquisition rate of the CCD. We can therefore image the Cs atoms immediately after releasing them from the trap, but the image of the Rb atoms is delayed by a minimum of 5 ms time-of-flight. This free expansion reduces the optical density of the cloud of Rb atoms such that we cannot detect fewer than ~ 2000 molecules. By contrast, we can detect ~ 200 molecules in the Cs image.

Many of the experiments in this thesis rely on measuring changes in the molecule number, for example to locate one- or two-photon resonances as in figure 4.6. In some cases we need to detect only a few hundred molecules, such as in the initial ground-state transfer in figure 5.1, or the ground-state lifetime in figure 5.12. The imaging system has a 4×4 mm^2 field of view, which allows time-of-flight expansion images of atomic samples for up to 25 ms before gravity pulls the sample out of the camera frame. Our molecular sample is only around 10×40 µm^2 and covers only a few pixels, so it is not ideal for measuring small atom numbers. We have therefore optimised our imaging method to detect the lowest possible atom numbers without changing any of the imaging hardware.

The first change is simple: the optical trap is turned back on after the first (Cs) image is taken, so the atoms are recaptured and held until the second (Rb) image is taken. This lets us image both the Cs and the Rb atoms with effectively zero time-of-flight. Thus we can detect a few hundred molecules with both the Cs

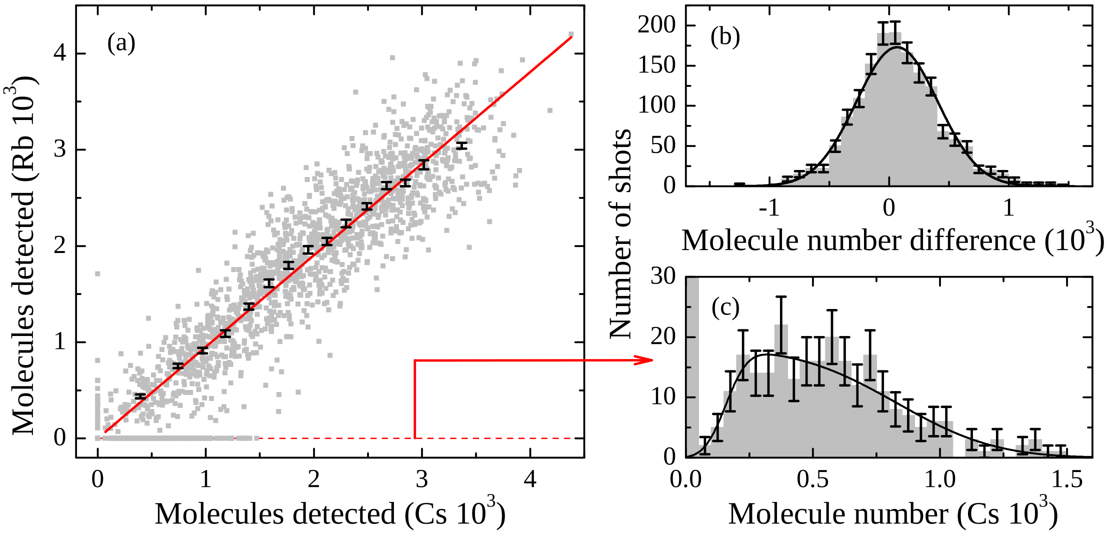

Figure 1.5: Comparison of the molecule number N measured with the Cs and Rb absorbtion images. (a) Points from individual experimental shots are in grey. The non-zero points are binned by Cs number and shown in black, with standard error bars shown. The solid line shows a linear fit through zero with a gradient of 0.952(4), *i.e.* the Rb image always gives a molecule number $\sim 4.8(4)\%$ lower than the Rb image. (b) Histogram of the molecule number difference between the two species, with a fitted Gaussian half-width of $0.68(1) \times 10^3$ and $\chi^2/\nu = 1.9$. (c) Histogram of the shots where $N_{\mathrm{Rb}} = 0$. A fit with a double error function (equation 1.4) allows us to extract the detection limits of $0.16(2) \times 10^3$ for the Cs images and $0.8(1) \times 10^3$ molecules for Rb images.

and Rb imaging systems, effectively doubling our data rate compared to our early molecular work [67, 93].

Detecting low atom numbers is easiest with a small, dense sample, as a large optical depth increases the visibility of the cloud over the background CCD noise. We thus compress the cloud before imaging it, by turning the optical trap up to ~ 2 W per beam after the molecules are dissociated. The trap frequencies increase suddenly and the cloud is compressed, increasing the optical depth of the sample. However, as the atoms rethermalise in the tighter trap, they expand and the optical depth drops off within a few ms, limiting the compression available for both species. With around 2000 molecules we get a peak optical depth around 0.6.

Detecting the molecules with two images gives us a simple way to check that the imaging system is working correctly, and to calculate the detection limits for the Rb and Cs images: we compare the molecule number between the two. Nominally these should be identical in the Cs and Rb images, since the atoms are formed from a pure sample of dissociated molecules. Random noise on each image, from power fluctuations in the probe beam and detection noise, turns this into a 1:1 statistical correlation. However, in figure 1.5(a) we see the numbers are not perfectly correlated, and the Rb images give a number averaging 5% less than Cs. This is probably caused by differences in the intensities of the imaging beams. We are usually more concerned with relative changes in molecule number, and the 5% difference is considerably smaller than our shot-to-shot variation, so this discrepancy is not a great concern.

In figure 1.5(b), we also look at the difference between the (nominally identical) numbers in each species. We can estimate the statistical noise on the molecule number as the $\sigma = 0.68(1) \times 10^3$ normally-distributed variation between the species.

In figure 1.5(c) we also see that the Rb imaging is less sensitive to low molecule numbers. There are many points where no molecules were detected, and we see $N_{\mathrm{Rb}} = 0$ shots appear when the Cs images show $N_{\mathrm{Cs}} \sim 800$, and disappear around $N_{\mathrm{Cs}} \sim 200$, which we can interpret as the detection limits for Rb and Cs respectively. This is quantified by fitting a double error function of the form

$$y = \frac{y_0}{2} \left[\mathrm{erf}\left(\frac{N - N_1}{w_1} \right) - \mathrm{erf}\left(\frac{N - N_2}{w_2} \right) \right], \tag{1.4}$$

where $N_1 = 0.16(2) \times 10^3$ and $N_2 = 0.8(1) \times 10^3$ are the Cs and Rb detection limits respectively.

We note that these conclusions only apply to molecules trapped in the 1550 nm optical trap, which includes all the work presented in chapters 4, 5 and 6 but not chapter 7 where we use a different 1064 nm optical potential. In principle the same analysis could be applied to this potential, if we took large amounts of data at a single trapping power.

1.5.4 Control system improvements

During the work for this thesis, we upgraded the control system for our experiment to improve the flexibility and automate a variety of measurements. I present here a short summary of these upgrades.

The core of the original control program was a National Instruments (NI) PCI-7833R FPGA board. This gave 48 digital lines, 8 analog outputs and 8 digital inputs. The digital lines controlled many things, including optical shutters, magnetic coils and AOMs. Through an analog voltage switching system, they also controlled AOM frequencies and intensities, and some coil currents. The analog outputs controlled some coil currents, and the analog ramps for the RF and optical trap evaporation. An arbitrary waveform generator for the RF evaporation and spin flip frequencies was controlled over GPIB, by a different computer which communicated with the FPGA via a PCI-DIO-32HS digital input/output card. This system had two main problems:

- Only 8 analog channels were available. More were needed, particularly for the second optical trap (see chapter 7).
- The experimental sequence was built into the structure of the program, making large changes to the sequence difficult.

A bug in this original control system also introduced a 25 s dead-time in our experimental cycle. This bug was fixed before the work began for this thesis, and in doing so, we reduced the duty cycle to $\sim$ 70 s per shot, increasing our data rate by 25% compared to previous work [91–93].

We therefore put in a new system based on the “DExTer” control program, which was designed and built by Tim Wiles [99], and which is currently used in six separate experiments in Durham. This is based on the same PCI-7833R FPGA board. It gives the same input and output lines as the original system, and an extra 24 digital and 16 analog “slow” outputs, with update speeds of 8.2 µs and 40 µs respectively, compared to 0.9 µs and 1.7 µs for the “fast” lines. In this program, an experimental sequence is represented as a series of timesteps of varying length, where each digital channel can be on or off, and each analog voltage can be set.

Both systems allow automated measurements, by repeating a sequence many times and varying a timestep length or voltage to an analog output. However, the new system can vary any timestep or analog voltage, while the old system was limited to a predefined list of options, changeable only by altering the program code. This means more experiments and measurements can be done automatically, decreasing the delay between experimental runs and thus producing more data.

We have fixed several bugs in the program, mainly to improve the interface, but one deserves a special note for anyone building other FPGA systems. The digital lines of an FPGA such as the 7833R can be configured as inputs or outputs, and generally this is defined in the code. As an output, each line has a low impedance. As an input, the line has a high impedance, and this is the default state when the FPGA turns on. However, if a line which should be an output is configured as an input, the high impedance lets the voltage float and, under some circumstance, the voltage can reach the TTL "high" level. This is problematic when controlling devices which can only be switched on under certain conditions or for a limited time, such as high-current magnetic coils which could overheat. Allowing the line to float high risks damaging these devices. Usually this does not occur because the line is configured correctly and the output set to 0 or 1 when an experimental sequence runs. However, a line can be reset to the default (high-impedance) state and allowed to float, if a new program is loaded to the FPGA but does not write to the line immediately, or if the FPGA is reset. We add several safety features to the FPGA system to avoid this:

- The FPGA does not reset between sequences or when the program starts.
- When the FPGA program starts and ends, we write default values to all outputs to configure them correctly.
- The experimental sequence and manual control functions run on a single FPGA which is not reloaded when switching between these.

The DExTer program can also control devices via GPIB from the same computer. During any given timestep, the FPGA can signal the host program to run one of several numbered Labview routines, which the user can program as they wish. Typically these are used for complex tasks such as setting a power supply voltage or configuring a signal generator to perform the RF evaporation ramps. However, these routines are also not limited to GPIB communication - in principle the program can run any LabVIEW code.

We have built into this a “remote control” system to send signals to other programs over a network. This is useful where the control of a device is too complex to be implemented directly within the FPGA host program, such as creating the pulse sequence for STIRAP in chapter 5. Each target program is given a unique Target Name. The FPGA host program writes a file to a shared drive, giving a list of Target Names and numeric parameters, which it can vary automatically in a similar way to varying a timestep length or analog voltage. The target program searches this file for its Target Name, reads the appropriate parameter and updates accordingly. Thus with minimal extra programming, we can automatically scan almost any computer-controlled parameter from the main control program. An early version of this system controlled the laser detunings in the frequency comb measurements (chapter 6), and the system can now control the shape and timing of the STIRAP pulse sequence (section 3.4).

Chapter 2

Basic theory

This chapter covers the basic theory of molecular interactions which underpins the study of ultracold molecules. It outlines the theory of dipole-dipole interactions and some of the models which can be tested with ultracold molecules. It also includes the theory needed to understand the creation and trapping of ground-state molecules: molecular structure, Feshbach resonances, the mathematical basis of stimulated Raman adiabatic passage, and the theory of optical trapping potentials for atoms and molecules.

2.1 Dipole interactions

One of the main attractions of ultracold heteronuclear molecules is their permanent dipole moment, and the associated long-range, anisotropic dipole-dipole interactions which contrast with the short-range contact interactions of non-polar atoms and molecules [100]. For two particles separated by $\vec{r}$ with dipole moments along the unit vectors $\hat{e_1}$ and $\hat{e_2}$, the energy of the dipole-dipole interaction is

$$U_{\text{dd}}(\vec{r}) = \frac{C_{\text{dd}}}{4\pi} \frac{(\hat{e}_1 \cdot \hat{e}_2) r^2 - 3(\hat{e}_1 \cdot \vec{r})(\hat{e}_2 \cdot \vec{r})}{r^5}. \tag{2.1}$$

If we assume that the sample is polarised, so that all the dipoles point in the same direction along the z-axis, *i.e.* $\hat{e}_1 = \hat{e}_2$, this simplifies to

$$U_{\text{dd}}(r) = \frac{C_{\text{dd}}}{4\pi} \frac{1 - 3\cos^2\theta}{r^3} \tag{2.2}$$

where θ is the angle between the direction of polarisation (the z-axis) and the relative position of the particles. From equation 2.2, we see the long-range ($1/r^3$) character of the dipole-dipole interaction. We also see the anisotropic term ($1 - 3\cos^2\theta$), which makes the interaction repulsive if the dipoles are positioned side-by-side ($\theta = 90°$) or attractive if they are positioned end-to-end ($\theta = 0°$). The interactions vanish for the angle $\theta = \arccos(1/\sqrt{3}) \simeq 54.7°$

C_{dd} is the coupling constant for the interaction. For particles with a permanent magnetic dipole moment μ this is $C_{\mathrm{dd}} = \mu_0\mu^2$; for a permanent electric dipole moment d this is $C_{\mathrm{dd}} = d^2/\epsilon_0$. For molecules, d is typically $\approx q_{\mathrm{e}}a_0$ with q_{e} the electron charge and a_0 the Bohr radius, while the magnetic moment is typically on the order of the Bohr magneton μ_{B}. Expressing a_0 and μ_{B} in terms of fundamental constants, we find that the ratio of the magnetic and dipolar coupling constants is

$$\frac{\mu_0\mu^2}{d^2/\epsilon_0} \sim \alpha^2 \sim 10^{-4} \tag{2.3}$$

where $\alpha \approx 1/137$ is the fine-structure constant. To realise significant dipole-dipole interactions in a quantum gas, one can use particles with either a magnetic or an electric dipole moment, but from equation 2.3 we see the coupling is usually much stronger in the electric case.

Because of their large electric dipole moments, polar molecules are excellent candidates for studying dipolar effects. To have a significant electric dipole moment, the molecule must fulfil three requirements [100]:

1. A heteronuclear molecule is needed to break the symmetry of the molecule and allow a dipole moment.

2. The molecule must be in a low rovibrational state, because the dipole moment scales as R^{-7} with internuclear separation R [71], and because higher rovibrational states are often not stable against collisional relaxation.

3. An external electric field, typically around 10 kV/cm, must be applied to orient the molecule, so that the laboratory frame dipole moment asymptotically approaches the dipole moment along the internuclear axis. Alternatively, the molecules must be prepared in a superposition of opposite-parity rotational states [26].

By creating ^{87}RbCs molecules in their absolute ground state, we can fulfil conditions 1 and 2, while condition 3 can be fulfilled simply with high-voltage electrodes inside or outside the vacuum chamber, though there are technical difficulties with this (see section 4.4.1), or by driving microwave transitions between rotational levels to prepare the superposition.

We will now look at two specific effects of polar molecule interactions which we may be able to observe in our experiment: long-lived collision complex formation and spin-lattice models.

2.1.1 Spin-lattice models

One of the most exciting systems that can be tested with ultracold molecules is the spin-lattice model [101]. This class of models is ubiquitous in condensed-matter physics, and is used as a simplified model to describe the characteristic behaviour of more complex interacting systems [102]. This has been demonstrated in KRb [26, 27], but the larger permanent electric dipole moment of the ^{87}RbCs molecule mean that the effects should be more pronounced. Polar molecules confined in a 3D optical lattice can realise the long-ranged spin-1/2 model given by the Hamiltonian

$$H = \sum_{i \neq j} \frac{V_{ij}}{2} \left[\frac{J_\perp}{2} (S_i^+ S_j^- + h.c.) + J_z S_i^z S_j^z \right] \tag{2.4}$$

by encoding the spin in two rotational states of the molecule [27, 101]. Here the summation runs over all occupied lattice sites with positions $\vec{r}_i$ in units of the lattice spacing a, and the terms $S_i^\pm$ and S_i^z are spin-1/2 operators. $V_{ij} = (1 - 3\cos^2\theta_{ij})/|\vec{r}_i - \vec{r}_j|^3$ is the dipolar coupling between sites i and j. The exchange terms $S_i^+ S_j^- + h.c.$ swap the spin states of molecules i and j. The strength of the spin-exchange interaction is characterised by $J_\perp = -d_{\downarrow\uparrow}^2/4\pi\epsilon_0 a^3$ where $d_{\downarrow\uparrow} = \langle\downarrow| d |\uparrow\rangle$ is the dipole matrix element between the spin states $|\downarrow\rangle$ and $|\uparrow\rangle$. The "direct" or "Ising" term $J_z S_i^z S_j^z$ arises because in general the $|\uparrow\rangle$ and $|\downarrow\rangle$ have different dipole moments. However, if there is no external electric field, $J_z = 0$ and this term can be neglected.

The dynamics of this system can be probed with a Ramsey interferometry sequence. The two "spin" states, which are actually rotational states, are coupled with a microwave field. A $\pi/2$-pulse creates an equal superposition, and a second $\pi/2$-pulse a time t later is phase shifted by ϕ. The contrast of the resulting Ramsey fringes can be predicted numerically and has a strong dependence on the filling fraction of the lattice [26].

The strength of the dipole interaction can be tuned, by realising the spin-1/2 system with different pairs of rotational states which have different transition matrix elements $\langle\downarrow| d |\uparrow\rangle$. This model also demonstrates the long-range, anisotropic nature of the dipole-dipole interaction, as the coupling between lattice sites depends strongly upon the both lattice geometry and the orientation of the dipoles relative to the lattice axes [27].

2.1.2 Collision complex formation

Understanding the dynamics of ultracold molecules can provide unique information about the role of tunneling, zero-point energy and quantum reflection effects in determining chemical reactivity, and the effect of long-range interactions on chemical reactions. However, understanding and modelling ultracold molecular collisions is a difficult problem. This is principally because the dynamics are governed by complex three- or four-body anisotropic potentials, so that many angular momentum states may contribute to scattering, while experiments are limited to a few observables, such as a loss rate and sometimes a temperature and elastic cross section.

For alkali-metal atoms, scattering models can be thoroughly tested by the observation of Feshbach resonances [21]. For atom-molecule collisions, the rovibrational density of states for three-atom complexes [103] is large enough that calculating and assigning atom-molecule resonances from a potential energy surface is probably impossible [6]. For molecule-molecule collisions, the density of states for four-atom complexes is predicted to be so high that the molecule-molecule resonances cannot even be experimentally resolved [6].

Mayle *et al.* suggest that a statistical treatment of the molecule-molecule resonances can bypass the inherent complexity of the problem, and the observables can be described by simpler, non-resonant scattering calculations [6]. For the case of nonreactive RbCs, the large number of very narrow resonances implies the existence of many weakly-bound complexes with very long lifetimes, sometimes on the order of experimental times. This means that some molecules can be hidden as two-molecule (four-atom) complexes, while a third molecule can collide with this complex and remove it from the trap. This leads to a delayed three-body loss mechanism, where the density of molecules n_{m} and complexes $n_{\mathrm{c},L}$ can be modelled by coupled rate equations

$$\dot{n}_{\mathrm{m}} = \sum_{L} \left(-n_{\mathrm{m}}^2 \sum_{M_L} K_{\mathrm{mm}}^{L,M_L} + 2\gamma_L n_{\mathrm{c},L} - K_{\mathrm{mc}} n_{\mathrm{m}} n_{\mathrm{c},L} \right) \tag{2.5}$$

$$\dot{n}_{\mathrm{c},L} = \frac{1}{2} n_{\mathrm{m}}^2 \sum_{M_L} K_{\mathrm{mm}}^{L,M_L} - \gamma_L n_{\mathrm{c},L} - K_{\mathrm{mc}} n_{\mathrm{m}} n_{\mathrm{c},L}. \tag{2.6}$$

Here K_{mm}^{L,M_L} and K_{mc} are the molecule-molecule and molecule-complex collision rate constants, γ_L is the decay rate of the complexes and L is the partial wave of the collision. These rates have all been estimated using multichannel quantum defect theory [6], and are expected to change dramatically when an electric field is applied to induce a molecular electric dipole moment in the laboratory frame. By contrast, the reactive KRb molecule cannot be described by these equations.

2.2 Stimulated Raman adiabatic passage

Stimulated Raman Adiabatic Passage, or STIRAP, is a general method to transfer population between states of a system which are not directly linked. It uses an intermediate state which has strong coupling to both the initial and final states, but which can exhibit fast loss if populated. STIRAP can achieve transfer efficiencies asymptotically approaching 100%. It is also relatively insensitive to variations in experimental parameters compared to, for example, driving π-pulses between states, which relies on careful control of the timing and Rabi frequency [104].

STIRAP was first suggested as a simple theoretical proposal in December 1989[1] [105]. However, a solid theoretical basis and the first experimental observation were given in 1990 [106]. It was initially used in molecular beam experiments,

---

[1] Curiously, this makes it exactly the same age as me!

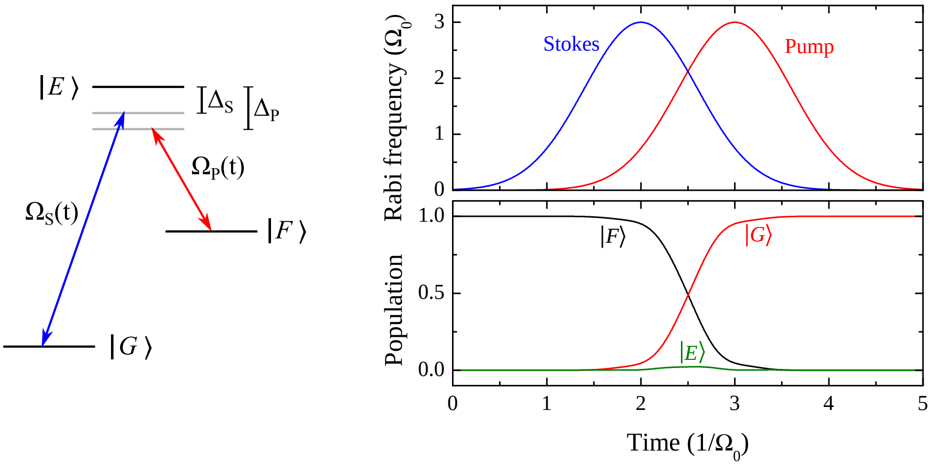

Figure 2.1: Left: level system for STIRAP. The system starts in state $|F\rangle$ and is transferred to $|G\rangle$. Rabi frequencies and detunings for both lasers are shown. Right: simulation of idealised STIRAP transfer. The lasers are on resonance ($\Delta_P = \Delta_S = 0$). Top: Pump and Stokes Rabi frequencies, showing the "counterintuitive" pulse sequence. Bottom: populations in the initial, intermediate and final states $|F\rangle$, $|E\rangle$ and $|G\rangle$ through the transfer sequence. The intermediate state is almost unpopulated throughout. This is a simplified version of the model used to simulate our molecular transfer in section 5.5.

to transfer molecules to vibrational excited states and study collisional dynamics. 25 years later, it has been used in many systems, including qubit manipulation and detection [107, 108], creating coherent superpositions of photon Fock states [109] and electron spin states of ThO [110], photon transfer between waveguides [111, 112] and transfer between hyperfine states in doped crystals [113, 114], as well as manipulation of the internal states of molecules. A thorough review of STIRAP and its uses was recently written by Bergmann *et al.* [104].

2.2.1 STIRAP - mathematical basis

We will now look at the mathematical and quantum mechanical basis of STIRAP, and try to get an intuitive picture of the process. STIRAP is based on an analytic solution to the Hamiltonian of a three-level λ system. For a level structure as shown in figure 2.1 the Hamiltonian is, in the rotating-wave approximation,

$$\hat{H} = \frac{\hbar}{2}\begin{pmatrix} 0 & \Omega_{\mathrm{P}}(t) & 0 \\ \Omega_{\mathrm{P}}(t) & 2\Delta_{\mathrm{P}} & \Omega_{\mathrm{S}}(t) \\ 0 & \Omega_{\mathrm{S}}(t) & 2(\Delta_{\mathrm{P}} - \Delta_{\mathrm{S}}) \end{pmatrix}, \tag{2.7}$$

We refer to the coupling lasers as the “pump” and “Stokes” with Rabi frequencies Ω_{P} and Ω_{S} respectively, with detunings Δ_{P} and Δ_{S}. If we set the lasers on two-photon resonance, *i.e.* $\Delta_{\mathrm{P}} = \Delta_{\mathrm{S}} = 0$, the eigenstates of $\hat{H}$ can be found analytically:

$$|a^+\rangle = \sin\theta\sin\phi\,|F\rangle + \cos\phi\,|E\rangle + \cos\theta\sin\phi\,|G\rangle \tag{2.8}$$

$$|a^0\rangle = \cos\theta\,|F\rangle - \sin\theta\,|G\rangle \tag{2.9}$$

$$|a^-\rangle = \sin\theta\cos\phi\,|F\rangle - \sin\phi\,|E\rangle + \cos\theta\cos\phi\,|G\rangle\,. \tag{2.10}$$

The mixing angle θ is given by

$$\tan\theta = \frac{\Omega_{\mathrm{P}}}{\Omega_{\mathrm{S}}}. \tag{2.11}$$

The second mixing angle ϕ is given by

$$\tan 2\phi = \frac{\sqrt{\Omega_{\mathrm{P}}^2 + \Omega_{\mathrm{S}}^2}}{\Delta_{\mathrm{P}}}. \tag{2.12}$$

but is not relevant to this discussion.

STIRAP uses the dark state $|a^0\rangle$, which crucially has no component of state $|E\rangle$. We note that, when $\Omega_{\mathrm{P}} = 0$ and $\Omega_{\mathrm{S}} \gg 0$, the dark state is $|a^0\rangle = |F\rangle$. If instead $\Omega_{\mathrm{P}} \gg 0$ and $\Omega_{\mathrm{S}} = 0$, the dark state is $|a^0\rangle = |G\rangle$. For any other values of Ω_{P} and Ω_{S}, $|a^0\rangle$ is a superposition of $|F\rangle$ and $|G\rangle$, which we can use to transfer our system from $|F\rangle$ to $|G\rangle$. A pulse sequence for STIRAP begins with only the Stokes light illuminating the molecules, which initializes the dark state as $|a^0\rangle = |F\rangle$. Ramping the intensity of the Stokes laser down and the pump laser up changes the mixing angle θ, and thus the composition of the dark state. If these ramps are sufficiently slow, the dark state transforms adiabatically from $|F\rangle$ to state $|G\rangle$, and the other states $|a^+\rangle$ and $|a^-\rangle$ are never populated. This means the lossy state $|E\rangle$ is never populated, and all the population is moved from $|F\rangle$ to $|G\rangle$. In practice the ramps cannot be infinitely slow, so the adiabaticity is never perfect and a small part of the population is excited to $|E\rangle$.

In figure 2.1 we see a sketch of the STIRAP process. The Stokes coupling turns on first, and then ramps down as the pump coupling ramps up, causing the slow transfer between the states $|F\rangle$ and $|G\rangle$, with only a small population reaching state $|E\rangle$. This is the typical picture of the "counterintuitive" pulse sequence, where the ramp sequence is a pair of Gaussian pulses, with the Stokes starting before the pump. This picture is commonly used in experiments with molecular beams, where the temporally offset pulses can be made by physically offsetting the two laser beams along the flight path of the molecules [106]. However, it tends to disguise the physical intuition behind the process. The STIRAP process should not be viewed as a Stokes pulse, followed by a pump pulse. The proper intuition is a slow adiabatic change of the state, as the Stokes coupling decreases and the pump coupling simultaneously increases.

The efficiency of STIRAP is 100% if the whole population is held in the dark state throughout the transfer. In practice however, the efficiency of the transfer P when on two-photon resonance is reduced due to non-adiabaticity of the dark state evolution, and limitations imposed by laser decoherence, such that [94]

$$P = \exp\left(-\frac{\pi^2\gamma}{\Omega_0^2\tau} - \frac{D\tau}{2}\right). \tag{2.13}$$

Here, γ is the natural linewidth of the state $|E\rangle$, D is the linewidth associated with the frequency difference between the two lasers, τ is the transfer time and Ω_0 is the reduced Rabi frequency, defined as $\Omega_0 = \sqrt{\Omega_\mathrm{P}^2 + \Omega_\mathrm{S}^2}$, where Ω_P and Ω_S are the peak Rabi frequencies of the pump and Stokes transitions respectively. By minimizing the two contributions to the exponential in equation 2.13 we can derive the necessary condition for efficient transfer [94]:

$$\frac{\Omega_0^2}{\pi^2\gamma} \gg \frac{1}{\tau} \gg D. \tag{2.14}$$

From this we see the requirements for STIRAP: high Rabi frequencies for both transitions, an intermediate state with a long natural lifetime, and a pair of narrow-linewidth lasers.

In practice, Ω_0^2/γ is limited by the available laser intensity. This sets the minimum required duration of the transfer to remain adiabatic. This in turn sets the maximum linewidth allowed to maintain coherence of the dark state. Therefore, the

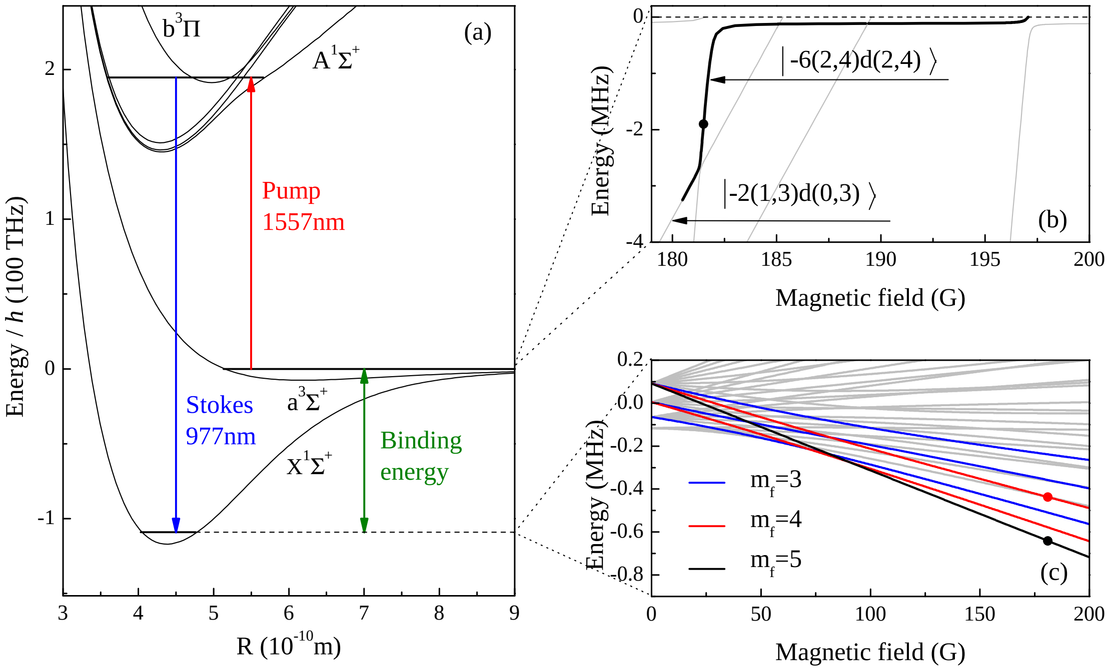

Figure 2.2: Molecular potential and states for STIRAP transfer of ^{87}RbCs to the ground state. Left: Interatomic potentials showing the singlet $X^1\Sigma^+$ and triplet $a^3\Sigma^+$ ground state potentials, and the lowest excited electronic potentials. Arrows show the pump and Stokes laser frequencies. Top right: near-dissociation molecular Feshbach states in the magnetic field range we use, relative to the combined ^{87}Rb $|F = 1, m_F = 1\rangle$ and Cs $|3, 3\rangle$ energies. The solid line shows the Feshbach states we can occupy, and the dot shows the state and magnetic field we use for STIRAP. Bottom right: hyperfine structure of the ^{87}RbCs rovibrational ground state, showing the $m_f = 4$ and $m_f = 5$ states we can address (see figure 6.5).

second criterion is that the linewidth of each of the lasers must be suitably narrow such that the linewidth associated with the frequency difference between the two lasers is minimized. In our experiment we find transitions which allow pulse durations on the order of ~ 10 μs. This indicates that the maximum linewidth for efficient transfer is on the order of 1 kHz.

2.3 RbCs molecular structure

We will briefly discuss the molecular theory and notation relevant to this work. In general, molecular structure and spectroscopy is a vastly complicated topic, and many books have been written about it, *e.g.* [115–118]. Here we will limit ourselves to the basic structure of linear diatomic molecules, such as ^{87}RbCs.

The description of molecular structure is simplified somewhat if we make two approximations. First, when atoms associate to form molecules, the inner electron shells are almost unperturbed. Only the outer valence electrons are distributed throughout the molecule to give the binding force [115]. Second, the masses of the nuclei are much larger than that of the electron, typically $M_N/M_e \sim 10^3 - 10^5$. Thus the motion of the nuclei is slow compared to that of the electrons, and we can approximate that the nuclei are at fixed positions within the molecule. This is known as the *Born-Oppenheimer approximation*, and means we can treat the electron and nuclear motions separately.

2.3.1 Electronic structure

We can estimate the separation of the electronic energy levels in molecules. Let R_0 be a typical average distance between the nuclei in a molecule. The valence electron wavefunction is spread over roughly this distance, so from the uncertainty principle the electron has a momentum of magnitude $\sim \hbar/R_0$. A rough estimate of the electronic energies is then [115]

$$E_e \approx \frac{\hbar^2}{mR_0^2}. \tag{2.15}$$

For a typical internuclear separation of a few Å, we get $E_e \sim 1$ eV ~ 250 THz, similar to the binding energy of the outer electrons in single atoms.

Diatomic molecules have angular momenta from rotation, electron orbits, electron spin and nuclear spin. The good quantum numbers for the angular momentum depend on the relative strengths of the couplings between these. There are five coupling cases, known as Hund's cases (a) to (e). Hund's cases are idealised situations which help to understand the pattern of rotational levels, but in general

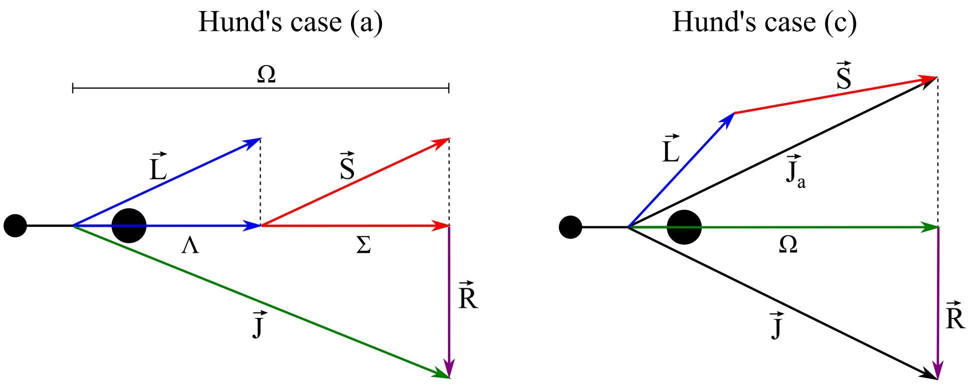

Figure 2.3: Coupling of orbital and electron spin angular momenta in Hund's cases (a) and (c), the cases relevant to the ^{87}RbCs molecule.

no molecule will fit perfectly with a particular case. Here we will look at cases (a) and (c) which are relevant to the RbCs molecule. Following [118], we denote the angular momenta as follows:

$\vec{L}$	the electronic orbital angular momentum.
$\vec{S}$	the electronic spin angular momentum.
$\vec{J}$	the total angular momentum.
$\vec{N}$	the total angular momentum excluding electron spin, $\vec{N} = \vec{J} - \vec{S}$.
$\vec{R}$	the rotational angular momentum of the nuclei, $\vec{R} = \vec{N} - \vec{L}$.

In Hund's case (a), shown as a vector diagram in figure 2.3, the orbital angular momentum $\vec{L}$ couples strongly to the internuclear axis by electrostatic forces. The electron spin angular momentum $\vec{S}$ in turn strongly couples to the orbital angular momentum $\vec{L}$ by spin-orbit coupling. The components of $\vec{L}$ and $\vec{S}$ along the internuclear axis are well-defined with quantum numbers Λ and Σ. Their sum is denoted by $\Omega = \Lambda + \Sigma$. The rotational angular momentum $\vec{R}$ is coupled to a vector $\vec{\Omega}$ along the internuclear axis to form the total angular momentum $\vec{J}$ with quantum number J_0. The good quantum numbers for angular momentum are Λ, S, Σ, J_0 and Ω.

In Hund's case (c), also shown in figure 2.3, the coupling between $\vec{L}$ and $\vec{S}$ is stronger than the coupling to the internuclear axis. In this case, $\vec{L}$ and $\vec{S}$ couple to form a resultant angular momentum $\vec{J}_a$, which precesses around the internuclear axis. The axial projection then has quantum number Ω. The rotational angular momentum $\vec{R}$ adds vectorially to $\vec{\Omega}$ to give the total angular momentum $\vec{J}$. The good quantum numbers for angular momentum are J_a, Ω and J_0.

Molecular states are denoted with a molecular term symbol

$$^{2S+1}\Lambda^{\pm}_{(\Omega)}. \tag{2.16}$$

The ± superscript refers to the symmetry under inversion in a plane containing the internuclear axis. The quantum number Λ is written Σ, Π, Δ,... for $\Lambda = 0, 1, 2, ...$ in analogy for s, p, d,... for atoms. The term value is often preceded by a term for an energy ordering analagous to the principle quantum number in atoms. These use X, A, B, C,... for singlet potentials ($S = 0$), and a, b, c,... for triplet potentials ($S = 1$), with the lowest (singlet) potential conventionally denoted X. For example, the ground state potential of ^{87}RbCs is written $X^1\Sigma^+$, while the lowest triplet potential is written $a^3\Sigma^+$.

If Hund's case (a) were perfectly applicable, there would be no coupling between the singlet and triplet states. Any electronically excited state which could be strongly coupled to the ground state (which is a pure singlet state) would have very weak coupling to the weakly-bound Feshbach states (which are predominantly triplet). This would make the large coupling strengths for STIRAP transfer unobtainable. However, it has been predicted [119, 120] that the spin-orbit coupling in heavy alkali dimers should mix the $A^1\Sigma^+$ singlet and $b^3\Pi$ triplet potentials. The Franck-Condon factors for the $A^1\Sigma^+ + b^3\Pi \rightarrow a^3\Sigma^+$ pump transitions and $A^1\Sigma^+ + b^3\Pi \rightarrow X^1\Sigma^+$ Stokes transitions are predicted to be high enough for the transfer, because the turning points of the potentials lie fortuitously above each other [119]. The possible candidates for the intermediate state are in the range 190 THz to 200 THz above the atomic threshold, or wavelengths between 1515 nm and 1590 nm for the pump transition. The ground state binding energy has been measured as 114.26816(5) THz [121], so the Stokes transition is then between 960 nm and 990 nm.

2.3.2 Rovibrational structure

The principal difficulty associated with cooling diatomic molecules is the extra degrees of freedom associated with rotation and vibration, and we will now discuss

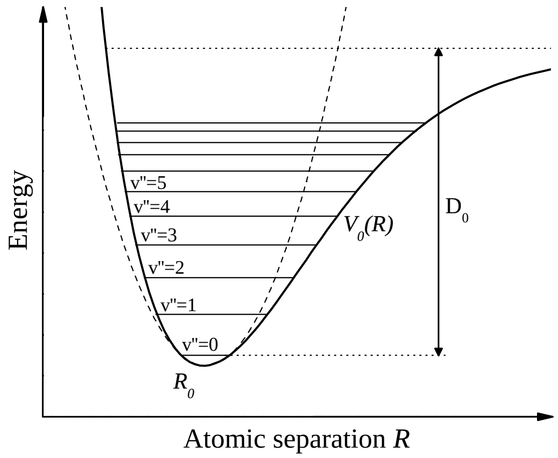

Figure 2.4: Vibrational levels of a diatomic molecule. Near the equilibrium separation R_0, the potential is approximately parabolic as shown in the dashed line.

these in detail. Here we will denote the rotation quantum number J, its projection onto the quantisation axis m_J, and the vibrational quantum number v.

Vibration

Consider the energy of the nuclear motion. If the electrons are bound to the molecule by a force F, the nuclei will be bound by an equal and opposite force. If we suppose this force is harmonic with a spring constant k, the frequency of the electron motion will be $\omega_E = \sqrt{k/M_e}$, while the nuclear motion will have $\omega_N = \sqrt{k/M_N}$. The ratio of the energies of the electronic and vibrational motion is then $E_N/E_e \approx \sqrt{M_e/M_N}$. The vibrational energy E_v is then approximately

$$E_v \approx \sqrt{\frac{M_e}{M_N}} E_e \tag{2.17}$$

Since M_e/M_N is typically $\sim 10^{-3} - 10^{-5}$, the vibrational energy is typically $\sim$ 100 times smaller than the electronic energy in equation 2.15 [115], or around $1 - 3$ THz.

In figure 2.4, we can see the ground-state internuclear potential of a diatomic molecule is approximately harmonic at the bottom of the well. Thus we can visualise the vibration of the molecules as a harmonic oscillator, with evenly spaced levels separated by some vibrational frequency ω_v. The $v'' = 0 \rightarrow v'' = 1$ spacing for ^{87}RbCs is ~ 1.5 THz [88, 122, 123]. The harmonic approximation breaks down for high vibrational levels as the potential becomes anharmonic, but the spacings have been measured to ±100 MHz by Fourier transform spectroscopy, and the highest vibrational level is $v'' = 136$ or $v'' = 137$. The $v'' = 0 \rightarrow v'' = 1$ vibrational spacing was measured as 1.49270 THz. [88].

Rotation

We can visualise the rotational structure with the model of a rigid rotor, where the distance between the nuclei of the molecule is fixed. This gives a series of rotational states with $E(J) = BJ(J+1)$, with rotational quantum number J. The rotational constant B can be calculated from the reduced mass of the molecule μ and the internuclear separation R [116], as

$$B = \frac{\hbar}{4\pi c \mu R^2}. \tag{2.18}$$

Using the masses of the individual atoms and taking the internuclear separation from the minimum of the potential in figure 2.2, we estimate $B = 0.5$ GHz. For ^{87}RbCs, the rotational constant has been measured as 0.49742275 GHz using Fourier transform spectroscopy in a heat pipe [88].

The higher vibrational states have a larger internuclear separation, so in general B decreases slightly as v'' increases [117]. In the lowest vibrational state, this effect is not relevant. However, when we remove the rigid rotor approximation, the rotation can cause centrifugal distortion by making the molecular bond stretch. This leads to a more general form of the rotational spacings (see chapter 9 of [124]):

$$E(J) = BJ(J+1) - DJ^2(J+1)^2 + HJ^3(J+1)^3 - ... \tag{2.19}$$

In some cases, it is possible to measure the higher order terms coming from the anharmonicity of the potential. Jennings *et al.* [125] have fitted terms up to $J^5(J+1)^5$ to the rotational transition frequencies in hydrogen fluoride, by measuring spacings up to $J = 32$ and taking advantage of the large rotational constant of 616 GHz.

If we approximate the bottom of the internuclear potential as harmonic with an oscillation frequency $\omega = 1.5$ THz, the $\mathcal{O}\left(J^3(J+1)^3\right)$ and higher terms are zero (see chapter 4 in [116]) and the centrifugal distortion D has the analytic form

$$D = \frac{4B^3}{w_v^2}. \tag{2.20}$$

We can estimate the centrifugal distortion in ^{87}RbCs. Using $B = 0.5$ GHz and $\omega_v = 1.5$ THz, we calculate $D \sim 200$ Hz, giving an 8 kHz correction to the $J = 0 \rightarrow J = 2$ spacing.

2.3.3 Hyperfine and Zeeman structure

We must also consider the hyperfine structure of the ground-state molecules. There is very little experimental data available for these splittings, because they are too small to resolve with most spectroscopic techniques, such as fourier transform spectroscopy [88]. However, the structure has been estimated theoretically by Aldegunde *et al.* [126]. They calculate the unknown coupling constants using density functional theory, and diagonalise the combined rotational, hyperfine, Zeeman and Stark Hamiltonian in several basis sets. The Zeeman structure of the ^{87}RbCs rovibrational ground state is shown in figure 2.2(c). The singlet states ($X^1\Sigma^+$) have no electronic angular momentum, so the Zeeman shifts arise from the interaction of the nuclear magnetic moments with the magnetic field. The mass of the nuclei is large compared to the mass of the electron, which makes the Zeeman shifts correspondingly much smaller than those in alkali atomic species. We see that the zero-field hyperfine splitting is $\sim$ 100kHz, and over a range of 200 G the Zeeman shifts are only $\sim$ 1 MHz. We can estimate that a magnetic field gradient of 5400 G/cm would be needed for magnetic levitation, far beyond the maximum gradient we can achieve in our experiment and the 30 G/cm needed to levitate the atoms. Thus in practical terms the molecule can be treated as having no magnetic moment, except for the high-precision spectroscopy in chapter 6 where the small Zeeman shift is accounted for in the ground-state binding energy.

2.4 Feshbach resonances and molecules

The first stage of our association process is magnetoassociation on a Feshbach resonance, so we must study the basic theory of Feshbach resonances. A full

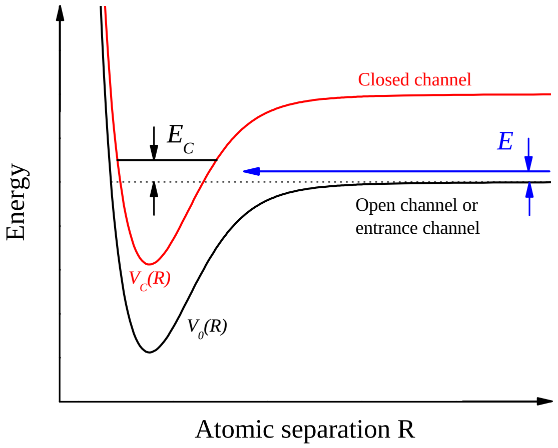

Figure 2.5: Basic two-channel model for a Feshbach resonance. Two atoms colliding at an energy E in the entrance channel resonantly couple to a molecular bound state of the closed-channel potential. For ultracold atoms, the collisions have nearly zero energy, $E \to 0$.

review of the theory of Feshbach resonances and magnetoassociation can be found in Chin *et al.* [21].

We consider two molecular potential curves as shown in figure 2.5. At large internuclear distances, free atoms at low energy (as in ultracold systems) are in the open, or entrance, channel. The second potential, referred to as the closed channel, supports molecular bound states with energies near that of the large-separation asymptote of the entrance channel.

A Feshbach resonance occurs when the molecular bound state has an energy close to the asymptote of the entrance channel. Then even weak coupling between the bound and unbound states can lead to strong mixing between the two channels. The energy difference E_C is typically tuned around zero by changing the magnetic field, if the states have different magnetic moments.

In all the cases relevant to this work, the atoms are in the “stretched“ state, $|F_{max}, m_F = F_{max}\rangle$, so collisions between atoms are purely triplet. The Feshback resonances and corresponding molecular bound states can have mixed singlet and triplet character, but the more commonly used broader resonances, and the states we consider in this work, have only a small amount of singlet character. [119]

A Feshbach resonance produces a pole in the scattering length, which is given by a simple function of the magnetic field B,

$$a(B) = a_{bg}\left(1 - \frac{\Delta}{B - B_0}\right) \tag{2.21}$$

with a width Δ, and the background scattering length a_{bg} which represents the off-resonant value and is directly related to the energy of the last bound vibrational level of the open channel potential $V_0(R)$ [21]. B_0 is the resonance position where the scattering length diverges to $a \to \pm\infty$. At the magnetic field $B = B_0 + \Delta$ the scattering length is zero. This means a Feshbach resonance can be used to tune the scattering length to any value, given sufficient control of the magnetic field. This technique has allowed the creation of BECs of Cs [77] and ^{85}Rb [127]. Tuning the scattering length through zero to small negative values has also allowed the formation of bright matter wave solitons [128, 129].

Feshbach resonances offer a way to create weakly bound molecules, from which a range of molecular states can be accessed by internal state transfer. The most common way to form Feshbach molecules is ramping an external magnetic field across a resonance. In a simplified picture, a Feshbach resonance consists of an avoided crossing between the entrance channel and the bound state of the closed channel. Ramping the field down across the resonance lets the atoms follow this crossing, to adiabatically convert atom pairs into molecules.

The molecular bound states and scattering lengths have been calculated theoretically by Jeremy Hutson's group at Durham University. The bound states are calculated using the BOUND [130] and FIELD [131] packages. The s-wave scattering lengths are obtained from coupled-channel calculations [132] using the MOLSCAT program [133], as modified to handle collisions in external magnetic fields [134]. These models have been throughly tested for ^{85}Rb [89], ^{85}Rb+Cs [90] and ^{87}Rb+Cs [66, 67], and give an excellent description of the scattering lengths, Feshbach resonances and high-lying bound states of Rb-Cs mixtures [66].

2.5 Trapping potentials

It is essential to understand the trapping potentials experienced by the ultracold atoms and molecules under study. Knowing the trapping frequencies allows us to measure phase-space densities and trap temperatures, while trap depths are essential to optimising evaporative cooling. By simulating the potentials experienced by our atoms and molecules, we open the possibility of measuring the molecular polarisabilities, which can be compared with theoretical models [135].

In our case, the main trapping potential is an *optical dipole potential*. We simulate our optical potentials with the model presented by Grimm *et al.* [136]. When an atom is placed in a light field, the electric field $\mathbf{E}$ induces an atomic dipole moment $\mathbf{p}$, which oscillates at the driving frequency of the light. For a light field with intensity I, the interaction potential of the induced dipole is then given by

$$U = -\frac{1}{2}\langle \mathbf{p} \cdot \mathbf{E} \rangle = \frac{1}{2\epsilon_0 c}\mathrm{Re}(\alpha)\, I \tag{2.22}$$

where α is the complex polarisability. The scattering rate, Γ_{SC}, of photons by the atoms is given by

$$\Gamma_{\mathrm{SC}} = \frac{1}{\hbar \epsilon_0 c}\mathrm{Im}(\alpha)\, I. \tag{2.23}$$

For the simplified case of a two-level atom, the form of the dipole potential is then

$$U_{\mathrm{dip}}(\mathbf{r}) = \frac{3\pi c^2}{2\omega_0^3}\frac{\Gamma}{\Delta} I(\mathbf{r}) \tag{2.24}$$

while the scattering rate is

$$\Gamma_{\mathrm{SC}}(\mathbf{r}) = \frac{3\pi c^2}{2\omega_0^3}\left(\frac{\Gamma}{\Delta}\right)^2 I(\mathbf{r}). \tag{2.25}$$

Δ is the detuning of the light from the transition frequency. We see that the dipole potential scales as I/Δ, whereas the scattering scales as I/Δ^2. It is therefore usually advantageous to use high intensities and large detunings to keep the scattering rate low for a certain trap depth. From equation 2.24 we also note that the potential can be attractive or repulsive. If the trapping light is red-detuned, *i.e.* $\Delta < 0$, then $U_{\mathrm{dip}} < 0$ and the atoms will be attracted to regions of high intensity. By contrast, a blue-detuned beam where $\Delta > 0$ will give $U_{\mathrm{dip}} > 0$ and the atoms will be attracted to regions of low intensity. A 3D harmonic potential can be made simply with a red-detuned (attractive) Gaussian beam. For lattice potentials, this means the atoms can be trapped at a minimum or a maximum of an interference pattern.

For a multi-level atom, the contributions of transitions to all the excited states must be included. In the case of alkali atoms, only a few levels contribute significantly. For molecules, a large number of rovibrational levels must be accounted for. For some bialkali species, the molecular polarisabilities have been calculated [135], including RbCs [137].

2.5.1 Lattice potentials

Ultimately we would like to load ultracold molecules into a three-dimensional periodic lattice potential, so we will take a brief look at the various types of lattice and how they are formed. A more complete review of lattice potentials can be found in [138]. In general, optical lattices are formed from the interference pattern between two or more beams. If we take the simplest case of two counter-propagating plane waves in the x-direction with wavelength λ, the interference pattern gives a potential

$$V(x) = V_0 \cos^2(\pi x/d) \tag{2.26}$$

with a lattice spacing $d = \lambda/2 = \pi/k$ and a lattice depth of V_0. Thus an ideal lattice can be characterised by two numbers: the lattice spacing d, and the lattice depth V_0, which is usually expressed in terms of the recoil energy

$$E_{\mathrm{R}} \equiv \frac{\hbar^2 k^2}{2m} = \frac{\hbar^2 \pi^2}{2md^2}. \tag{2.27}$$

This can be understood as the energy of an atom absorbing a single photon from the lattice. Often the dimensionless parameter $s = V_0/E_{\mathrm{R}}$ is used.

Making a power series around a potential minimum, the trapping frequency for a single lattice site is

$$\omega_{\mathrm{lat}} = \frac{\pi}{d}\sqrt{\frac{2V_0}{m}}. \tag{2.28}$$

For a typical dipole trap with a beam waist of $w_0 = 60$ µm we can achieve trapping frequencies of ∼ 100 Hz. In a lattice where the spacing is typically $d \sim 500$ nm, trap frequencies of ∼ 10 kHz are easily achievable.

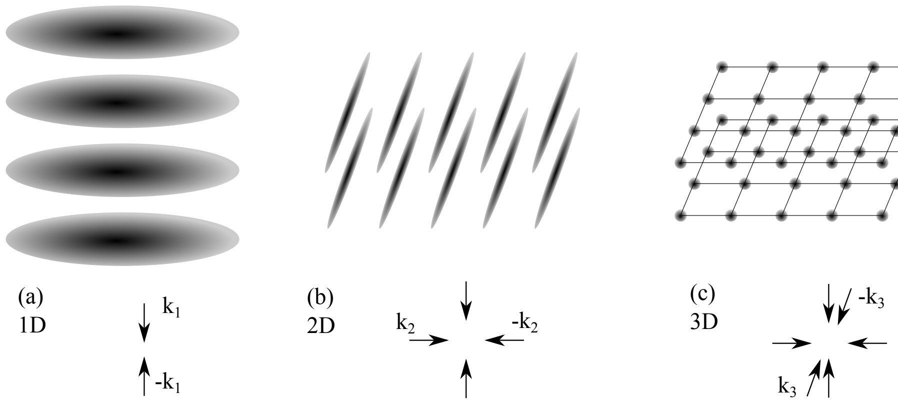

Figure 2.6: 1D, 2D and 3D lattice geometries. A single pair of beams forms a 1D lattice, or a stack of "pancake" sheets. Two pairs of beams form a 2D lattice of "tubes". A third pair of beams forms a 3D lattice of points.

The interference pattern created by three or more such laser beams is in general rather complicated and depends on the geometry, polarisation, frequency and relative phases of the beams. This can create a wide variety of lattice geometries [138, 139], but simple geometries can be made by building the lattice from pairs of independent beams. This can be achieved by introducing a frequency offset of tens of MHz between the pairs of lattice beams, usually with AOMs. Interference effects between the pairs is then washed out because the potential changes much faster than the oscillation frequency of the atoms in the lattice wells.

This technique can be used to create 2D or 3D periodic potentials. The case above of one pair of counterpropagating beams creates a stack of "pancake" traps, as shown in figure 2.6(a). If another pair of counterpropagating beams is added orthogonal to the first pair, the interference forms a grid of elongated "tube" traps, *i.e.* a 2D lattice as in figure 2.6(b). A third pair of orthogonal beams forms a 3D cubic array of points as in figure 2.6(c).

Chapter 3

Laser system for STIRAP

In this chapter, we will discuss the design and characterisation of the laser system we use for transfer of the Feshbach molecules to the ground state. We offset-lock two lasers to a high-finesse optical reference cavity, narrowing the linewidth to < 1 kHz, and align them to a 35 μm focus at the atomic cloud to achieve the necessary intensities. We also develop robust methods to create arbitrary, well-defined pulse sequences suitable for STIRAP.

Molecules in the near-dissociation "Feshbach" states have a large interatomic separation, and so have a negligible electric dipole moment and a relatively short lifetime due to collisions in the ultracold gas. This necessitates transfer of the molecules to the ground state. This is done by coupling both the initial weakly-bound Feshbach state $|F\rangle$ and the rovibrational ground state $|G\rangle \equiv |v'' = 0, J'' = 0\rangle$ to a common excited state $|E\rangle$. This requires two lasers, hereafter referred to as the pump and Stokes lasers as shown in figure 2.2. A suitable pulse sequence for STIRAP begins with only the Stokes light illuminating the molecules. This first counterintuitive step initializes the molecules in a dark state $|D\rangle$ as defined by

$$|D\rangle = \cos\theta\,|F\rangle - \sin\theta\,|G\rangle\,, \qquad \tan\theta = \frac{\Omega_{\mathrm{p}}(t)}{\Omega_{\mathrm{S}}(t)} \tag{3.1}$$

where $\Omega_{\mathrm{p}}(t)$ and $\Omega_{\mathrm{S}}(t)$ are the Rabi frequencies of the pump and Stokes transitions respectively. Ramping the intensity of the Stokes laser down and the pump laser up changes these Rabi frequencies and hence the mixing angle θ, which determines the composition of the dark state. In particular, with the appropriate pulse sequence the dark state can be adiabatically transformed from state $|F\rangle$ to state $|G\rangle$, producing molecules in the rovibrational ground state [22]. Typically the sequence is then reversed to transfer the molecules back to the Feshbach state for dissociation and detection.

In section 2.2.1 we saw the conditions for efficient STIRAP transfer:

$$\frac{\Omega_0^2}{\pi^2\gamma} \gg \frac{1}{\tau} \gg D. \tag{3.2}$$

Here, γ is the natural linewidth of the state $|E\rangle$, D is the linewidth associated with the frequency difference between the two lasers, τ is the transfer time and $\Omega_0 = \sqrt{\Omega_\mathrm{p}^2 + \Omega_\mathrm{S}^2}$ is the reduced Rabi frequency.

The natural linewidth is dependent on the excited state chosen; the range of values for this term is therefore limited by the range of states accessible to the laser system. The importance of this term in defining the efficiency of the transfer highlights the need for a thorough molecular spectroscopy search to identify the best state to use, namely a state with high Ω_0^2/γ. This gives the first criterion which our laser system must fulfil: it must be possible to tune both of the lasers over a wide overlapping frequency range to maximize the range in which a suitable excited state can be found.

In practice, Ω_0^2/γ is limited by the available laser intensity. This sets the minimum required duration of the transfer to remain adiabatic. This in turn sets the maximum linewidth allowed to maintain coherence of the dark state. Therefore, the second criterion is that the linewidth of each of the lasers must be suitably narrow such that the linewidth associated with the frequency difference between the two lasers is minimized. In our experiment we find transitions which allow pulse durations on the order of ~ 10 μs. This indicates that the maximum linewidth for efficient transfer must be on the order of kHz.

3.1 Design of the laser system

We now turn to the practical details of the laser system for STIRAP. This must consist of two narrow-linewidth laser light sources. The frequency between these

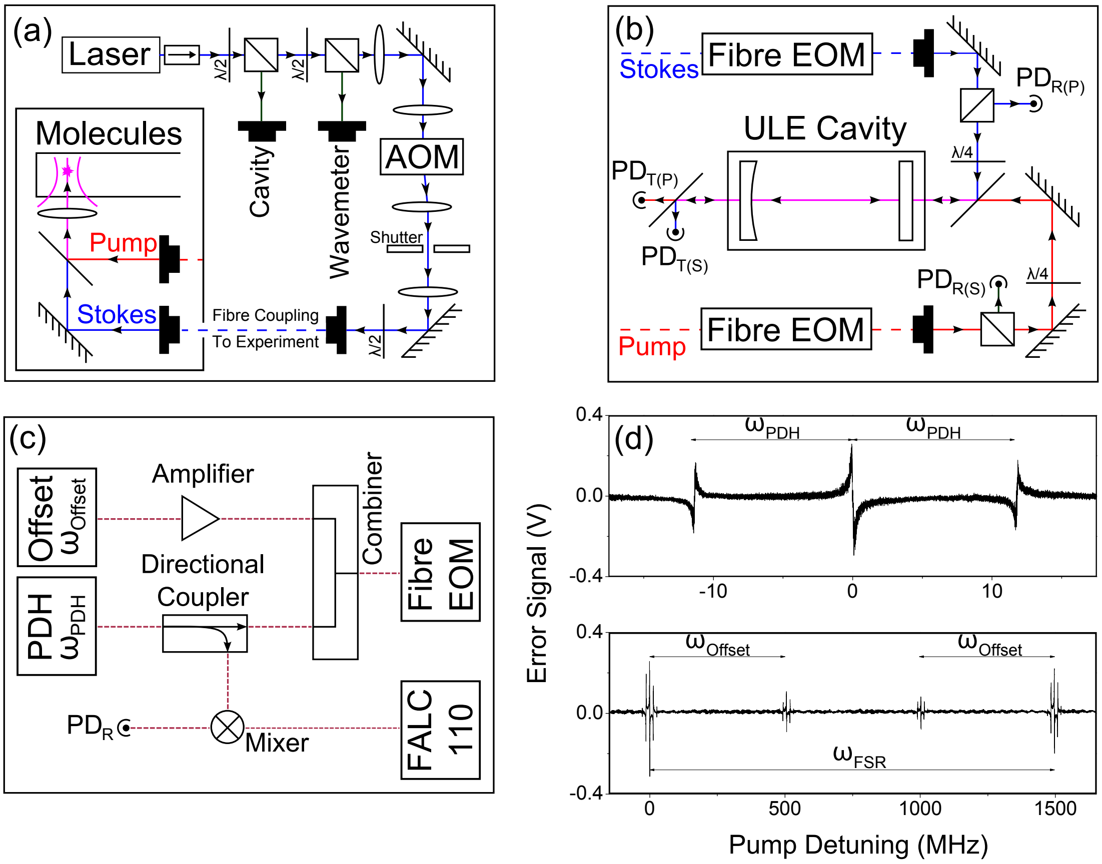

Figure 3.1: STIRAP laser system (a) Experimental coupling setup for the 977 nm Stokes laser. An identical setup for the 1557 nm pump laser is not shown. (b) Optical setup for frequency stabilization to the cavity, including the fibre-coupled electro-optic modulators (EOMs) providing the Pound-Drever-Hall (PDH) and offset modulation signals. (c) The PDH and offset electronics for the pump laser. Note the fibre EOM provides both the PDH and offset modulations, removing the need for free space EOMs. The directional coupler which is used to split the PDH modulation signal is a Minicircuits ZDC-20-3, and the mixer is a Minicircuits ZFM-150+. The resultant error signal is sent to a Toptica FALC 110 fast analogue servo module. The Stokes setup is identical except for the amplifier (Minicircuits ZKL-1R5), which is removed. (d) PDH error signal scanning the pump laser frequency over short (upper) and long (lower) ranges.

two sources is required to be relatively large ($\sim$ 100 THz) and equal to the binding energy of the molecule. This can be achieved by stabilizing the laser frequencies to an optical frequency comb [78], multiple independent cavities [24] or a single cavity [140]. In the case of frequency stabilization to an optical cavity, there are two approaches. The length of the cavity may be actively stabilized by referencing back to a frequency comb [24], or an atomic reference [141, 142]. Alternatively, the need for an optical reference can be removed by relying on the passive stability of an ultra-low-expansion (ULE) glass cavity maintained at the zero expansion temperature of the glass [140]. Typically, a tunable frequency source is then generated by using the output of another laser which is offset-locked to the frequency stabilized laser via an optical phase-locked loop [140].

Our system uses a pair of Toptica DL Pro external cavity diode lasers at 1557 nm and 977 nm for the pump and Stokes transitions respectively. Light from each laser goes through an optical isolator (40 dB) before being split by polarizing beam splitters and coupled into three fibres leading to the main experiment, a wavemeter and an optical cavity, as shown in figure 3.1 (a). Both lasers are referenced to the same cylindrical 100 mm plane-concave optical cavity to narrow the linewidth. The cavity (ATFilms) is constructed from ULE glass, and is mounted in a temperature stabilized vacuum housing from Stable Laser Systems. The temperature of the cavity is maintained at 35 °C, the zero-expansion temperature of the ULE glass. Further key properties of the reference cavity are listed in table 3.1.

3.2 Offset cavity locking

In this section we will discuss the method we use to continuously tune the lasers. We use a pair of fibre-coupled EOMs to stabilise the lasers to a tunable frequency offset from a mode of the reference cavity.

Each beam sent to the cavity passes through an optical fibre-coupled electro-optic modulator (EOM). The output of each EOM (Thorlabs LN65S-FC for 1557 nm, EOSpace PM-0K5-10-PFA-PFA-980 for 977 nm) is then coupled via a fibre and mode-matching optics to the optical cavity. Dichroic mirrors at either end of the cavity (Thorlabs BB1-E03P 750 - 1100 nm, and Thorlabs DMLP1180R) are

	Stokes (977 nm)	**Pump** (1557 nm)
Mirror Radius 1	∞	
Mirror Radius 2	500 mm	
Zero-Expansion Temperature	35 °C	
Length	100.13958(7) mm	100.15369(7) mm
Free Spectral Range	1496.873(1) MHz	1496.662(1) MHz
Finesse	$1.37(6) \times 10^4$	$1.19(6) \times 10^4$
Mode Linewidth	109(5) kHz	126(5) kHz

Table 3.1: Key properties of the single ultra-low expansion cavity (ATFilms) to which both the pump and Stokes lasers are referenced. The data presented in this table are extracted from the results presented in figure 3.3.

used to combine the two different wavelengths of light entering the cavity, and to separate the two wavelengths following transmission or reflection. The transmitted and reflected beams are monitored on photodiodes, and the signal generated by the reflected light is sent to the locking electronics. The full optical setup is shown in figure 3.1 (a) and (b). The frequency stabilization electronics are a standard Pound-Drever-Hall (PDH) setup as has been explained in [143], where the EOM is driven at a frequency $\omega_{\mathrm{PDH}} \sim 10$ MHz to generate the PDH readout signal (figure 3.1 (d)). This error signal is sent to a fast analogue servo module (Toptica FALC 110) which is integrated into the control electronics in each laser.

The fibre-coupled EOMs are crucial to the simplicity and flexibility of our setup. These modulators are non-resonant and hence work over a wide bandwidth of $\sim$ 10 GHz. Additionally, these devices can be driven simultaneously at multiple frequencies and require relatively small driving voltages ($\sim$ 4.5 V). We use these EOMs to provide continuous tunability of the laser frequency sent to the main experiment. By applying a modulation frequency ω_{Offset} to each EOM we add high-frequency sidebands to the original carrier light (figure 3.1 (d)). By stabilizing the frequency of a sideband to a cavity mode, we are then able to precisely tune the frequency of the carrier light by simply changing the modulation frequency, ω_{Offset}. Due to the high bandwidth of the EOMs, ω_{Offset} may be larger than the free spectral

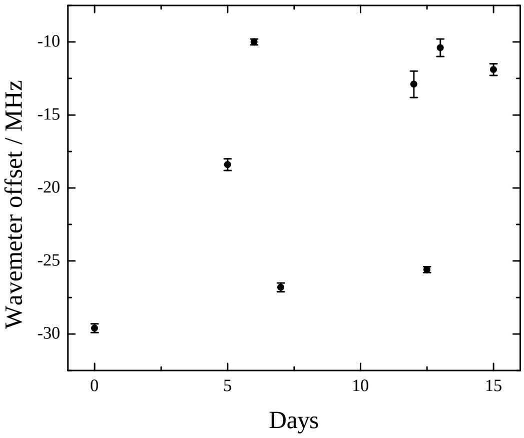

Figure 3.2: Accuracy of the wavemeter, measured with an atomic transition. A laser is tuned to the $5P_{3/2} \rightarrow 4D_{5/2}$ transition at 1529.261 nm in rubidium and the transition frequency is recorded on a Bristol 621A wavemeter. Here we see the difference from the precisely known literature value [144]. From this we estimate that the wavemeter has an accuracy of 20 MHz.

range of the optical cavity ω_{FSR}. Hence, the frequency of the carrier light can be tuned continuously to any point between the modes of the cavity.

The Pound-Drever-Hall technique used to stabilize the frequency of a sideband to a cavity mode requires further modulation of the light at a frequency ω_{PDH}. We accomplish this using the same non-resonant EOMs already discussed by combining the sideband offset and PDH modulation frequencies on an RF combiner (Minicircuits ZFSC-2-2-S+) and driving each EOM at two RF frequencies simultaneously, as shown in figure 3.1 (c).

Isolating the optical cavity from vibrations is typically critical in experimental systems such as this for achieving high efficiency STIRAP. Our cavity is placed on a breadboard on top of a Sorbothane® mat, which is inside a wooden box lined with sound-proofing foam (30 mm thick). The whole assembly is placed on an optical table (without a vibration isolation platform) in the same room as the main experiment itself. We neglect further isolation in part because we find that the part of the apparatus most sensitive to vibrations is not the cavity itself but instead the EOM and the accompanying fibres.

Measurement of the absolute wavelength of each laser for each transition shown in table 4.1 is done with a single wavemeter (Bristol 621A) to which both lasers are coupled. We estimate the accuracy of the wavemeter by comparing it to the $5P_{3/2} \rightarrow 4D_{5/2}$ transition in Rb at 1529 nm. A first laser is locked to the $5S_{1/2}(F = 2) \rightarrow 5P_{3/2}(F = 3)$ closed cooling transition at 780 nm using frequency modulation spectroscopy. The pump laser is then tuned to the $5P_{3/2}(F = 3) \rightarrow 4D_{5/2}$ transition at 1529 nm. 60 μW of 780 nm light and 56 μW of 1529 nm light are copropagated through an 8 cm Rb vapour cell. We observe the transmission of the 780 nm light, which increases on 2-photon resonance because the closed lower transition is opened by multiphoton decay from the upper $4D_{5/2}$ state to the $5S_{1/2}(F = 1)$ ground state, reducing the population in the $5S_{1/2}(F = 2)$ ground state. This process is known as double-resonance optical pumping spectroscopy, and shows better signal-to-noise than simply measuring the absorption of the 1529 nm beam [145]. We show a comparison over several weeks between the known frequency as measured with a frequency comb [144] and our wavemeter reading in figure 3.2. This shows the absolute accuracy of the wavemeter is limited to around 20 MHz.

We have also measured the long term stability of the laser frequency by reference to an optical frequency comb (for details see chapter 6). This has revealed a root mean square deviation in the frequency deviation of the beat signal over a time period of 24 hours of 116 kHz, as shown in figure 3.4. It is worth noting that in our experiment, it typically takes $1 - 2$ hours to map out a molecular transition and we have been able to observe transitions with widths of $\sim$ 200 kHz. In chapter 6 we use this frequency comb to make a $\sim$ 10 kHz-precision measurement of the pump-Stokes frequency difference and thus the molecular binding energy.

3.3 Measuring the cavity free spectral range

In this section, we develop a simple, novel method to measure the free spectral range of the cavity using the fibre-coupled EOMs. The accuracy with which we can measure the relative frequency between transitions found using this laser system is only limited by the uncertainty with which we can measure the free spectral

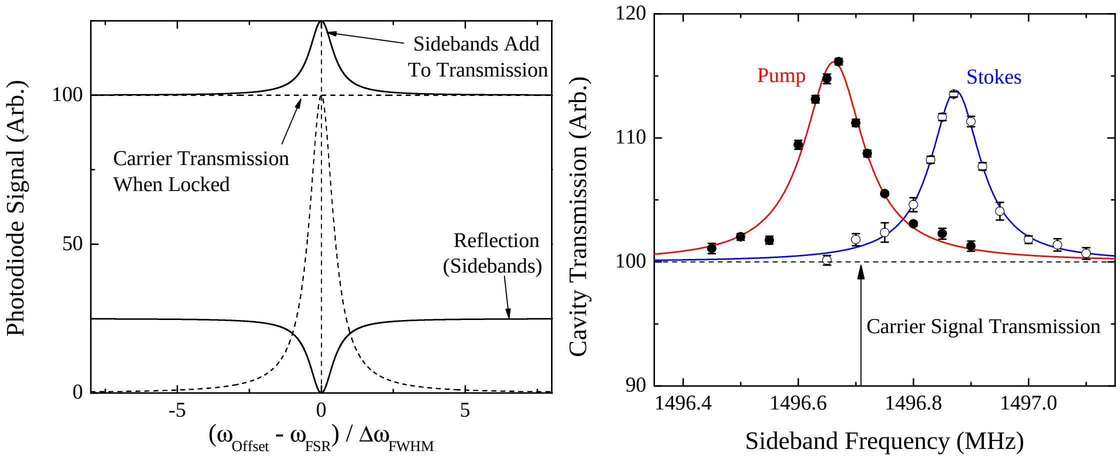

Figure 3.3: Measurement of the free spectral range of the optical cavity, ω_{FSR}. (a) The carrier frequency is stabilized to a cavity mode (dashed line). We use a non-resonant EOM to produce sidebands at a frequency ω_{Offset} away from this cavity mode. Light in the sidebands is reflected by the cavity, except when $\omega_{\mathrm{Offset}} = N \times \omega_{\mathrm{FSR}}$ where N is an integer. In this case, the sideband light is transmitted along with the carrier light and we observe increased transmission through the cavity. By measuring the frequency at which we achieve peak transmission through the cavity as we sweep the sideband across a neighbouring cavity mode (such that $N = 1$), we can therefore directly measure ω_{FSR}. (b) Experimental measurement of the cavity free spectral range using this method. Results for the cavity transmission are shown with Lorentzian fits at wavelengths of 1557 nm (filled circles) and 977 nm (empty circles). Note the difference between the peak positions, which is from the thickness of the inner (980 nm) mirror coating. As the linewidth of our lasers is ∼3 orders of magnitude less than the cavity linewidth, we can extract the linewidth of the cavity at each wavelength from the width of the Lorentzian fits.

range of the cavity. Fortunately, the fibre-coupled EOMs provide a simple, yet accurate method of measuring this quantity. By stabilizing the frequency of the carrier light to a cavity mode, the addition of sidebands which are not resonant with a cavity mode reduces the light transmitted through the cavity. However, if we set the offset modulation frequency ω_{Offset} such that the sideband overlaps with an adjacent cavity mode, *i.e.* $\omega_{\text{Offset}} = N \times \omega_{\text{FSR}}$, the light in the sideband will once again be transmitted through the cavity. We hence scan the offset modulation frequency and monitor the intensity of the light transmitted through the cavity to measure the position of peak transmission, as shown in figure 3.3. The laser frequency is stabilized to a cavity mode throughout the measurement, using the PDH lock explained in section 3.2. This lock narrows the linewidth of the laser to ~ 3 orders of magnitude less than the cavity linewidth (see section 3.6). The width of the transmission peak observed therefore yields the linewidth of the cavity. A Lorentzian fit to the data allows the measurement of both the free spectral range and the linewidth of the cavity at each wavelength, as documented in table 3.1. We note that the length of the cavity differs by 14.1(1) µm between the two wavelengths, corresponding to the thickness of the inner (977 nm) coating on the cavity mirrors. Initially we believed a ~ 1 kHz measurement of the free spectral range would let us extrapolate the exact cavity mode number between the two wavelengths and thus the ~ 100 THz frequency difference between them, but the difference in length makes this impossible. We could improve the precision by at least an order of magnitude by referencing the drive frequency to GPS, taking much more data and tuning the sideband through a more distant cavity mode (the EOM will work for at least $N = 6$). However, the 1 kHz is smaller than the precision to which we can measure our molecular transitions, so more precise measurements of the FSR were unnecessary.

Light from both lasers is carried to the experimental table in 8 m single-mode polarisation-maintaining fibres. After the fibres, the two beams are collimated with achromatic doublet lenses to a ~ 4 mm radius and combined on a dichroic mirror (Thorlabs DMLP1180L), and focussed ($f = 300$ mm) to a waist of 37.7(1) µm (pump) and 35.6(6) µm (Stokes) at the position of the trapped molecules. The system provides up to 16 mW of each wavelength of light at the position of the molecular sample. We measure the beam sizes directly as a function of position

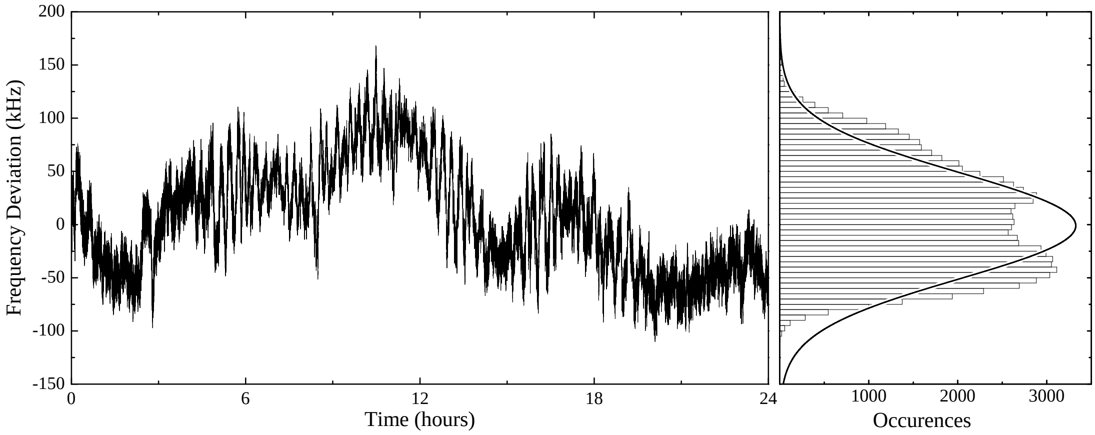

Figure 3.4: Measurement of the stability of the laser by reference to an optical frequency comb. (a) Frequency deviation of the beat note between the pump laser system and a frequency comb tooth, recorded on a counter over a 24-hour period. (b) Histogram of the same data. A Gaussian curve with a full-width half-maximum of 120 kHz is shown for comparison.

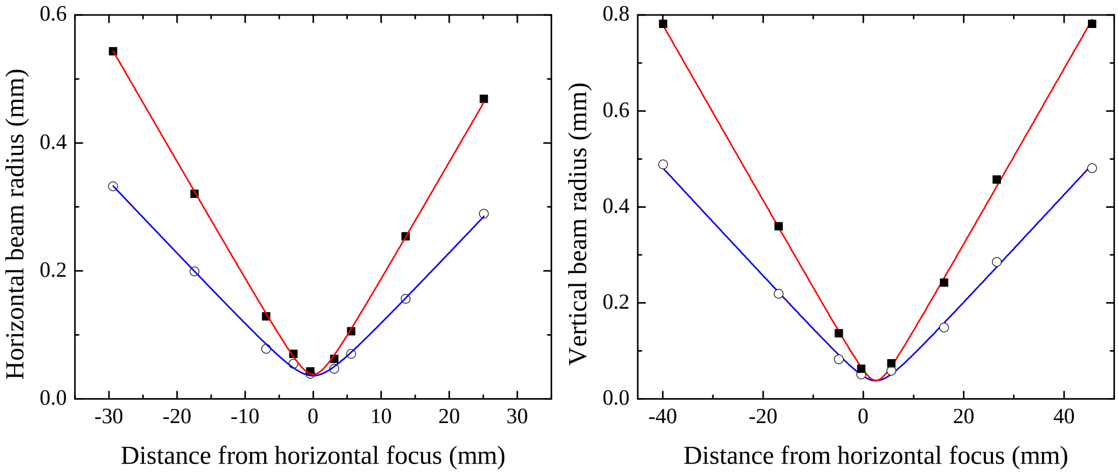

Figure 3.5: $1/e^2$ radius of the STIRAP lasers around the focal point. Closed squares and open circles are the pump and Stokes beams respectively. Note the astigmatism, causing a 2.5(2) mm displacement between the vertical and horizontal focuses. The fit lines are standard Gaussian beam profiles as in equation 3.3.

along the beam using a translating knife edge and fit the equation

$$w(z) = w_0\sqrt{1 + \frac{z^2}{z_R^2}} \tag{3.3}$$

where $z_R = \pi w_0^2/\lambda M^2$ and M^2 is an empirical parameter for the deviation from a perfect Gaussian beam. This gives waists of $w_0 = 39(2)$ µm and $w_0 = 36.2(7)$ µm for the pump and Stokes beams respectively. The more precise waists given above are from separate measurements (not shown here) at the focuses in figure 3.5. From this we calculate $M^2 = 1.4(1)$ and $M^2 = 1.3(1)$ for the pump and Stokes respectively. We see the beam is astigmatic, giving a 2.5(2) mm offset between the horizontal and vertical focuses. This is important in section 5.3 when calculating the normalised Rabi frequencies.

3.4 Intensity control

In this section, we will discuss how we modulate the laser intensity for STIRAP, and the program we use to produce arbitrary, easily altered pulse sequences.

For molecular spectroscopy and STIRAP, we generate pulses of light at each wavelength by passing each beam destined for the main experiment through separate acousto-optic modulators (AOM). The AOMs (ISOMET 1205C-1023 for 1557 nm, ISOMET 1205C-1 for 977 nm) are driven at their centre frequency of 80 MHz, using fixed frequency drivers with a $0 - 1$ V input for amplitude modulation. By controlling the amplitude of the AOM driving frequency using a signal supplied by an arbitrary waveform generator (AWG, Agilent 33522B), the power diffracted into the first order may be controlled to create pulses of arbitrary shape. To improve the stability of the AOM response against thermal effects, the AOMs are kept active during the rest of the experimental cycle and the light is instead blocked by a shutter.

We make our spectroscopy pulses with an arbitrary waveform generator (AWG) which is programmed in LabVIEW. In principle this is a simple task: we upload an arbitrary list of voltages to the AWG, and it iterates through them at a constant rate. However, we wish to define the pulse shape programatically, so they can be reproduced and altered easily. In chapters 4 and 5 we use a wide variety of pulse shapes, and often an experiment involves changing the pulse timing from shot to shot. Thus a system to change the pulse shapes quickly and easily can dramatically simplify many experiments. One can imagine choosing the pulse shape from a list of mathematical functions – cosine, Gaussian, square *etc.* – but this would restrict the possible experiments. For example, the pulses to measure the Stokes Rabi frequency (figure 5.3(b)) correspond to no simple mathematical form and must be assembled piecewise. To this end, we have designed a LabVIEW program with a simple, reliable user interface to build arbitrary voltage arrays and upload them to the AWG.

The program is built with a highly modular structure. The top-level host program handles the user interface, while the pulse shapes and communication with the AWG are handled by separate LabVIEW VIs (subroutines in distinct files). The modular structure means it can be adapted for any AWG without changing the code defining the pulse shapes. The program can also account for the nonlinear response of the AOM, allowing the user to program Rabi frequency profiles directly, though this feature is not currently in use and has not been tested. The program has also been adapted for remote control by the main FPGA experimental control program (see section 1.5.4).

Each of our pulse shapes is defined by a separate LabVIEW VI. The host program calls a pulse shape VI chosen by the user. This pulse shape VI passes an array of parameter name strings (“*pulse length*”, “*start time*”, *etc.*) to the host program for display. The user gives values for each of these parameters, and these are passed to the pulse shape VI. This calculates the appropriate pulse sequence from the parameters, and returns an array of Rabi frequencies to the host, which uploads them to the AWG through a separate subVI.

This apparently complex structure means the pulse design can be switched quickly and with no programming skill, because the pulse shape VI and parameters can be chosen while the host VI is running. Designing new pulses needs only basic LabVIEW programming skills, as a template pulse shape VI can be resaved and the code specifying the pulse shape rewritten. This system has been in daily use for over two years with no issues and has proved to be effective and reliable.

The maximum length of the pulse sequence is 1 million sample points, set by the AWG memory. This allows a maximum sequence length of 1.6 s before the sample rate interferes with the STIRAP transfer as in figure 5.8. For the lifetime measurements in section 5.9, we need a way to increase the hold time between the forward and reverse STIRAP transfer beyond this limit. We therefore add a circuit which uses a pair of DG419 integrated circuit analog switches to swap the channels on the AWG. After we transfer the molecules to the ground state, we swap the channels and repeat the same voltage ramps, giving a reversed intensity ramp from the AOMs and hence transferring the molecules back to the initial Feshbach state. With this technique, there is no practical limit to the length of the hold time in the ground state.

3.5 Alignment

Here we discuss alignment of the $\sim 36\ \mu\text{m}$ beams to the optical trap, which is a non-trivial problem, and we develop specific techniques to achieve this. It is essential to align the beams to within a small fraction of the beam size, to ensure the highest intensity for STIRAP. Resonant light at 852 nm or 780 nm is not useful as the fibres taking light to the experimental table are not single-mode at these wavelengths. Instead, the pump and Stokes beams are initially overlapped with a knife edge, so that a single mirror mount moves both focuses in tandem. We then align the STIRAP beams to the atoms by using the Stokes beam as an optical trap, since with magnetically levitated ^{87}Rb atoms the Stokes beam can form a trap with a depth around 1.4 μK. We leave the Stokes beam on while loading atoms into the 1550 nm crossed trap as normal, and then ramp the crossed trap off to leave atoms trapped in the Stokes beam. This method aligns the beams accurately enough to get a 1-photon spectroscopy signal, on a strong molecular transition at the maximum pump power available. We fine tune the alignment by adjusting the beam position to minimise the pump power and pulse length needed to remove the molecules.

Both pump and Stokes beams are aligned simultaneously using a single mirror. Initially we used the 1/4”-80 adjusters provided with the kinematic mirror mount,

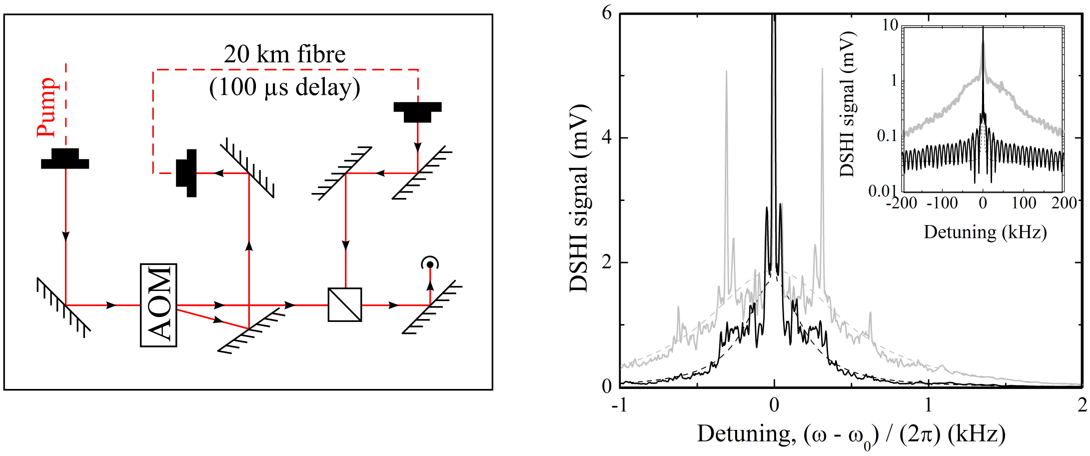

Figure 3.6: Delayed self-heterodyne measurement of the laser linewidth. (a) Optical layout used for the self-heterodyne linewidth measurement. (b) Self-heterodyne beatnote for the pump laser. Black and grey lines show linewidths of 0.21(1) kHz and 0.52(2) kHz achieved with the main experiment turned off and on respectively. Two additional large spikes at ±310 Hz can be observed when the experiment is switched on indicating the presence of acoustic noise. Inset: the same data over a wider frequency range with a logarithmic amplitude scale, showing the characteristic DSHI interference fringes (black), and the linewidth of the free-running laser (grey) for comparison. This measurement is relatively insensitive to noise below 10 kHz because of the limited delay line length of 100 µs.

but these did not give the precise adjustment needed. We therefore replaced the adjusters with differential micrometer screws (Thorlabs DM22), which use a pair of oppositely-handed threads to create a movement of just 25 µm/turn, with 0.5 µm increments possible. This means the focus moves by just 235(3) µm/turn, precise enough to align the STIRAP beams to within ±5 µm. We have seen no effect of backlash in the adjusters, with the optimal alignment position identical whether the adjuster is turned clockwise or anticlockwise during the adjustment process.

3.6 Delayed self-heterodyne measurement of the laser linewidth

We estimate the linewidth of the pump laser using delayed self-heterodyne interferometry (DSHI) [146]. In this method, laser light from the system is separated into two paths, and one of these paths is frequency shifted and time delayed with respect to the other. The paths are then recombined to create a beat note, from which we can estimate the loss of phase coherence. To achieve this, we deliver light from the pump laser through a 2 m single mode fibre to an AOM driven at an angular frequency $\omega_0 = 2\pi \times 80$ MHz. The first order diffracted light from the AOM is delayed by 100 µs by a 20 km single mode fibre before being recombined with the light from the zeroth order. The resultant beat note is measured on a high-speed photodiode as shown in figure 3.6 (a).

In an idealized DSHI experiment, the delay time τ between the two paths should be significantly more than the coherence time of the laser τ_{c}, so that there is no correlation between the noise in the two arms of the interferometer [147]. However, it is still possible to get useful information about the linewidth even when $\tau < \tau_{\mathrm{c}}$. In this case, the beat note measured on the photodiode following recombination contains lineshapes resulting from both correlated and uncorrelated noise contributions. If we consider a laser with a constant (white) noise spectrum and power P_0, this DSHI power spectrum has the analytic form [147]

$$\begin{aligned} S_{\mathrm{DSHI}}\left(\omega,\tau\right) &= \frac{\frac{1}{2}P_0^2\tau_{\mathrm{c}}}{1+(\omega-\omega_0)^2\tau_{\mathrm{c}}^2}\left(1-e^{-\tau/\tau_{\mathrm{c}}}\left[\cos[(\omega-\omega_0)\tau]+\frac{\sin[(\omega-\omega_0)\tau]}{(\omega-\omega_0)\tau_{\mathrm{c}}}\right]\right) \\ &+ \frac{1}{2}P_0^2\pi e^{-\tau/\tau_{\mathrm{c}}}\delta(\omega-\omega_0). \end{aligned} \tag{3.4}$$

The structure of this spectrum consists of a Lorentzian with full-width half-maximum defined by $1/(2\pi\tau_c)$ superimposed with interference fringes with a period $1/(2\pi\tau)$ arising from partial coherence between the two paths, and a δ-function at the AOM frequency. For the limiting case of a long delay time where no coherence remains between the paths, $\tau/\tau_c \to \infty$, the power spectrum is simply a Lorentzian curve whose width is set by the laser linewidth. For $\tau/\tau_c \to 0$ this reduces to a δ-function as frequency fluctuations between the two paths become perfectly correlated.

In our system the laser is frequency stabilized to a cavity, so below the servo loop bandwidth the phase noise of the laser is suppressed. This non-uniformity means that we cannot assume that the white noise model gives a good estimate of the coherence time. However, numerical simulations by Di Domenico *et al.* [148] have shown that the lineshape of such a laser is still approximately Lorentzian, and comes from the part of the individual frequency noise components of each path which exceeds $8\ln(2)/\pi^2$ multiplied by their respective Fourier frequencies, known as the β-separation line. Other parts of the noise spectrum contribute to a wide pedestal without affecting the full-width half-maximum of the lineshape. Hence, a reasonable estimate of the linewidth can still be achieved using the same functional form as equation 3.4.

The measured self-heterodyne beat note of the laser (with the AOM frequency removed) is shown in figure 3.6. The inset shows the same signal over a larger span with interference fringes as predicted in equation 3.4. For our setup we expect $\tau/\tau_c \sim 0.1$ and around this value the oscillatory term is reasonably flat in the range of 2 kHz from the centre. We also note that in our measurement, the δ-function will be broadened due to the limited resolution bandwidth (R) of our spectrum analyser (Agilent N9320B). The δ-function can therefore be replaced with an appropriately normalized Gaussian and the fringes can be neglected:

$$S_{\mathrm{DSHI}}(\omega) = \frac{\frac{1}{2}P_0^2\tau_c}{1+(\omega-\omega_0)^2\tau_c^2} + \sqrt{\frac{\pi}{8}}\frac{P_0^2}{R}\exp\left[-\frac{1}{2}\left(\frac{\omega-\omega_0}{R}\right)^2\right]. \qquad (3.5)$$

Fitting to this equation over a range of 2 kHz suggests a laser linewidth of 0.21(1) kHz. However, when the equipment used in the rest of the experiment was turned on the linewidth increases to 0.52(2) kHz. The main contribution to this noise is acoustic, coming from the large power supplies used to drive the magnetic field coils for the experiment, with smaller contributions from the water cooling pump and the fibre laser used in the optical dipole trap. For comparison, the free-running laser linewidth is measured to be 85(8) kHz as shown inset in the left panel of figure 3.6 (b). This measurement is much closer to the idealized DSHI case as the coherence time of the laser is much shorter.

An independent analysis of the DSHI spectrum for the same experimental setup was performed using proprietary phase noise reconstruction software [149]. This yielded a linewidth around 200 Hz which agrees well with the reading from the spectrum analyser. It should be noted neither analysis is a full measurement of the linewidth since the 100 µs delay in the DSHI method acts as a 10 kHz high-pass filter, reducing sensitivity at low frequencies. A full measurement by comparison with a second identical system would be prohibitively expensive.

3.7 Conclusions

In this chapter, we described the laser system we use for STIRAP transfer of molecules to the ground state. We stabilised two lasers to a single high-finesse reference cavity. We found a long-term stability of $\sim$ 120 kHz, and we used delayed self-heterodyne interferometry to estimate a linewidth of 200 Hz. We developed methods to align both beams precisely to a narrow focus at the molecular sample, and built a versatile system to create arbitrary, easily changed two-colour pulse sequences. This puts us in an excellent position for molecular spectroscopy and transfer of molecules to the ground state using STIRAP, which we will discuss in the next chapters.

Chapter 4

Molecular spectroscopy

In this chapter, we study the molecular transitions for STIRAP. We use the laser system from chapter 3 to locate several transitions, and identify a suitable intermediate state for the STIRAP transfer. We use two-photon spectroscopy to study the rovibrational ground state of ^{87}RbCs and measure the rotational constant. We apply electric fields and use Stark spectroscopy to measure the electric dipole moment of the ^{87}RbCs molecule.

To implement STIRAP, the pump and Stokes lasers need to be tuned such that they couple the initial weakly-bound state and the rovibrational ground state to a common excited state. In our system this corresponds to a range of states lying between ~ 1530 nm and ~ 1565 nm above the dissociation energy of the molecule as shown in figure 2.2. Detailed spectroscopy of the mixed $A^1\Sigma^+ + b^3\Pi$ molecular potential, by Debatin *et al.* [142], has identified the lowest hyperfine sublevel of the $|E\rangle \equiv |\Omega' = 1, v' = 29, J' = 1\rangle$ state as suitable for efficient ground state transfer in this region. Our laser system therefore needs to be able to access the transitions to this common state. To demonstrate the capabilities of our laser system, we perform molecular loss spectroscopy on seven of the electronically excited states previously identified, including the state $|\Omega' = 1, v' = 29, J' = 1\rangle$ which we will use for the ground state transfer.

4.1 One-photon spectroscopy

First, we will study one-photon spectroscopy of the molecules, i.e. the 1557 nm pump transition from the Feshbach state to an electronic excited state. Molecular loss spectroscopy is carried out by illuminating the Feshbach molecules with a 750 µs pulse of pump light, polarized parallel to the magnetic field. If the pump light is resonant with a transition to an excited molecular state, the molecules populate the excited state and decay to other molecular levels which we cannot detect. This leads to a reduction in the number of molecules we detect in the trap. Starting with the maximum power of ~ 16 mW, the power in the pump beam is reduced until a small number of molecules is still observable even when directly on resonance in order to get an accurate measure of the transition centre. A number of these loss features may be seen in figure 4.1; each feature is recorded using a different power in the pump beam, ranging from 300 µW to 16 mW, due to the variation in coupling strengths between states. Each state is found with a constant bias field of 180.487(4) G applied to the molecules, to initialize them in the $|-2(1,3)d(0,3)\rangle$ state. To compare the wavelength of each transition with that previously reported [142], we must subtract the 327 MHz Zeeman shift of the atomic $|F=3, m_F=3\rangle$ state from the measured wavelength for each transition. This is because the measurements in [142] were made from a different Feshbach state at a different magnetic field of 217 G. The accuracy is limited entirely by the wavemeter (Bristol Instruments 621A). These values are presented in table 4.1.

We have not done an exhaustive search of all the transitions within the range of our lasers, as they have been extensively documented by Debatin *et al.* [142]. Instead, we focussed on the transitions that they showed to have good coupling to both the excited and ground states.

The transitions in the $\Omega' = 1$ manifold (see section 2.3.1 for an explanation of the quantum numbers) are good candidates for the intermediate STIRAP states as they have strong coupling to the Feshbach states, as seen in figure 4.5, and a long natural lifetime. They have another advantage: large hyperfine splittings, often much larger than the natural linewidth, so a single hyperfine state can be addressed, making a very pure three-level λ-type system. We show this in figure 4.2, where we vary the pump detuning across the $|-2(1,3)d(0,3)\rangle \rightarrow |v'=29, J'=2\rangle$

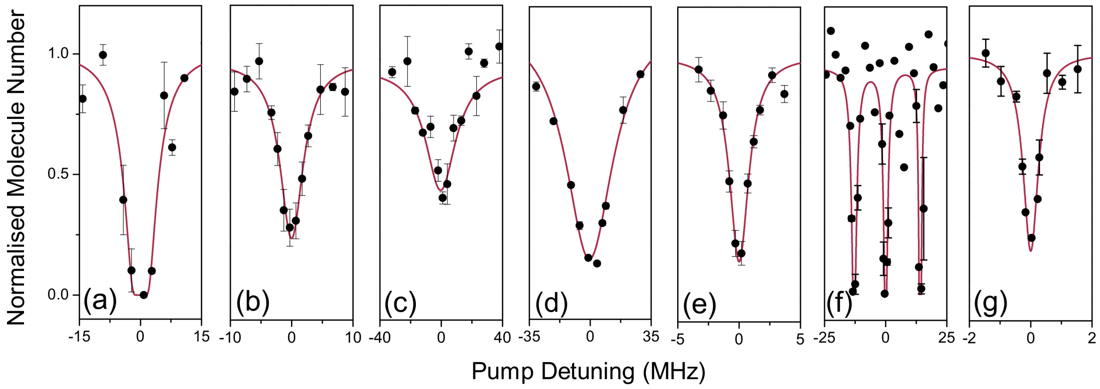

Figure 4.1: One photon molecular spectroscopy from the $|{-2}(1,3)d(0,3)\rangle$ state close to dissociation. We see loss of molecules when the pump laser is on resonance with transitions to molecular states in the $A^1\Sigma^+ + b^3\Pi$ hyperfine manifold. The pump detuning in each case is relative to the centre of the transition. The states (a)-(g) are labelled as in table 4.1.

	State	Transition Energy E/hc (cm^{-1})	
		Innsbruck	**Durham**
(a)	$\lvert\Omega' = 0, v' = 35, J' = 1\rangle$	6364.031(2)	6364.0301(7)
(b)	$\lvert\Omega' = 0, v' = 37, J' = 1\rangle$	6398.663(2)	6398.6584(7)
(c)	$\lvert\Omega' = 0, v' = 38, J' = 1\rangle$	6422.986(2)	6422.9730(7)
(d)	$\lvert\Omega' = 0, v' = 38, J' = 3\rangle$	–	6423.1149(7)
(e)	$\lvert\Omega' = 1, v' = 29, J' = 1\rangle$	6423.501(2)	6423.5026(7)
(f)	$\lvert\Omega' = 1, v' = 29, J' = 2\rangle$	–	6423.5843(7)
(g)	$\lvert\Omega' = 1, v' = 29, J' = 3\rangle$	–	6423.6847(7)

Table 4.1: A summary identifying the seven excited states studied, and the transition energies (E/hc) of each, as identified by the Innsbruck group [142] and by us. Note that we can excite the $|\Omega' = 0, v' = 35, J' = 1\rangle$ state transition with the pump laser, but it lies at the edge of the region accessible to the Stokes laser and so while 2-photon spectroscopy is just possible (see chapter 6), the Rabi frequencies are not high enough to perform STIRAP transfer.

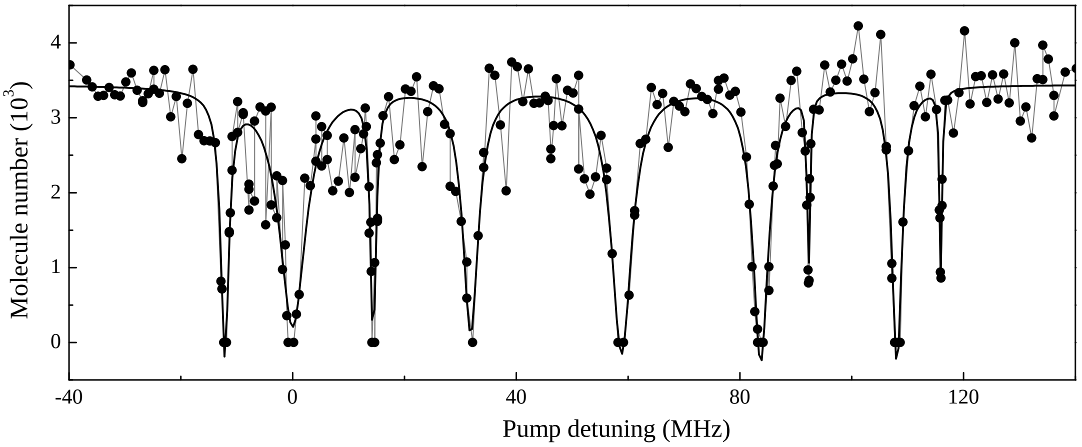

Figure 4.2: Hyperfine structure in the $|v' = 29, J' = 2\rangle$ excited state of the $A^1\Sigma^+ + b^3\Pi$ manifold. The lowest three peaks are the transitions in figure 4.1. The hyperfine quantum numbers of these states have not been identified, but show well-separated hyperfine states and rich structure even within a single rovibrational level.

excited-state transition with a 20 ms pulse of 16 mW of pump light, showing a large number of loss features corresponding to hyperfine and Zeeman states. We have not identified the hyperfine quantum numbers of these transitions, but we see that the states are well-separated and very numerous. These states can have very different coupling strengths, offering another degree of freedom and a wider selection of states when searching for a suitable intermediate STIRAP state.

For STIRAP, we use the lowest hyperfine level of the $|\Omega' = 1, v' = 29, J' = 1\rangle$ state. A broad scan of this rovibrational state is shown in figure 4.3. We see that the hyperfine states are well-separated: the nearest state is 300 MHz higher. We identify the exact centre of the lowest resonance by setting the pump power to 36 µW and pulsing it on for 750 µs. We vary the pump detuning and, as before, monitor the molecule loss. A Lorentzian fit, as shown in figure 4.4, gives the centre. Over about two hours, we can locate the transition to within 5 kHz, much less than the natural linewidth we measure later in section 5.4.

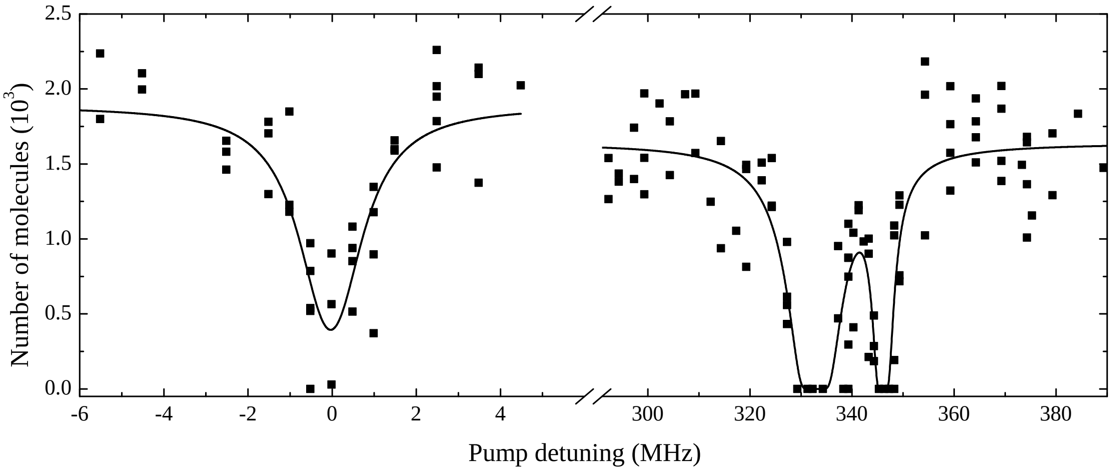

Figure 4.3: Hyperfine structure in the $|v' = 29, J' = 1\rangle$ excited state of the $A^1\Sigma^+ + b^3\Pi$ manifold. The lowest transition is the intermediate state we use for STIRAP. Note the powers for the two curves are very different: 14 µW for the lower transition, and 15 mW for the upper two. Solid lines are to guide the eye.

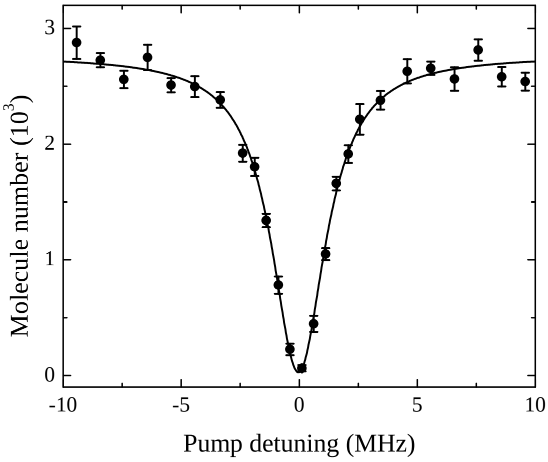

Figure 4.4: High-precision scan of the lowest hyperfine state in the $|v' = 29, J' = 1\rangle$ rovibrational level. This is the intermediate state we use for STIRAP transfer to the absolute ground state. Such a measurement takes a few hours and locates the transition centre to within ±5 kHz

4.2 Rabi frequencies

We will now look at the Rabi frequencies and coupling strengths for the transitions we will use for STIRAP. As discussed in section 1.5.2, the initial state from which we begin our ground state transfer is not limited to the $|-2(1,3)d(0,3)\rangle$ state. In fact, in this section we will see that the $|\Omega' = 1, v' = 29, J' = 1\rangle$ state we use has much stronger coupling to the $|-6(2,4)d(2,4)\rangle$ state. We measure the strength of the coupling by setting the pump laser on resonance, varying the duration of the pump pulse used (t), and measuring the fraction of the molecules remaining in the initial state (N/N_0). We see this loss for the $|-2(1,3)d(0,3)\rangle$ and $|-6(2,4)d(2,4)\rangle$ Feshbach states in figure 4.5. The molecule number is then fitted with

$$\frac{N}{N_0} = \exp\left(\frac{-\Omega_{\mathrm{p}}^2 t}{\gamma}\right), \tag{4.1}$$

where Ω_{p} is the Rabi frequency and γ is the $2\pi \times 35$ kHz natural linewidth of the pump transition (see section 5.4).

Figure 4.5 shows the variation in the reduced Rabi frequency (normalised to the peak pump power) as the magnetic field changes. We see a clear peak when the molecules start in the $|-6(2,4)d(2,4)\rangle$ state. As the Rabi frequency for the transition from the $|-6(2,4)d(2,4)\rangle$ state is more than 60 times that achieved for the $|-2(1,3)d(0,3)\rangle$ state transition, we use $|F\rangle \equiv |-6(2,4)d(2,4)\rangle$ for two-photon experiments. In section 1.5.2 we saw that the Feshbach molecules have a reduced lifetime of 23 ms in this state. However, the pulse sequence for one- and two-photon spectroscopy (see section 4.3 below) takes less than 1 ms, so this lifetime reduction is negligible.

4.3 Dark-state spectroscopy

To detect low lying molecular levels of the singlet potential we use two-photon dark-state spectroscopy [150, 151]. This is done by keeping the pump laser on resonance with the $|F\rangle \to |E\rangle$ transition, and pulsing both the pump and Stokes lasers on simultaneously for 750 μs. The Stokes power is set to the maximum available of 16 mW, while the power of the pump laser is set to 40 μW such that

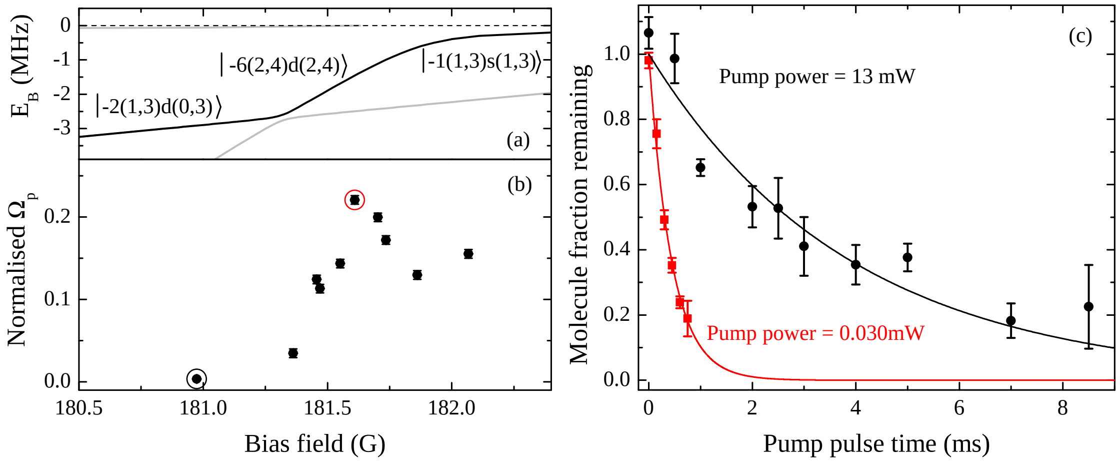

Figure 4.5: Varying Rabi frequency with different initial Feshbach states, for the transition to the lowest hyperfine state of the $|v' = 29, J' = 1\rangle$ rovibrational level. (a) molecular states near the dissociation threshold. (b) Rabi frequency normalised to $\sqrt{I}$ with I the peak intensity of the pump beam. We see a peak around 181.6 G when we start in the $|{-6}(2,4)d(2,4)\rangle$ state. (c): loss of the Feshbach molecules when driving the pump transition from the $|{-6}(2,4)d(2,4)\rangle$ (red) and $|{-2}(1,3)d(0,3)\rangle$ (black) states. These correspond to the marked points in (b). Note the former is considerably faster despite using 400× less pump power.

the pump transition is slightly saturated. When the Stokes light is off resonance, we therefore observe no molecules after the pulse. If the Stokes light is on resonance with a transition $|E\rangle \rightarrow |G\rangle$ however, the molecules are projected onto the dark state given by equation 3.1. Imaging the dissociated atoms after the pulse sequence corresponds to a projection of this dark state back onto the initial Feshbach state. This double projection results in a final state given by $\cos^2(\theta)\,|F\rangle + \sin^2(\theta)\,|G\rangle$, with $\tan\theta = \Omega_P/\Omega_S$. During the pulse, the Stokes Rabi frequency is much higher than the pump Rabi frequency and hence the mixing angle θ is small. This leads to a large proportion of the Feshbach state remaining following the pulse sequence, which we observe as a suppression of the molecular loss. This method lets us search for the rovibrational ground state before attempting STIRAP. The result of scanning the Stokes frequency across the transition to the ground state is shown in figure 4.6.

We measure absolute frequencies of 192572.09(2) GHz and 306830.49(2) GHz for the pump and Stokes transitions respectively. This implies a zero-field binding energy of $hc \times 3811.576(1)$ cm^{-1} for the $J'' = 0$ state, relative to the degeneracy-weighted hyperfine centres. This is consistent with the latest theoretical values [152] and experimental measurements [142], and the measurement is limited by the accuracy of our wavemeter. In chapter 6 we measure the binding to ±40 kHz precision using an optical frequency comb.

We have seen the dark state resonance from the $|-2(1,3)d(0,3)\rangle$ initial state, despite the lower coupling strength to the excited state. This is possible because for two-photon spectroscopy the pump Rabi frequency must be much lower than the Stokes Rabi frequency, to ensure that the mixing angle θ is small. However STIRAP transfer to the ground state is extremely inefficient from this initial state with our available laser intensities, and all the two-photon measurements presented in this thesis use the $|-6(2,4)d(2,4)\rangle$ initial state.

We observe both the $J'' = 0$ and $J'' = 2$ levels of the electronic and vibrational ground state in figure 4.6, separated by $h \times 2940.77(7)$ MHz. To the best of our knowledge this is the most precise direct measurement of this splitting. Note that our publication [80] gives incorrect values for this splitting and B_0, caused by an arithmetical error. This mistake is corrected here. In the rigid rotor approximation

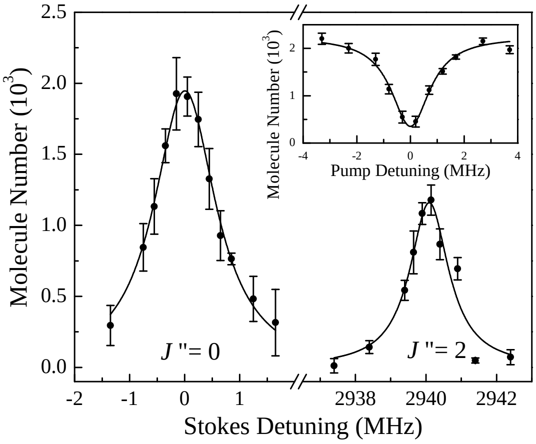

Figure 4.6: Two-photon spectroscopy of the RbCs vibrational ground state. The molecules remain in the initial near-dissociation state when the Stokes light is on resonance with the $J'' = 0$ and $J'' = 2$ rotational states. The solid lines illustrate Lorentzian fits used to determine the resonance positions. Inset: One-photon loss spectrum for the $|a^1\Sigma^+ + b^3\Pi_1, v' = 29, J' = 1\rangle$ state. The pump laser is held on resonance with this transition during the two-photon spectroscopy.

(neglecting centrifugal distortion), the rotational levels have energies of

$$E(J) = B_0 J''(J''+1). \tag{4.2}$$

This implies a rotational constant $B_0 = 0.0163489(4)\ \mathrm{cm}^{-1}$, which is consistent with the theoretical prediction of $0.0163(4)\ \mathrm{cm}^{-1}$ [152].

We do not include centrifugal distortion in this calculation. However, in section 2.3.2 we estimated the centrifugal distortion constant as $D = 200$ Hz. The shift of the $J'' = 2$ rotational level is $DJ''^2(J''+1)^2 \sim 8$ kHz. This is much smaller than the 70 kHz uncertainty on our rotational spacing and thus we do not need to include it, though the 5 kHz precision of our binding energy measurement in chapter 6 suggests we might be able to resolve it with further measurements.

The accuracy of this measurement of B_0 is limited, because we cannot resolve the hyperfine structure of the molecule using dark-state spectroscopy. In the $J'' = 0$ ground state, the hyperfine state we address is known, as seen in figure 6.5, and we could account for it. However we have not studied the $J'' = 2$ hyperfine structure in detail and could be addressing any of several hyperfine states. We could improve

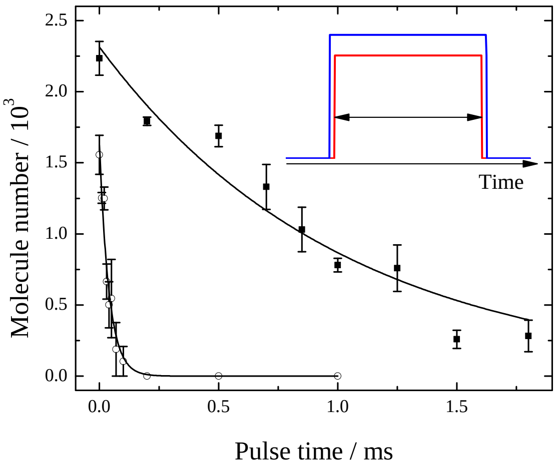

Figure 4.7: Decoherence of the dark-state resonance using the $|a^1\Sigma^+ + b^3\Pi_1, v' = 29, J' = 1\rangle$ intermediate state. Black squares show the loss of molecules with the Stokes laser on resonance with the rovibrational ground state. Open circles are with the pump laser only, for comparison. The curves are exponential decay fits, with $\tau = 1.0(1)$ ms with the Stokes and $\tau = 40(5)$ µs without. There is a large range of times from 0.2 ms → 1.25 ms where molecules only remain when the Stokes is on, which shows that this intermediate state is suitable for two-photon spectroscopy. Inset: pulse sequence sketch (not to scale). Pump and Stokes are red and blue respectively.

the measurement by using STIRAP to determine the $J'' = 2$ hyperfine structure, as we have done for $J'' = 0$ in figure 6.5, but this would be a significant amount of work.

Driving direct microwave transitions between the rotational levels would give a high-precision measurement of the spacings, and we are currently pursuing this idea in the experiment. Selection rules would let us drive the transitions $J'' = 0 \rightarrow J'' = 1$ and $J'' = 2 \rightarrow J'' = 1, 3$, so this would let us measure the energies of the $J'' = 0, 1, 2, 3$ levels and fit equation 2.19 to measure D and H. This could be combined with a measurement of the vibrational splitting and equation 2.20 to test the harmonicity of the ^{87}RbCs molecular potential.

We characterise the "quality" of the two-photon resonance by looking at the decoherence rate. Both lasers are set on resonance and we pulse 200 µW of pump light and 16 mW of Stokes light for a variable time. The molecules are projected on to the dark state as in the dark-state spectroscopy, but the dark state decoheres and the molecules are lost through excitation to the excited state. In figure 4.7 we compare the decay rates with and without the Stokes light, and see that the decay rate is reduced by a factor of 25, indicating a strong suppression of molecule loss. There is a wide range of pulse times where molecules remain only when the Stokes laser is on. We use pulse times in this range when measuring transition frequencies, as they give a molecule number of zero when the Stokes laser is off resonance and thus a better signal-to-noise ratio.

4.4 Electric dipole moment

We will now look at the electric dipole moment of the molecule, and the effect of electric fields on the spectroscopy. The permanent electric dipole moment (EDM) of a polar molecule is the key quantity of interest for many applications. Without an externally applied electric field, the averaged electric dipole moment in the laboratory frame is zero. Turning on an electric field couples states of opposite parity and hence polarizes the molecules in the direction of the field. In the experiment, we apply the necessary electric field with an array of four electrodes positioned outside the fused silica cell (shown in figure 4.8). We first measure the DC Stark shift of the pump transition as a function of the applied electric field. We can then measure the relative shift between the $|E\rangle$ and $|G\rangle$ states (the Stokes shift). As the electric dipole moment of the state $|F\rangle$ is negligible due to the large interatomic separation, the difference between the pump and Stokes shifts yields the DC Stark shift of the rovibrational ground state (shown in figure 4.11).

4.4.1 Electric field creation and calculation

The electric field is generated by a set of four electrodes running parallel to the outside of the fused silica cell. The electrodes are 1.5 mm in diameter, separated by 29.0(2) mm vertically, 24.8(2) mm horizontally and are 22.0(5) mm long. They are bent at either end at a radius of 2(1) mm to allow electrical connections to be made without interfering with the already limited optical access to the cell. The

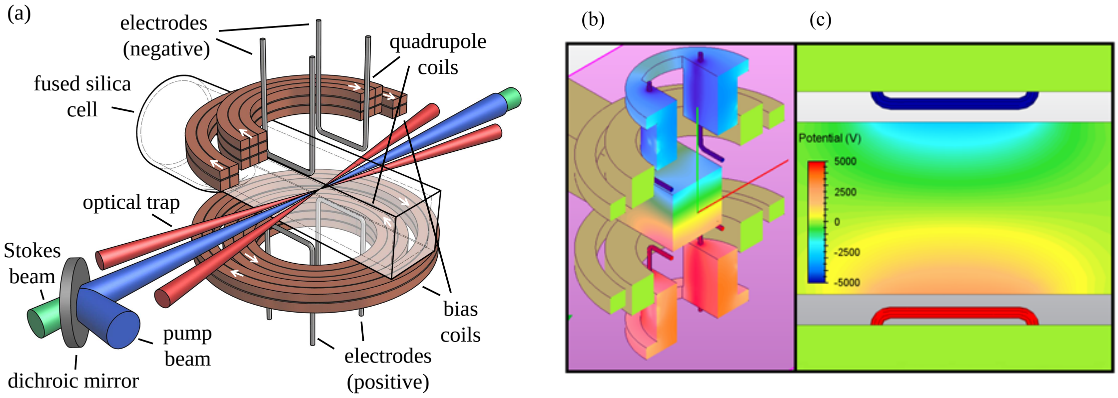

Figure 4.8: Electric field generation and calculation. (a) The position of the high-voltage electrodes outside the vacuum cell, with the magnetic field and gradient coils and position of the optical trap shown. The coil and electrode mounts are not shown, but are included in the field simulation. (b) Cutaway view of the model of the setup, showing the simulated electric potential. (c) Cross-section of the potential in the vertical plane along the vacuum cell.

electrodes are currently connected in pairs so that the two electrodes above the cell are negatively charged, and the two below the cell are positively charged. We do not currently have any experimental method of calibrating our electric field. We therefore calculate the electric field at the centre of the cell by using finite element analysis to solve the Poisson equation. A 3D mesh is generated from a CAD model of the experimental apparatus which includes the electrodes, cell walls, earthed magnetic field coils, and dielectric coil mounts. The mesh creation and subsequent calculation is carried out in the Autodesk Multiphysics software package. The 3D model and results of the finite element analysis are shown in figure 4.8. It is found that the presence of the fused silica cell (external dimensions of 24 mm × 24 mm × 80 mm, with 2 mm thick walls) enhances the electric field by $\sim 2\,\%$. The electric field at the centre of the cell given an applied electric potential of 1 kV between the upper and lower electrode pairs is 153(1) Vcm^{-1}. The gradient of the electric field at the centre of the cell is zero, so the uniformity is determined by the curvature of the field as defined by its second order derivative equal to 17(5) $\mathrm{V\ cm}^{-3}$. Hence a displacement of the molecular cloud from the centre of the cell by 1 mm leads to a variation in the electric field seen by the

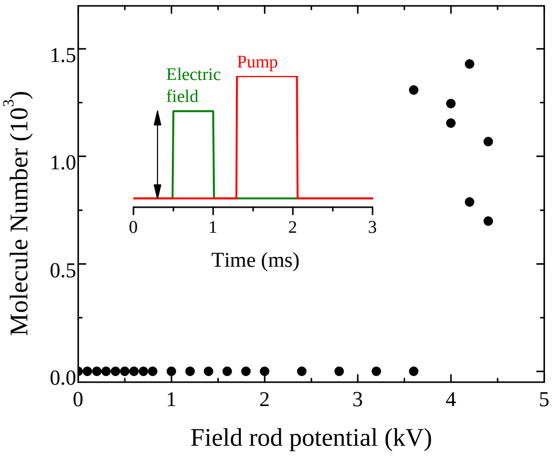

Figure 4.9: Maximum usable field for a short pulse. The electric field is pulsed on, followed by resonant pump light to remove all the molecules. When the cell polarises significantly, the pump transition shifts off resonance and the the molecules are not removed. We see a maximum usable potential of ±3.5 kV or ∼ 1 kV/cm.

molecules of less than 0.1 %. The uncertainties in the calculated electric field are discussed in section 4.4.4.

The high voltage power supplies connected to the electrodes are TTL controlled so that the field is only applied for the portion of the experiment when the STIRAP pulses are in operation. The field we can use in our measurement of the ground-state dipole moment is limited by electric polarisation or charge buildup on the glass vacuum cell. When an electric field is applied, this polarisation opposes it, reducing the field at the molecules. Thus it is important for the accurate calculation of the electric field that we avoid electric polarization of our cell. In section 5.10 we will see that, if the field is turned on at ±240 V s^{-1} with the cell unpolarised, the polarisation effect causes the electric field to reduce by 1.4 V $cm^{-1}s^{-1}$. However as a test for the measurement of the EDM, where the exact field is critical, we measure the residual polarisation caused by short, high electric field pulses up to ±4500 V. We set the pump laser on resonance and the electric field is pulsed on for 0.5 ms. 0.35 ms later, a 0.75 ms pulse of pump light removes all the molecules. We increase the field until the molecules reappear, as shown in figure 4.9, indicating that the residual electric polarisation has shifted the pump transition off resonance. This shows we can apply up to ±3.5 kV or ∼ 1 kV/cm to the molecules. Remnant polarization can remain in the experiment for days following a high voltage pulse. To remove this polarization between measurements, we bathe the cell in UV light. The UV light is generated by a single LED (Roithner-Lasertechnik LED395-66-60-110), and has a typical output power of 240 mW at 395 nm. The mechanism which causes this is not clear, but testing has revealed no measurable shift in the molecular transitions after the vacuum chamber and surrounding area have been irradiated for a few minutes.

4.4.2 Excited state Stark shift

We characterize the $|\Omega' = 1, v' = 29, J' = 1\rangle$ state by measuring its DC Stark shift. By applying a 750 µs pulse of pump light whilst an electric field is applied to the molecules we can track the DC Stark shift of the various hyperfine sublevels of the state from their zero field values as shown in figure 4.10. The DC Stark shift of the state is initially linear with a gradient of 500 kHz/(Vcm^{-1}) up to $\sim$ 400 Vcm^{-1}. Above this field, we observe an avoided crossing between the sublevel identified for STIRAP and the higher-lying hyperfine states. It is worthy of note that the coupling to these higher-lying states is relatively weak as $\sim$ 15.6 mW of available pump power is required to saturate the transitions, whereas only 69 µW is necessary to saturate the lowest hyperfine sublevel which we use for STIRAP (see the left frame of figure 4.10). Because of this, we do not follow the avoided crossing for the two-photon spectroscopy, which would allow only very low Rabi frequencies at high fields, but cross it as shown in the right frame of figure 4.10 to maintain the strong coupling.

4.4.3 Ground state shift

We measure the ground state Stark shift by the difference in shift between the pump and Stokes transitions. At each electric field, we find the pump transition as in figure 4.10 and do a high-precision scan to locate it precisely. We then measure the Stokes transition frequency as in figure 4.6. Subtracting the pump shift from the Stokes gives the absolute shift of the ground state, shown in figure 4.11.

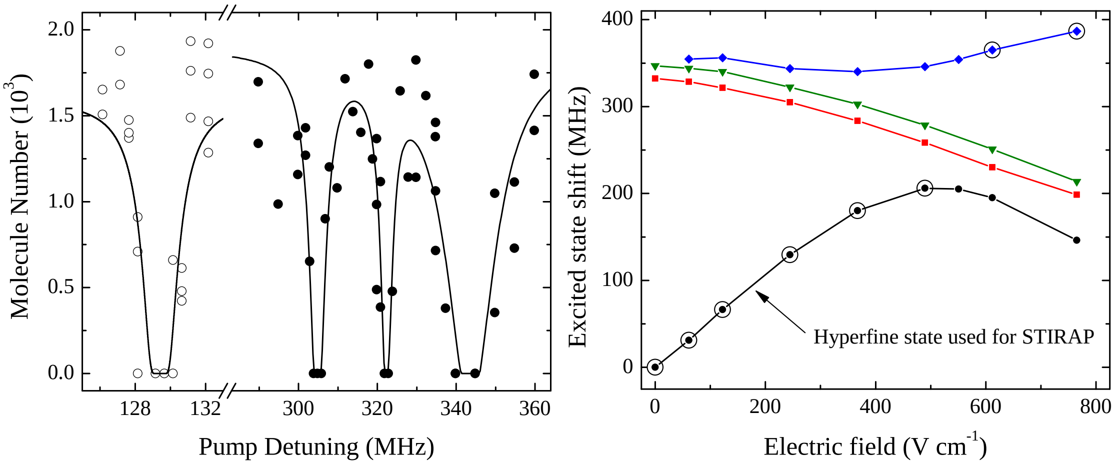

Figure 4.10: One photon Stark spectroscopy from the $|-6(2,4)d(2,4)\rangle$ state close to dissociation. (a) Spectroscopy of the four hyperfine sublevels of the $|\Omega' = 1, v' = 29, J' = 1\rangle$ state observed with an applied electric field of 245 V/cm. Empty circles show data collected with a pump power of 69 µW, filled circles show a pump power of $\sim$ 15.6 mW. (b) Stark shift of these states up to an applied electric field of 765 V/cm. The lowest hyperfine sublevel is used for STIRAP transfer to the rovibrational ground state. An avoided crossing is observed between that state and the higher-lying hyperfine states at an applied electric field of $\sim$ 550 V/cm. Circles show the state used for the ground-state spectroscopy in figure 4.11.

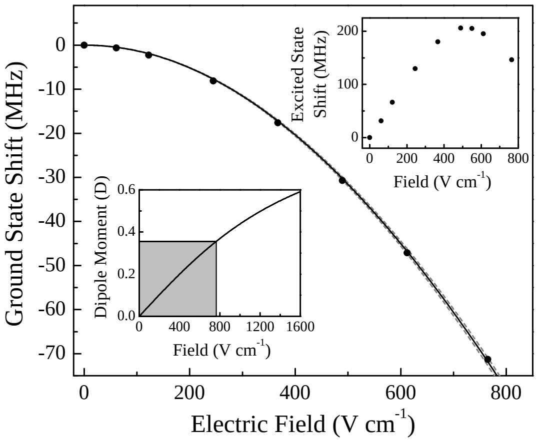

Figure 4.11: Stark shift of the rovibrational ground state. The solid black line shows the curve fitted to our results from which we extract a permanent electric dipole moment in the molecular frame of 1.225(3)(8) D. The dotted grey lines indicate the upper and lower bounds due to the systematic error in the electric field calculation. Upper inset: Stark shift of the $|^3\Pi_1, v' = 29, J' = 1\rangle$ excited state used for Stark spectroscopy and STIRAP. The behaviour is initially linear with a gradient of approximately 500 kHz/(Vcm^{-1}) up to a field of $\sim$ 400 Vcm^{-1}. Lower inset: Ground-state electric dipole moment in the laboratory frame as a function of electric field. The grey region indicates the range of electric dipole moments currently accessible in the experiment.

We fit the Stark shift by calculating the matrix solution of the rigid-rotor Stark Hamiltonian in the laboratory frame [78, 153]. These matrix elements are defined by

$$\begin{aligned}\langle J\ m_J \mid H \mid J'\ m_J' \rangle = {} & B_0 \cdot J(J+1) \cdot \delta_{JJ'm_Jm_J'} \\ & - d_0 E \sqrt{(2J+1)(2J'+1)} \cdot (-1)^{m_J} \cdot \\ & \begin{pmatrix} J & 1 & J' \\ -m_J & 0 & m_J' \end{pmatrix} \begin{pmatrix} J & 1 & J' \\ 0 & 0 & 0 \end{pmatrix}, \end{aligned} \tag{4.3}$$

where J and m_J are the rotational quantum number and its projection along the z axis respectively, B_0 is our experimentally measured rotational constant, E is the applied electric field, and the two matrices are Wigner 3-j coefficients. We include rotational levels up to $J = 8$. This equation can be understood by considering its two terms separately. The first is the rotational splitting without the presence of an applied field, the second is the DC-Stark shift. Intuitively, as the field increases the degeneracy of the rotational m_J states is removed and the molecule axis gradually aligns along the applied field, giving an increasing dipole moment in the laboratory frame.

4.4.4 Error budget for measurement of the electric dipole moment

The major sources of systematic error in the calculated value of the permanent electric dipole moment can be seen in Table 4.2. They are broken down into three areas. The first is due to the uncertainty in the measurement of the electrode separations, including any uncertainties in the electrode shape (i.e. the bend radius at either end of each electrode). The next is the uncertainty in the position of the molecular cloud with respect to the centre of the electrode array, estimated to be ±1 mm in any direction. Note that the position of the glass cell with respect to the electrode array has an error of similar magnitude. However, calculations of the electric field where we move the glass cell by 4±1 mm show negligible deviation from the central value. The final source of error is from the electric field calculation itself. Finite element analysis is an approximate method which relies upon a converging solution. This convergence has some noise, which is estimated

	α_{d_0} (D)
Electrode separation	±0.007
Molecule position	±0.002
Field calculation	±0.004
Total systematic error	±0.008

Table 4.2: Breakdown of the various sources of systematic uncertainty in the measured value of the permanent electric dipole moment (α_{d_0}).

by repeating the calculation with various mesh densities. We estimate the uncertainty in this value to be ±0.7 % of the central electric field at a given potential. It is clear that the uncertainty is dominated by the accuracy of the measurement of the electrode position.

We have measured the Stark shift of the excited state at 245 Vcm^{-1} with the electric field applied in the reverse direction. We measured a 50 kHz disparity between forward and reverse field Stark shift measurements, against an overall Stark shift for the transition of 130 MHz. This is consistent with our estimate of the uncertainty associated with the position of the molecules with respect to the centre of the electrode array.

Including all these considerations, we get a final value for the permanent dipole moment of the ^{87}RbCs molecule:

$$d_0 = 1.225(3)(8)\ \mathrm{D}$$

where the values in brackets are the statistical and systematic uncertainties respectively.

The lower inset in figure 4.11 shows the fitted DC Stark shift converted into the equivalent electric dipole moment in the laboratory frame, and the grey region indicates the dipole moment range currently accessible in the experiment.

The maximum laboratory-frame dipole moment we access in this measurement is 0.355(2)(4) D at an electric field of 765 Vcm^{-1}. We believe this was, at the time of publication of [80], the largest dipole moment accessible in the laboratory frame in any ultracold molecule experiment. For comparison, in ^{87}RbCs, Takekoshi *et al.*

accessed laboratory-frame dipole moments of ~ 0.03 D [79], while in KRb, Ni *et al.* reported values up to 0.22 D [28]. Park *et al.* have since reported 0.8 D in ^{23}Na^{40}K [81], and Guo *et al.* have recently achieved 1.06(4) D in ^{23}Na^{40}Rb [82].

Takekoshi *et al.* have reported a measured value of $d_0 = 1.17(2)(4)$ D [79], which agrees with our measurement within our respective uncertainties. A key feature of our work is that we can apply a larger electric field. This allows measurement of the ground-state dipole moment with smaller uncertainties and the realization of larger laboratory-frame electric dipole moments than in [79].

4.5 Conclusions

In this chapter, we have studied the ^{87}RbCs molecule with one- and two-photon spectroscopy. We have identified a suitable intermediate transition for STIRAP transfer to the ground state. With two-photon spectroscopy, we have measured the rotational constant and electric dipole moment of the ^{87}RbCs ground state. This puts us in an excellent position to transfer the molecules to the ground state, which we will cover in chapter 5.

Chapter 5

Creation of ground-state ^{87}RbCs molecules

In this chapter, we will describe the transfer of our Feshbach molecules to the ground state using STIRAP. We build a model of the transfer including the effects of finite laser linewidth, based on [94], and show that we have excellent agreement with experimental measurements of the STIRAP transfer and the independent measurements of the laser linewidth and shot-to-shot noise made in chapter 3. We also completely characterise the transitions used in the transfer with direct measurements of the Rabi frequencies, and we estimate the excited-state lifetime. This gives a simple, well understood route for the creation of ground-state ^{87}RbCs molecules and a valuable diagnostic for optimising the laser system. With these methods, we achieve a one-way transfer efficiency of 88(3)% to the rovibrational and hyperfine ground state. The ground-state molecule sample has a lifetime of 0.89(6) s.

5.1 Ground-state transfer in an optical potential

Transfer to the ground state via STIRAP relies on a dark state $|\psi\rangle$ that is an eigenstate of the Hamiltonian of a λ-type system, equation 5.9, on two-photon

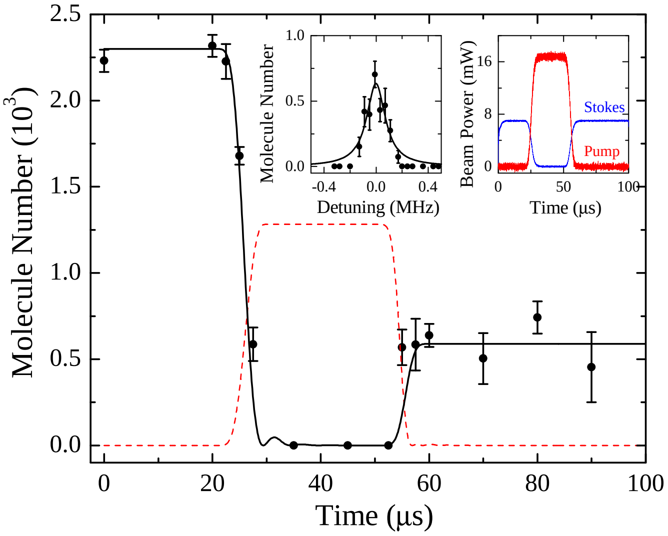

Figure 5.1: Transfer of ~ 1250 optically trapped molecules to the absolute ground state. Shown is the number of molecules remaining in the Feshbach state $|F\rangle$ when both lasers are switched off during the STIRAP sequence. The black solid and red dashed lines show the Feshbach and ground-state populations. They are taken from the Lindblad model described in the text, but are to guide the eye only. The 50% transfer efficiency each way is limited by AC Stark shifts from the optical trapping beam. Left inset: The final population of Feshbach molecules as a function of Stokes detuning. Right inset: The pump and Stokes beam powers during the STIRAP pulse sequence.

resonance. This is composed of a superposition of the $|F\rangle$ and $|G\rangle$ states,

$$|\psi\rangle = \cos\theta\,|F\rangle + \sin\theta\,|G\rangle\,, \tag{5.1}$$

where the mixing angle θ is defined by $\tan\theta = \Omega_\mathrm{P}/\Omega_\mathrm{S}$. Transfer from state $|F\rangle$ to $|G\rangle$ (and back) is then achieved by an adiabatic change in the mixing angle, using the pulse sequence shown in the right inset of figure 5.1. The Stokes beam is initially turned on to 7 mW for 20 µs. With $\Omega_\mathrm{S} \neq 0$ and $\Omega_\mathrm{P} = 0$, $|\psi\rangle$ is equivalent to the initial state $|F\rangle$. The Stokes beam is then ramped down in 10 µs while the pump beam is ramped up to 16 mW. This adiabatically transfers the population to the ground state $|G\rangle$. We cannot detect the ground state directly, so after a 20 µs hold we reverse the process to transfer back to the initial state, allowing measurement of the square of the one-way efficiency. The maximum efficiency is achieved with both lasers on resonance, as shown in the left inset to figure 5.1. We map out the transfer by truncating the pulse sequence and recording the molecules remaining in the state $|F\rangle$, as shown in figure 5.1 for the on-resonance case.

The model of the transfer process in figure 5.1 is based on a numerical integration of the Lindblad master equation, but is to guide the eye only. This is for two reasons. First, for this transfer we did not have a direct measure of the Stokes Rabi frequency, so this was left as a free parameter. Second, the transfer efficiency is limited by the AC Stark shift of the transitions caused by the trapping laser, which is not included in the model. The line should therefore be taken only as a guide to the eye, and the one-way transfer efficiency of 50% and ground-state population of ~ 1250 molecules are calculated directly from the experimental data.

We will see in section 6.3 that we can address the $m_f = 4$ and $m_f = 5$ hyperfine states with vertical and horizontal Stokes polarisations respectively. In figure 5.1 we use the horizontal case. The left inset shows a single peak when scanning the Stokes frequency, indicating that we have addressed only the lowest, $m_f = 5$, hyperfine state.

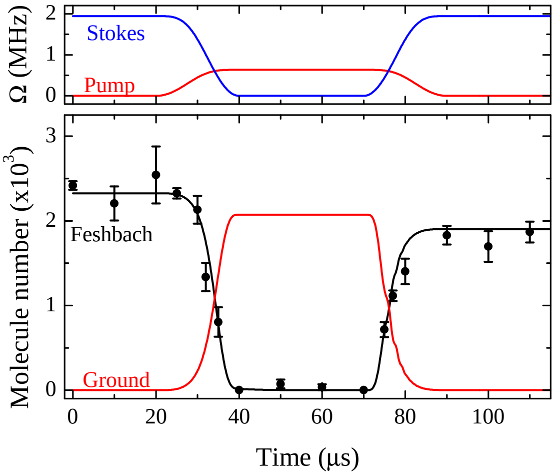

Figure 5.2: Transfer of molecules to the absolute ground state and back using STIRAP. Top: analytic approximations of the Rabi frequency profiles for the transfer. The maximum values for both the pump and Stokes are both measured (see section 5.3). Bottom: Population remaining in the initial (Feshbach) state. Circles are experimental data, and show a one-way efficiency of 88(3)%. The black and red lines are a simulation which includes the laser linewidth and has no free parameters, as described in the text. Note that most of the outward transfer occurs in the last 10 μs of the ramp because of the high Stokes Rabi frequency.

5.2 Optimised ground-state transfer

In our previous work we achieved 50% transfer efficiency [80], but we have since found this to be limited by a variable AC Stark shift of the 1557 nm pump transition across the sample. This was caused by the 1550 nm trapping beams, which reduced the coherence of the pump transition. In this section we remedy this by switching off the trapping beams for 120 μs during the transfer sequence to remove this effect. The magnetic gradient coil is turned off earlier in the sequence, so during the transfer the molecules are in free flight in a uniform magnetic field of $\sim$ 181.6 G with a curvature of 0.3 G/cm^2. The optical trap is switched back on after the transfer sequence to recapture the remaining Feshbach molecules. The axial trapping frequency is 180 Hz, which corresponds to a period of 5.5 ms. The molecules do not move significantly while the trap is off for 120 μs, so there is no measureable drop in the number or increase in the temperature. Using this method we observe a one-way transfer efficiency of 88(3)% and create a sample of 2000 ground-state molecules, as seen in figure 5.2.

5.3 Characterising the molecular transitions

The transfer efficiency in equation 2.13 depends on the Rabi frequencies Ω_P and Ω_S and the excited-state linewidth Γ. If we wish to model the STIRAP transfer, we must first make reliable measurements of all these parameters.

We measure the transition strengths by driving and directly observing Rabi oscillations on each transition. For an open 2-level system where the excited state decays to other levels at a rate Γ, the probability $P_F(t)$ of finding the system in the lower state oscillates and decays [154] as

$$P_F(t) = \cos^2\left(\frac{\Omega t}{2}\right) e^{-\Gamma t/2}. \tag{5.2}$$

We assume here that the “closed” decay rate from the upper to the lower state is negligible. We note the factor of 1/2 in the decay term, which arises because the oscillations mean the system spends only half the time in the excited state. To measure the pump transition, we pulse on 12.4 mW of resonant pump light for

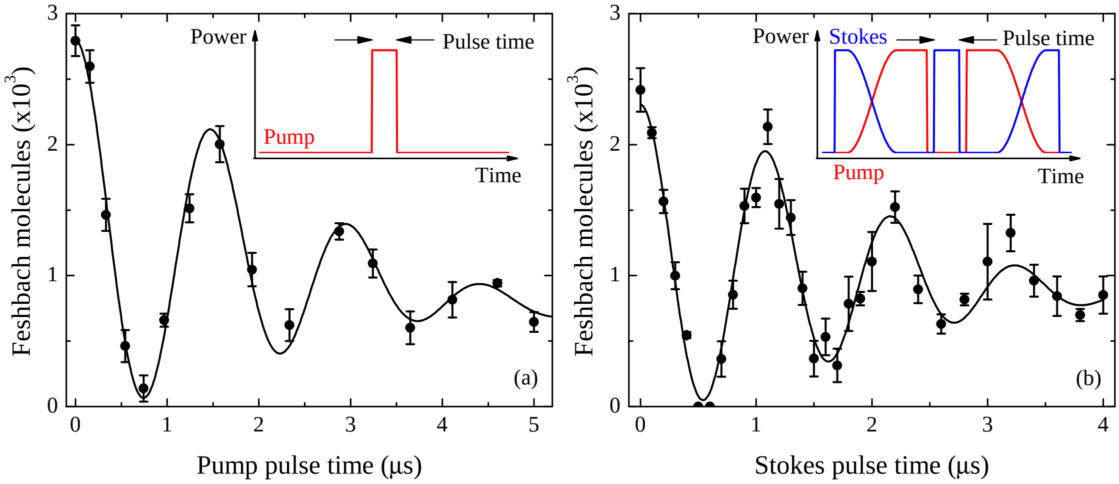

Figure 5.3: Rabi oscillations on (a) the pump and (b) the Stokes transitions. A fit to each is shown, which includes decay of the excited state and dephasing from spatial variation of the Rabi frequency. Inset are sketches of the pulse sequences for each measurement, with the pump laser in red and the Stokes in blue. For the Stokes, we transfer the molecules to the ground state by STIRAP before driving the oscillations, and then transfer any remaining ground state population back to the Feshbach state for detection.

a variable time of a few microseconds and monitor the population in the initial $|{-6}(2,4)d(2,4)\rangle$ state. We see Rabi oscillations driven on the pump transition, as shown in figure 5.3(a).

To observe the Stokes Rabi frequency, the molecules are first transferred to the ground state by STIRAP. The Stokes beam is then switched on to 3.4 mW for a few microseconds, with the pump beam off, before the molecules are transferred back to the Feshbach state by STIRAP. Rabi oscillations on the Stokes transition are shown in figure 5.3(b).

The simple model of the Rabi oscillations in equation 5.2 can estimate the Rabi frequency, but gives a poor fit for longer pulse durations. This is because the oscillations begin to dephase at later times due to variation in Rabi frequency across the cloud. Daniel *et al.* [155] build an analytic theoretical model including the thermal motion of the sample and Rabi frequencies varying over distances smaller than the imaging resolution. Here, the dissociation and detection scheme we use means that we can monitor only the total population and cannot resolve variations in the Rabi frequency across the cloud. Rough calculations show that the thermal effects are several orders of magnitude too small to be measured in our system, leaving only the dephasing term. This gives an oscillation of the form

$$N = \frac{N_0}{2} e^{-\Gamma t/2} \left(1 + \exp\left(-\frac{t^2}{T_x^2}\right) \cos(\Omega t)\right), \tag{5.3}$$

where

$$T_x = \frac{\sqrt{2}}{\sigma_I \cdot \partial_x \Omega} \tag{5.4}$$

is the dephasing time resulting from the spatial variation of the Rabi frequency, σ_I is the molecule sample size and $\partial_x \Omega$ is the Rabi frequency gradient across the sample. Fits to these equations are shown in figure 5.3 and give pump and Stokes Rabi frequencies of $2\pi \times 666(6)$ kHz and $2\pi \times 915(7)$ kHz respectively. The dephasing times are 3.2(3) µs and 2.5(2) µs respectively. With a transverse cloud size of ~ 10 µm at the centre of a 35 µm Gaussian beam, these are roughly consistent with the variation in Rabi frequency across the cloud according to equation 5.4.

We use our measured beam sizes and powers to calculate reduced Rabi frequencies of $2\pi \times 0.9(1)\ \mathrm{kHz}\sqrt{\mathrm{I_P}/(\mathrm{mW/cm^2})}$ for the pump transition and $2\pi \times 2.2(2)\ \mathrm{kHz}\sqrt{\mathrm{I_S}/(\mathrm{mW/cm^2})}$ for the Stokes. These values have been measured in Innsbruck [79] using the decay time at low Rabi frequency, when $\Omega \ll \Gamma$ and the Rabi oscillations are not visible. Our values agree well with measurements in Innsbruck, which give values of $2\pi \times 0.8(2)\ \mathrm{kHz}\sqrt{\mathrm{I_P}/(\mathrm{mW/cm^2})}$ and $2\pi \times 2.8(7)\ \mathrm{kHz}\sqrt{\mathrm{I_P}/(\mathrm{mW/cm^2})}$ respectively (see supplementary material for [79]).

From the Rabi frequencies and the intensities of our beams, we calculate dipole matrix elements for the pump and Stokes transitions. The dipole matrix element D is

$$D = \langle \psi_f | e\vec{r} | \psi_i \rangle \tag{5.5}$$

and we can calculate it by

$$\hbar\Omega = DE \tag{5.6}$$

where E is the electric field of the light [121]. The electric field is given by

$$I = \frac{c\epsilon_0}{2} E^2 \tag{5.7}$$

where I is the intensity of the light. From our Rabi frequencies and the sizes and powers of the beams, we calculate dipole matrix elements of $8.1(9) \times 10^{-4}\ ea_0$ for the pump transition and $2.0(2) \times 10^{-3}\ ea_0$ for the Stokes. We can use the matrix element to calculate the spontaneous decay rates Γ along each transition [156], which are given by

$$\Gamma = \frac{\omega_{P,S}^3}{3\pi\epsilon_0\hbar c^3} D^2 \tag{5.8}$$

Using the transition frequencies of $\omega_P = 2\pi \times 192.572$ THz and $\omega_S = 2\pi \times 384.230$ THz respectively, we get decay rates for these transitions of $\Gamma_\mathrm{P} = 2\pi \times 55(6)$ mHz and $\Gamma_\mathrm{S} = 2\pi \times 1.4(1)$ Hz. Since these rates are less than 10^{-4} of the total excited-state linewidth, we conclude that spontaneous decay along the pump and Stokes transitions is negligible compared to decay to other undetectable levels, i.e. the excited state is entirely open.

5.4 Excited state lifetime

Fitting equation 5.3 in figure 5.3 also give us the excited-state linewidth. The oscillations on the pump transition, figure 5.3(a), give a decay rate of $\Gamma = 2\pi \times 39(4)$ kHz, while the Stokes transition data, figure 5.3(b), give $\Gamma = 2\pi \times 24(6)$ kHz. Another identical measurement of the pump transition gave $\Gamma = 2\pi \times 41(9)$ kHz (data not shown). Our best estimate of the linewidth, $\Gamma = 2\pi \times 35(3)$ kHz, is a weighted average of these measurements. We use this in our model of the STIRAP transfer in section 5.5.

Our linewidth is a factor of 4 smaller than that measured in Innsbruck [79] from the width of the spectroscopic feature at low power. The reason for this discrepancy is currently unknown, and the lifetime is currently the least well-characterised factor in our system.

We can also measure the lifetime directly, using coherent Rabi oscillations on the pump transition. We drive a pair of π-pulses to move the entire Feshbach population to the excited state and back, and vary the hold time between them. We then fit the remaining population with an exponential decay, as shown in figure 5.4. This gives an even lower linewidth of $2\pi \times 10.1(9)$ kHz. We have not

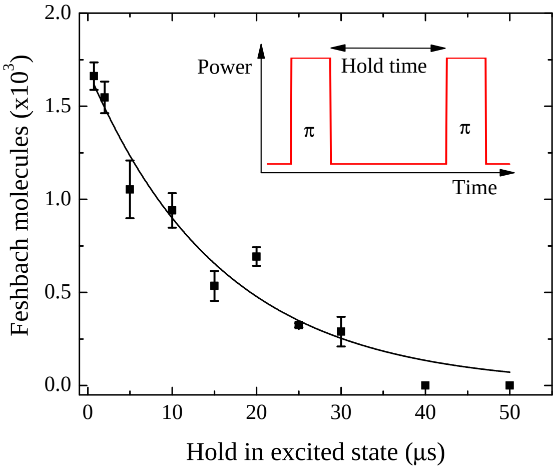

Figure 5.4: Number of Feshbach molecules remaining after a hold in the excited state. We use π-pulses, as seen in figure 5.3, to transfer the population to the excited state and back to the Feshbach state. A fit gives an excited state lifetime of 16(1) μs, and thus a linewidth of $2\pi \times 10.1(9)$ kHz. Inset: sketch of the pump beam pulse sequence, indicating the time changed (not to scale).

been able to reproduce this measurement. However, for all of these values we clearly meet the conditions for efficient transfer in equation 3.2.

5.5 Modelling the transfer

We model the STIRAP transfer using a numerical simulation based on an open three-level "lambda" system, as shown in figure 5.5. This system has a three-level Hamiltonian (not including decay to state $|L\rangle$):

$$\hat{H} = \frac{\hbar}{2}\begin{pmatrix} 0 & \Omega_\mathrm{P}(t) & 0 \\ \Omega_\mathrm{P}(t) & 2\Delta_\mathrm{P} & \Omega_\mathrm{S}(t) \\ 0 & \Omega_\mathrm{S}(t) & 2(\Delta_\mathrm{P} - \Delta_\mathrm{S}) \end{pmatrix}. \tag{5.9}$$

From this, we construct the Lindblad master equation, and add a term for decay $|E\rangle \rightarrow |L\rangle$. To make the transfer, the AOM drivers are modulated by voltage ramps of the form $V_\mathrm{P}(t) = \sin^2(\pi t/2T)$, $V_\mathrm{S}(t) = \cos^2(\pi t/2T)$ with a transfer time T. We analytically approximate the response $R(V)$ of our AOMs and RF amplifiers, and scale $\Omega(t) = \Omega_0\sqrt{R(V)}$ for each laser. We initialise the simulation

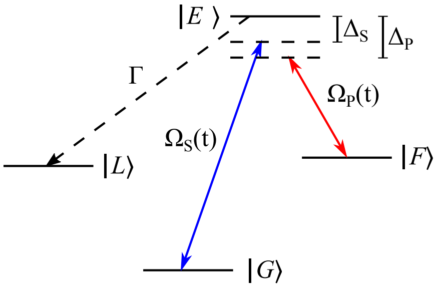

Figure 5.5: Level system for modelling STIRAP transfer to the ground state. $|F\rangle$ is the initial Feshbach state, $|G\rangle$ is the final ground state, and $|E\rangle$ is the lossy intermediate state which decays to many undetectable states represented by $|L\rangle$. $\Omega_{P,S}(t)$ are the pump and Stokes Rabi frequencies, and $\Delta_{P,S}(t)$ are the detunings.

in state $|F\rangle$. Ω_0 is scaled with the square root of the powers used in each individual experiment. We use the excited-state lifetime measured from the decay of the oscillations in figure 5.3. By numerically integrating the master equation using the QuTIP module in Python [157] with 200 ns timesteps, we calculate the population in each of the states through the transfer sequence. We repeat the sequence of $\Omega_{\mathrm{P,S}}$ in reverse to calculate the round-trip efficiency which can be matched to the experiment. The simulated Rabi frequency profile is shown in figure 5.2.

This basic model of the three-level open system overestimates the transfer efficiency as greater than 99%. In figure 5.6 we vary the length of the transfer ramps. Without noise, the round-trip efficiency approaches 1, but experimentally it drops for transfer ramps longer than ~ 50 µs.

We account for the lower transfer efficiency by adding the effects of laser linewidth and noise. The transfer efficiency is relatively insensitive to the 2-photon detuning, so we consider only the simplified case where the laser noise is uncorrelated but identical for both lasers. We do this by replacing the detuning $\Delta_{\mathrm{P,S}}$ with time-varying functions, following Yatsenko *et al.* [94]:

$$\Delta_{\mathrm{P,S}} \rightarrow \Delta_{\mathrm{P,S}} + \xi(t), \tag{5.10}$$

where $\xi(t)$ is some zero-mean random process. By averaging over 200 simulations for each data point, with randomised $\xi(t)$, we get the average transfer efficiency and populations through the transfer process. We might consider a simple model using normally distributed random noise. The effect of normally distributed noise

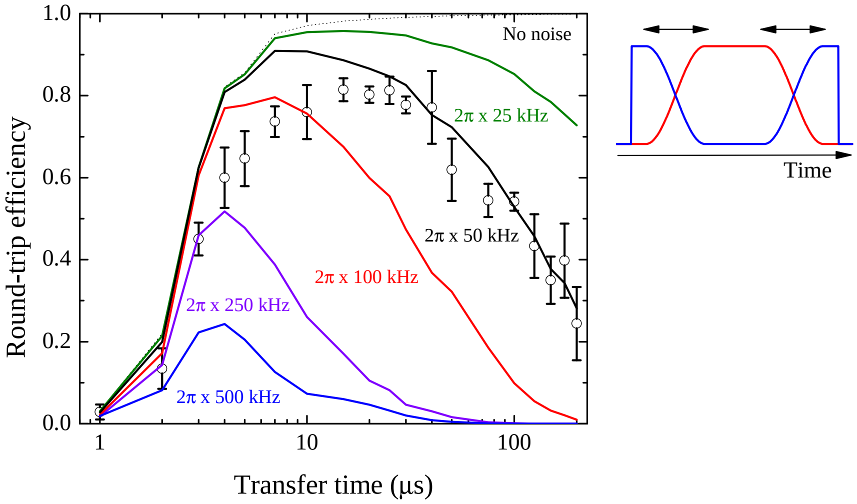

Figure 5.6: Simulation of STIRAP transfer with uncorrelated noise. Open circles: experimental data.Dotted: Noiseless model. Lines: Monte Carlo simulations with uncorrelated random Gaussian noise, with $1/e^2$ half-widths listed. Right: sketch of the pulse sequences (not to scale). The arrows indicate the independent parameter which was varied in this measurement. Red is the pump beam, blue is the Stokes.

with various widths is shown in figure 5.6. However, it is clear this does not give a good fit, as we see the simulated efficiency drops off much more at longer transfer times than we observe experimentally. We believe that this is because the model does not account for temporal correlations in the laser frequency. Yatsenko *et al.* [94] suggest a model which accounts for this using exponentially correlated coloured noise:

$$\xi(t+\Delta t) = \xi(t)e^{-C\Delta t} + h(t), \tag{5.11}$$

where $h(t)$ is a random Gaussian variable with second moment $DC(1-e^{2C\Delta t})$. C is the inverse phase correlation time of the laser field, while D is the phase diffusion coefficient, giving a noise amplitude of $\sqrt{DC}$.

We test this noise model in figure 5.7(a), using the same experimental data as in figure 5.6. This shows the effect of the phase correlations, with an uncorrelated model in red, a partially correlated model in black which gives the best fit to the data, and a perfectly correlated model in blue which overestimates the transfer efficiency for all transfer times. We also show in green the effect of increasing the

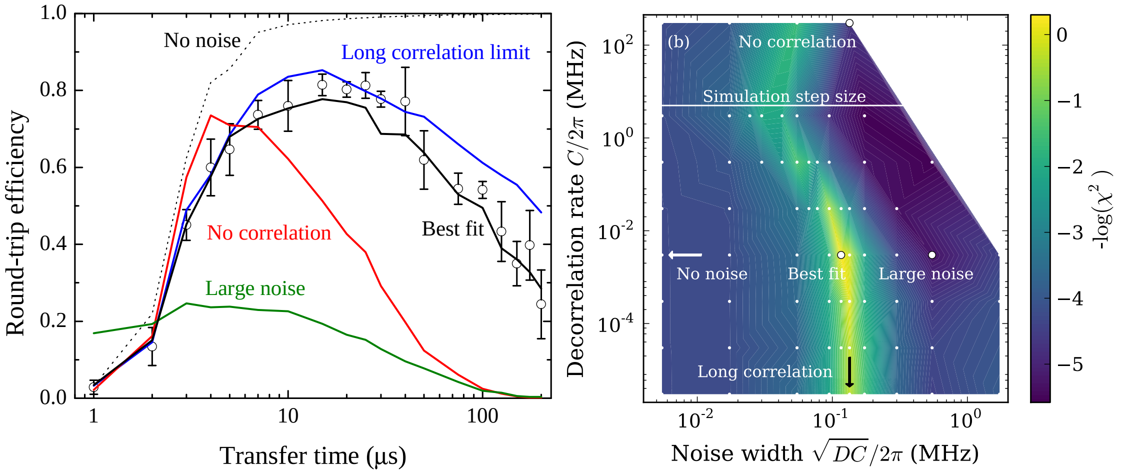

Figure 5.7: Effect of laser noise on STIRAP transfer. (a) Efficiency of STIRAP transfer as the ramp speed is varied. Experimental data are shown with 1σ standard errors. Monte Carlo simulations are shown for several different values of the laser decorrelation rate C and laser noise amplitude $\sqrt{DC}$, as explained in the text. The apparent efficiency for the green "large noise" curve at short times is from molecules remaining in the initial state, i.e. the transfer fails. (b) χ^2 goodness-of-fit contour plot for the data and model in panel (a). White dots are the values we have simulated. We indicate the parameters matching the curves in panel (a), and arrows denote limiting cases. Note the long ridge of good fits spanning several orders of magnitude in correlation time, approaching the long-correlation limit where a single frequency is randomly selected for each experimental shot or simulation run.

total noise amplitude at the same correlation time as the best fit, so that the laser is often far off resonance and the molecules never leave the initial state.

In figure 5.7(b) we estimate the values of D and C with the χ^2 goodness-of-fit to the experimental data in figure 5.7(a). The best fit occurs at a phase correlation time of around 300 µs, which corresponds to a short-term laser linewidth of $C = \sim 2\pi \times 3$ kHz. Measurements from delayed self-heterodyne interferometry [158] estimated the laser linewidth as $2\pi \times 0.5$ kHz. These are consistent, as we note that the best-fit point is remarkably insensitive to the phase correlation time, with only an order-of-magnitude estimate possible. We see this as the long vertical "ridge" of good fits in figure 5.7(a). However, the noise amplitude $\sqrt{DC}$ is much more sensitive, and we fit $\sqrt{DC} \sim 2\pi \times 130$ kHz, also consistent with our measurements of the shot-to-shot stability of our laser frequency [158]. In our case, where the correlation time is much longer than the transfer time, the frequency noise is effectively a nearly constant detuning, which matches with slow, shot-to-shot variation in the laser frequency.

We estimate the sensitivity of the transitions to magnetic field fluctuation. The theoretical results in figure 2.2(b) and (c) give Zeeman shifts of 2.22 MHz/G for the Feshbach state and 4.05 kHz/G for ground state. We have measured the Zeeman shift of the excited state as 0.4(2) MHz/G. Using these gradients, we estimate that the shot-to-shot frequency noise above corresponds to a field stability of ±60 mG for the pump transition, or ±260 mG for the Stokes. The former is within our measured field reproducibility over many weeks [67], though we have no way to measure the field stability on a shot-to-shot basis.

We use this model to recreate the transfer in figure 5.2. We use the best fit values of D and C from figure 5.7, and average over 200 runs of the simulation to generate the Feshbach and ground-state populations. The model slightly overestimates the round-trip transfer, but this is within our normal day-to-day variation in the transfer efficiency. It is clear that the model is a reasonable description of the transfer.

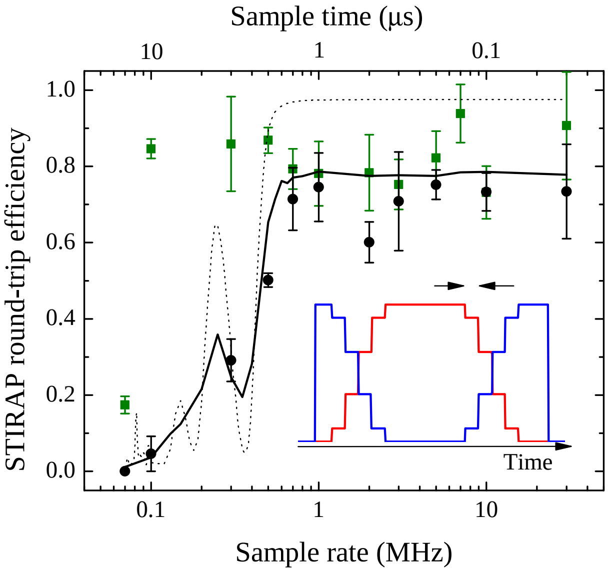

Figure 5.8: STIRAP efficiency with (green) and without (black) a low pass filter on the voltage profile used to create the STIRAP pulses, as the sampling rate is reduced. The one-way transfer time is 20 µs. The filter cutoff frequency is varied to maintain it at 1/8 of the sample frequency. The low pass filter recreates the smooth ramps needed for STIRAP transfer, even down to ~ 0.1 MHz where the unfiltered ramp becomes a step change. The solid line is a model of the unfiltered pulse profile, as explained in section 5.5. It has no free parameters. The dotted line is the same model, but not including laser linewidth. Inset: sketch of the unfiltered intensity ramps (not to scale), for a sample rate of 0.25 MHz. Red is the pump beam, blue is the Stokes.

5.6 STIRAP ramp sampling rate

We will now look at the effect of discrete sampling in the STIRAP ramps. In principle the ramps for STIRAP transfer should be smooth, analog ramps, but in practice they are generated by a discrete sampling process, which could in principle affect the transfer efficiency. The arbitrary waveform generator (AWG) which modulates the acousto-optic modulators in the STIRAP system has a limited bandwidth of 30 MHz, or a sampling time of 30 ns, which we can vary. Low sample rates turn the smooth ramps needed for STIRAP into step-like profiles which reduce the efficiency, while high sample rates limit the length of the pulse sequence because of the finite memory of the AWG. To solve this, we can use the AWG's built-in low-pass filter with a cutoff frequency of sample rate/8, which smooths the voltage ramp to the AOM. We see the effect of this filter in figure 5.8, showing the round-trip efficiency at varying sample rates. With the filter off, the efficiency drops dramatically when the sample time gets close to the 20 µs ramp time. However with the filter on, the efficiency remains high even when the sample time is 10 µs and the "ramp" is only three points. Figure 5.8 also suggests a slightly higher transfer efficiency with the filter on, but the difference has a significance of only 2.4 σ.

We test our model of the transfer using this data, by recreating the step-like profiles in the simulated pulse sequence. As in the basic model of the transfer (figure 5.2), the overall efficiency is slightly overestimated. The model exactly reproduces the sudden drop in efficiency for sample rates below 700 kHz, and does so with no free parameters.

The oscillations in the model as the sampling rate drops occur when the sample time matches with a two-photon 3π Rabi oscillation between the Feshbach and ground states. These oscillations seem to offer fairly high transfer efficiencies, but they are suppressed by dephasing caused by the laser noise. With careful choice of Rabi frequencies and the correct length of 2-photon pulse, much higher efficiency transfer to the ground state might be possible by driving a single π pulse. However, using coherent Rabi oscillations for the transfer relies on having a consistent Rabi frequency. Small changes in the power and alignment would

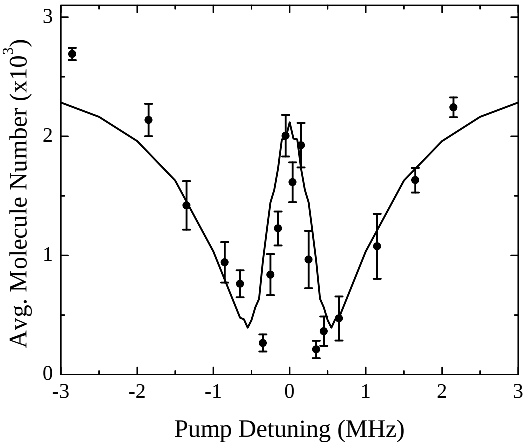

Figure 5.9: EIT-like profile for STIRAP transfer. The Stokes laser is set on resonance, and the pump laser is scanned. The remaining Feshbach molecules follow the characteristic W-shaped EIT lineshape. The solid line is a numerical model as described in the text. It has no free parameters.

change the Rabi frequency and make the transfer unreliable, while the STIRAP method is inherently insensitive to such changes.

5.7 EIT lineshape

We test the model of the STIRAP transfer further by reproducing an electromagnetically induced transparency (EIT) lineshape. In this experiment, we fix the Stokes laser on resonance with the $M_F = 5$ ground state, and scan the pump laser. When the pump light is resonant with the excited state, the Feshbach molecules are lost as in the one-photon spectroscopy in section 4.1. When the pump light reaches the centre of the transition, the two-photon resonance condition is fulfilled and STIRAP transfer occurs, so the Feshbach molecules are not lost. The two-photon resonance is much narrower than the one-photon resonance, and this produces the characteristic W-shaped EIT spectrum, which we see in figure 5.9. We know the shape of the STIRAP ramps and the Rabi frequencies of both transitions, so we can model the entire shape with no free parameters. As we see in figure 5.9, the model reproduces the shape. It somewhat overestimates the width of the EIT peak. The model without laser noise reproduces the width of the central peak accurately, so we deduce that the mismatch of the peak width is caused by remaining uncertainty in the laser noise model. There is also some uncertainty from the scaling to the total Feshbach molecule number, which is taken from ten points at a pump detuning of ±6 MHz. The match to the EIT lineshape demonstrates that the model reproduces a wide range of resonant and off-resonant effects.

This demonstrates a relatively easy and reliable way to transfer the molecules to the absolute ground state. We have fully characterised the transfer route and are now in a position to capture the ground state molecules in the optical trap and make further studies of their properties.

We now have a sample of ground-state molecules, but have so far kept them in the ground state for only 30 µs, and without a trapping potential. In this section we will describe trapping the ground-state molecules in the 1550 nm trapping potential after the transfer.

5.8 Ground-state temperature measurement

We measure the temperature of our molecules by releasing them from the trap into free flight and watching their expansion rate. The width of the cloud σ is given by

$$\sigma^2 = \sigma_0^2 + \frac{k_{\mathrm{B}}T}{m}t^2. \tag{5.12}$$

We square the expansion time and average cloud width, and make a linear fit. The temperature is given by the gradient $k_{\mathrm{B}}T/m$.

When measuring atomic temperatures, the expansion time is usually limited by the field of view of the camera, and the time for the atoms to fall out of frame. For the molecules the expansion time is limited by the low molecule number and optical depth, so that the dissociated molecules cannot be detected over the imaging noise after more than 5 ms time of flight.

We have no way to detect the ground state directly, but only indirectly by dissociating them into atoms. Thus if we release the ground-state molecules and allow them to expand, they will fall out of the STIRAP beam and will not be dissociated or detected. This means we cannot measure the ground-state temperature directly, so instead we measure the expansion rate after the molecules have been dissociated into atoms. The temperature must therefore be interpreted as an upper bound on the temperature, although we have seen no evidence of heating from the dissociation process.

Figure 5.10 shows a temperature of 2.2(2) µK after a very short 20 µs hold in the ground state, and a lower temperature of 1.0(2) µK after a 60 ms hold. The latter is the lowest temperature we have measured in the ground state so far. The reasons for the drop in temperature are discussed in more detail below below.

In figure 5.2, the 88(3)% round-trip STIRAP efficiency meant we had 2000 Feshbach molecules remaining after a 30 µs hold in the ground state. In figure 5.11(a),

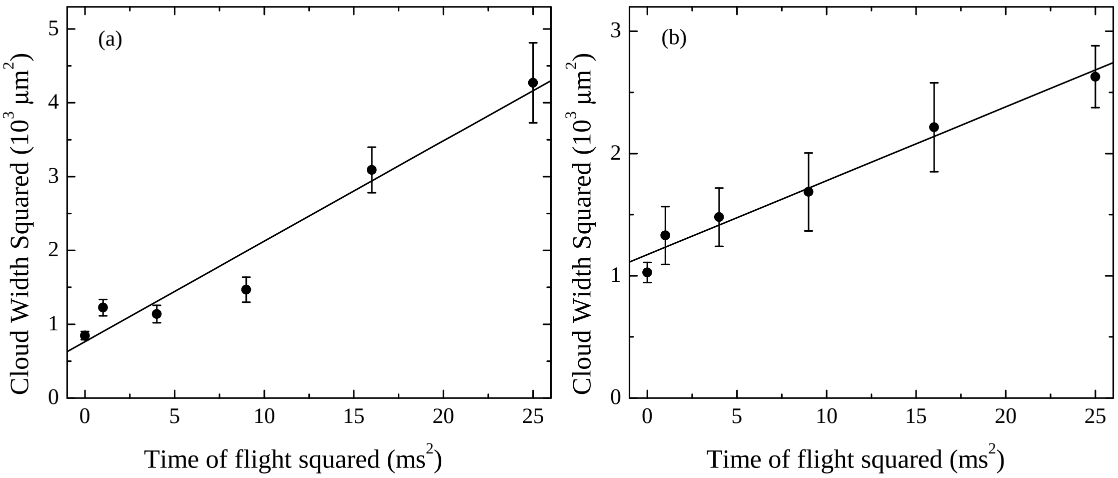

Figure 5.10: Temperature of the dissociated molecules after a 20 μs hold (a) and a 60 ms hold (b) in the ground state. These data sets are the highest and lowest temperatures shown in figure 5.11 below.

we see that the number drops by a factor of 2 in 21(7) ms after the molecules are loaded. This may be because after the transfer to the ground state, the molecules are not yet at equilibrium. The Feshbach molecules are loaded into the pure optical potential in only 50 ms, and so the loss of high-energy molecules may continue after the transfer to the ground state. We see this loss by looking at the change in temperature during the earliest part of the lifetime. We measure the temperature of the Feshbach molecules by time-of-flight expansion as in figure 5.10, after several hold times in the ground state. This gives us a better picture of the temperature drop in figure 5.10. The large number of data points needed for the temperature measurements mean we also get a precise measure of the molecule number at each point. We see a large drop in the molecule number within the first 50 ms and a corresponding drop in the temperature from 2.2(2) μK to 1.0(2) μK. From around 60 ms the temperature rises to 1.9(2) μK.

5.9 Ground-state lifetime

Measuring the lifetime of the ground-state molecules has a technical problem: the memory in the AWG creating the STIRAP pulses only allows sequences up to around $\sim$ 1 s long, or shorter if we use a higher sampling rate for the ramps. To

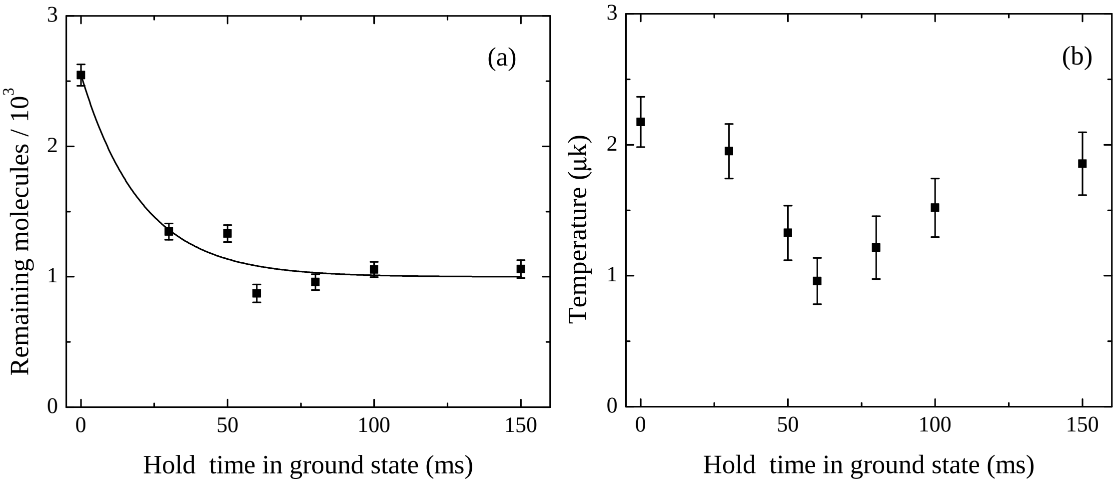

Figure 5.11: Fast loss of molecules after transfer to the absolute ground state. (a) Molecule loss with a fitted exponential decay time of 21(7) ms, showing the loss occurs within around 50 ms of the transfer. (b) Temperature during the same sequence, showing a distinctive drop as the sample thermalises or high-energy molecules escape from the trap.

make longer sequences, we add a simple circuit using a pair of DG419 integrated circuit analog switches, which swaps the pump and Stokes channels. We transfer the molecules to the ground state by STIRAP as in the previous section, then turn the optical trap back on, hold the atoms for some time and switch the pump and Stokes channels. Since the transfer ramps are symmetric between the two channels, we can use an identical transfer sequence to return to the Feshbach state. This method has a further advantage that the return transfer is synchronised to the optical trap turning off. If a single 1 s pulse sequence were used, the FPGA controlling the optical trap and the AWG controlling the STIRAP sequence would only be synchronised during the forward transfer. By the time the return transfer happened 1 s later, the accuracy of the FPGA clock speed, which is only 1 part in $\sim 10^4$, would mean the trap could turn off at a different time to the STIRAP pulse sequence.

In figure 5.12 we compare the lifetimes of the $M_F = 4$ and $M_F = 5$ molecular hyperfine states[1]. In this experiment, we only measure the molecule number for

---

[1] Details of how we select the hyperfine state are in section 6.3.

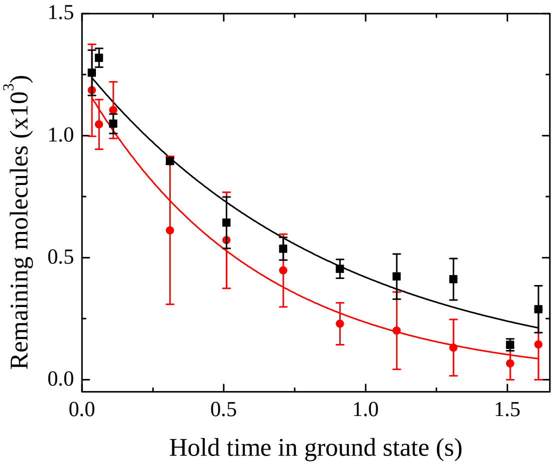

Figure 5.12: Lifetime comparison of the hyperfine states of the rovibrational ground-state. $m_f = 5$ (black) and $m_f = 4$ (red) states have lifetimes of 0.89(6) s and 0.6(1) s. The $m_f = 5$ state has a longer lifetime, consistent with this being the lower energy state and absolute ground state at this field.

holds longer than 35 ms, so we do not see the fast loss which is visible in figure 5.11(a). From the ground-state Zeeman structure in figure 6.1, we see that the $M_F = 5$ state is the absolute ground state, while $M_F = 4$ lies 0.19(1) MHz higher. We might then expect the $M_F = 4$ state to be less stable and have a shorter lifetime due to decay to lower Zeeman states. We see the $M_F = 4$ state has a lifetime of 0.6(1) s, and the $M_F = 5$ state has a slightly longer lifetime of 0.89(6) s under identical conditions, consistent with this hypothesis. Takehoshi *et al.* have observed a similar effect by populating the $M_F = 5$ state and reducing the magnetic field until it was not the hyperfine ground state [79].

The loss mechanism causing the 0.89(6) s lifetime has not yet been determined. Loss from collisions with background atoms typically leads to atomic lifetimes of > 1 minute and can be ruled out. We would expect two-body loss processes to be suppressed by energy considerations as we are in the ground state, and Innsbruck have seen evidence of such suppression [79]. However, they note that the suppression may not be complete due to thermal population of higher hyperfine levels. The residual loss could also be from three-body collisions. A more complete analysis of the lifetime would use a two- or three-body loss model. This is not practical in this case because the two- and three-body models are very difficult to distinguish without the ability to measure the increase in temperature. At the low molecule numbers in figure 5.12, it is very difficult to measure the expansion of the cloud and thus the temperature. Figure 5.11 does include the temperature for the earliest part of the lifetime, but we see a fast drop in the temperature and number, probably from rethermalisation and evaporation of the sample, which means we cannot easily distinguish two- and three-body losses. Optimising the loading could remove this fast loss and let us determine the loss mechanism.

5.10 Lifetime with external electric fields

As discussed in chapter 1, we would like to study the effects of long-range dipole-dipole interactions between the molecules, and particularly the effect of "sticky collisions" [6]. These collisions would manifest most obviously as an increase in the loss rate, *i.e.* a decreased lifetime, when an electric field is applied to induce an electric dipole moment in the molecules. We test this hypothesis by measuring the lifetime of the $M_F = 5$ state when electric fields are applied. We create the electric fields with the same electrodes which we used for Stark spectroscopy in section 4.4. The electric potential is turned on immediately after the transfer to the ground state and turned off before the transfer back to the Feshbach state. The experimental sequence is otherwise identical to the lifetime measurement in section 5.9.

In figure 5.13, we see that the lifetime decreases from 0.91(9)s to 0.27(2)s, which is a decrease of 7σ. This suggests that the electric fields cause a large decrease in the lifetime of the molecules. However, we cannot conclude from these results that the lifetime is reduced by a polar collision process, as we have yet to eliminate some potential technical causes, most notably the polarisation of the cell. When a large electric field is applied to the electrodes outside the vacuum chamber, the glass vacuum cell can become polarised or charged. This will always act to oppose and reduce the applied field at the sample, which can affect the return STIRAP efficiency, giving the appearance of loss. We quantify the speed and size of this effect in figure 5.14. A constant voltage is applied to the electrodes, and

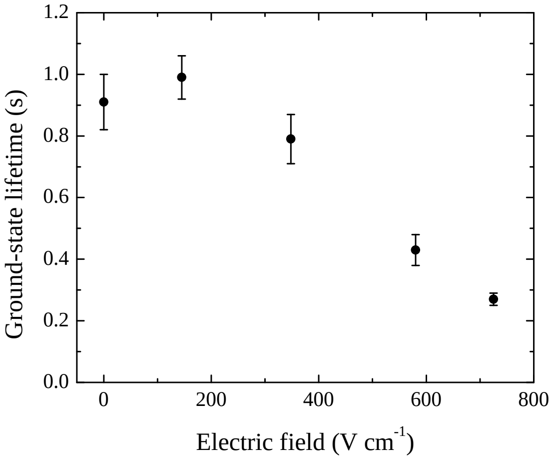

Figure 5.13: Change in observed ground-state lifetime as an external electric field is applied. The lifetime is measured as in figure 5.12. Note this is not necessarily indicative of dipole-related loss effects, because of technical effects as discussed in the text.

after some varying time we measure the shift of the pump transition from the zero-field case, using one-photon spectroscopy as in figure 4.4. We see that the field is reduced by over 10%, and the transition shifts by $-0.76(3)$ MHz/s, which corresponds to the field being reduced by 1.4 V cm^{-1}s^{-1}. In section 6.3 we will see that the two-photon resonance is only $\sim$ 350 kHz wide, and in chapter 4.4 we saw that the excited, ground and Feshbach state Stark shifts are very different, so the states will be shifted from two-photon resonance in a fraction of a second. This could be solved by adjusting the pump and Stokes wavelengths before the return transfer, however the difficulties of detuning the laser system during the experimental sequence, and the large number of detuning curves that would have to be taken (both transitions reoptimised for each hold time in the excited state) mean so far we have not been able to do so.

5.11 Conclusions

In this chapter, we presented transfer of ^{87}RbCs Feshbach molecules to the ground state using STIRAP. We reach 88% transfer efficiency and create around 2000 ground-state molecules. We fully characterised the transfer route with high-

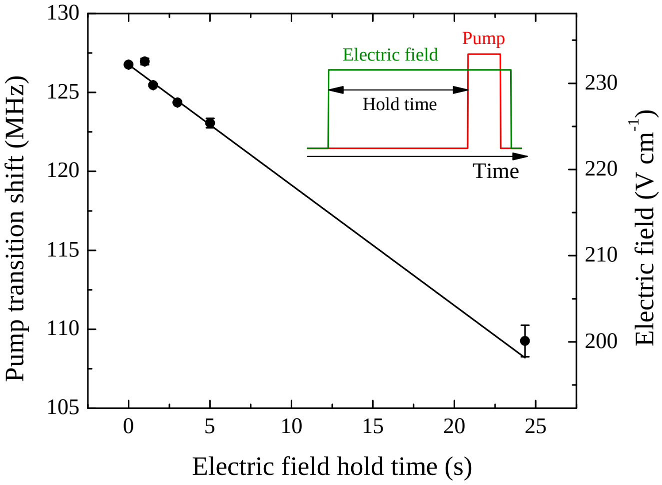

Figure 5.14: Reduction of the field from polarisation of the glass cell. A constant voltage is applied to the electrodes during a pump spectroscopy pulse, and for a varying time before it. The pump transition frequency is then measured as in figure 4.4. The field is reduced as the polarisation of the cell opposes the applied potential. A linear fit shows the transition shifts by $-0.76(3)$ MHz s^{-1}. Inset: a sketch of the experimental sequence (not to scale).

precision spectroscopy and direct measurements of the Rabi frequencies, and found these to be consistent with previous work. We modelled the transfer including a Monte Carlo model of the laser noise, and found that the main limitation to the transfer efficiency is shot-to-shot noise, rather than laser coherence. This transfer provides a reliable route for association of ground-state ^{87}RbCs molecules for use in future experiments.

We have demonstrated trapping of ground state molecules in an optical potential for over 1 s, and tentatively observed a reduction in the lifetime with applied electric fields, though there are still technical effects which could cause this.

Chapter 6

Precision binding energy measurement

In this chapter we will look more closely at the binding energy of the ^{87}RbCs molecule. An accurate characterization of the internal structure of even simple bialkali molecules has been challenging both theoretically and experimentally. The most precise measurement so far of the binding energy of these molecules is for KRb [78], where a frequency comb was used to measure the difference in laser frequency for the STIRAP transfer to a precision of ±1 MHz at a non-zero magnetic field. In ^{87}RbCs, the measurement precision has so far been approximately 20 MHz, limited by the precision of wavemeters. Such a measurement is shown in chapter 4, and a similar measurement has been made in Innsbruck [142].

Here, we present the most precise measurements of the binding energy D_0, or dissociation energy, of the lowest rovibrational state of the ^{87}RbCs $X^1\Sigma^+$ electronic ground state to date. First, we explain the working and stability of our novel frequency comb based on difference frequency generation (DFG), and how we use it to measure the 114 THz frequency difference between the STIRAP lasers. From this frequency difference we use theoretical models of the molecular structure to calculate the binding energy of the ^{87}RbCs molecule at zero magnetic field. The relevant molecular states are shown in figure 6.1.

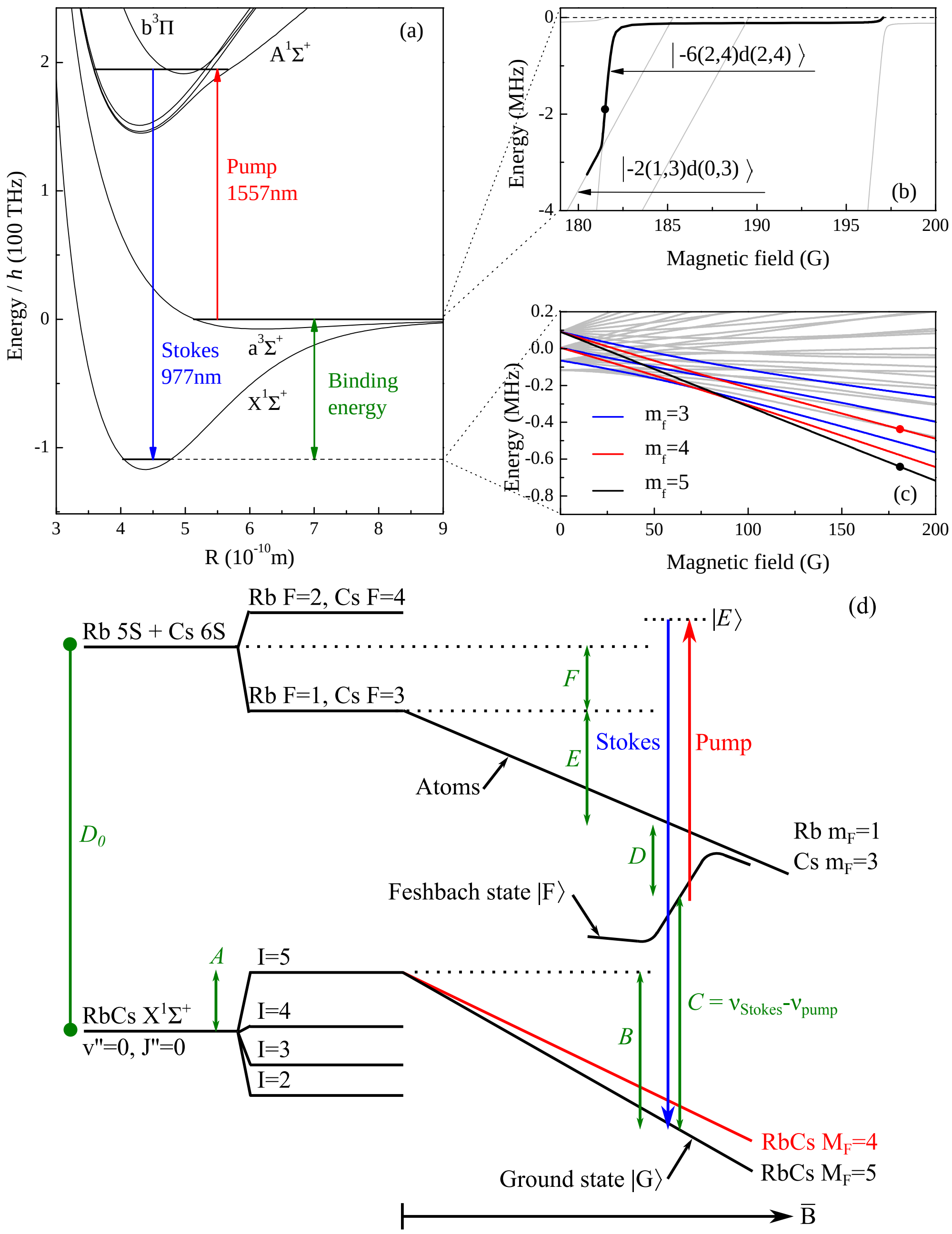

Figure 6.1: ^{87}RbCs molecular states relevant to the binding energy measurement. (a) The position of the energy levels we use for STIRAP within the molecular potentials. (b) Feshbach states close to dissociation. The dotted line is the Rb $|f = 1, m_f = 1\rangle$ + Cs $|3, 3\rangle$ threshold. (c) Zeeman splitting of the ground state into 32 energy levels from total molecular nuclear spin $I'' = 2, 3, 4$ and 5. Transitions to the highlighted states are allowed by selection rules. Dots indicate the states we address with our laser system. (d) Schematic view including the atomic levels. The initial Feshbach state, intermediate excited state and ground state are labeled as $|F\rangle$, $|E\rangle$ and $|G\rangle$ respectively.

6.1 Laser frequency measurement

We determine the binding energy with precision measurements of the pump and Stokes transition frequencies using a GPS-referenced frequency comb. Our frequency comb is the first of its kind, using the difference frequency generation technology developed by Toptica Photonics AG [159]. In this comb, the amplified output of an Er:fibre oscillator is compressed using a silicon prism compressor and then spectrally broadened using a highly nonlinear photonic crystal fibre to make a supercontinuum spanning more than an optical octave. This has a comb spectrum with frequencies $f = Nf_{\text{rep}} + f_{\text{CEO}}$. Two extreme parts of this supercontinuum are spatially and temporally overlapped in a nonlinear difference frequency generation (DFG) crystal. This cancels the carrier-envelope offset frequency (f_{CEO}) to produce an offset-free frequency comb spectrum at 1550 nm with a bandwidth of ~ 100 nm. Each comb tooth N then has a frequency $f = Nf_{\text{rep}}$. This output is then extended to different wavelength ranges by nonlinear frequency shifting and frequency doubling. This method to cancel f_{CEO} has the advantage of requiring no servo-loop feedback system, compared to the conventional $f - 2f$ approach where the high-frequency noise components of f_{CEO} cannot be cancelled [160]. The characterization of the phase noise of different comb teeth confirms the elastic tape model [161] with a fixed point at zero frequency [149].

The frequency comb is seeded by a mode-locked Er:fibre laser with an 80 MHz repetition rate, whose 10th harmonic is locked to an 800 MHz ultra-low-noise oven-controlled RF oscillator, which in turn is locked to a 10 MHz GPS reference (Jackson Labs Fury).

The absolute stability of the comb locked to the GPS reference has been measured by recording a beat note between a comb tooth and a laser stabilized to the Rb $5S_{1/2}(f{=}2)\rightarrow 5P_{3/2}(f'{=}3)$ line. Figure 6.2(a) shows the Allan deviation (AD) of the beat signal, compared to the AD of the GPS referenced oscillator to which the comb is locked. The AD of the beat follows a similar trend to the reference signal but deviates at longer time scales. This deviation is due to the drift in the lock-signal offset of the laser locked to the Rb spectroscopy line and is commonly observed over such time scales. These results show that measuring uncertainties down to 10^{-11} is practical with our comb system.

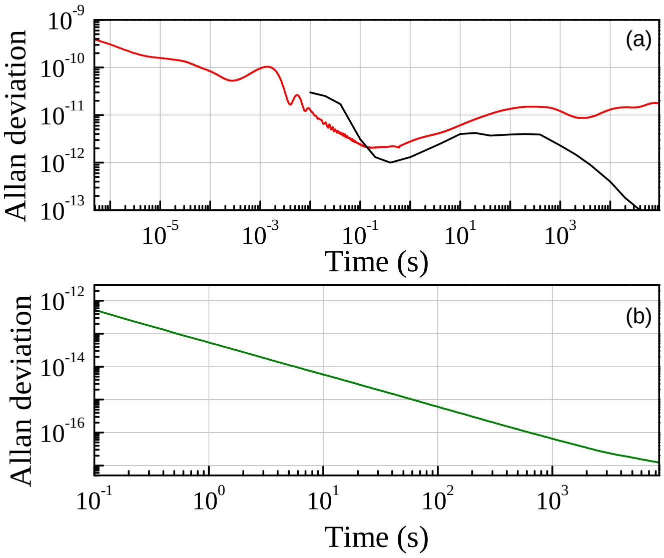

Figure 6.2: Measurements of the stability of the frequency comb. (a) Allan deviation (AD) of a beat between the frequency comb and a laser stabilized to the Rb $5S_{1/2}(f{=}2)\rightarrow 5P_{3/2}(f'{=}3)$ transition (red), and the AD of the GPS-referenced 10 MHz oscillator (black) to which the comb is locked. (b) AD of the beat signal between two identical DFG combs locked to a common reference. The beat was recorded at a wavelength of 1556 nm via a transfer oscillator [149]. Data courtesy of Toptica Photonics AG.

To quantify the lock noise of the comb, we measure the AD of a beat signal between two combs locked to a common RF reference. We observe an overall AD lower than the reference signal with no similarity to the AD of the reference signal (figure 6.2(b)). This indicates that the noise on the repetition rate lock is much smaller than the noise on the GPS reference, and the fractional uncertainty on the repetition rate exactly follows that of the GPS reference. Therefore we can consider the AD of the GPS signal at time scales greater than our experimental cycle to calculate the resulting deviation on the repetition rate.

The frequency difference between the two STIRAP lasers is measured with comb teeth separated by $\delta N = (306.8 - 192.6)$ THz/80 MHz $\sim 10^6$, so the uncertainty in the GPS clock frequency must be less than 10 mHz if we are to maintain an uncertainty in our measured laser frequency of less than 10 kHz. The AD over time scales shorter than the experimental cycle will add to the statistical error of the molecular round-trip signal. However, the AD over longer time scales will lead to a systematic offset in our measurements. From the specifications of the GPS reference we calculate that, over the course of one measurement, the AD leads to a systematic uncertainty of ± 23 Hz on the frequency difference between the two lasers. This is negligible compared to the other sources of uncertainty described later.

The absolute frequency of the lasers is measured by beating light from each of the STIRAP lasers with the nearest tooth of the optical frequency comb. A schematic diagram of the optical setup used to measure the beat note and the comb tooth number is shown in figure 6.3. The beat note is recorded on a spectrum analyzer (Agilent N9320B for the Stokes, Agilent N1996 for the pump), which is referenced to the same 10 MHz GPS clock as the comb. The frequency of the beat note is averaged and recorded over each three-second interval. We identify the nearest comb tooth (N) using a wavemeter with an absolute accuracy of 30 MHz (High Finesse WS-U), which we calibrate with lasers locked to well-known spectral lines in Rb, Cs and Sr.

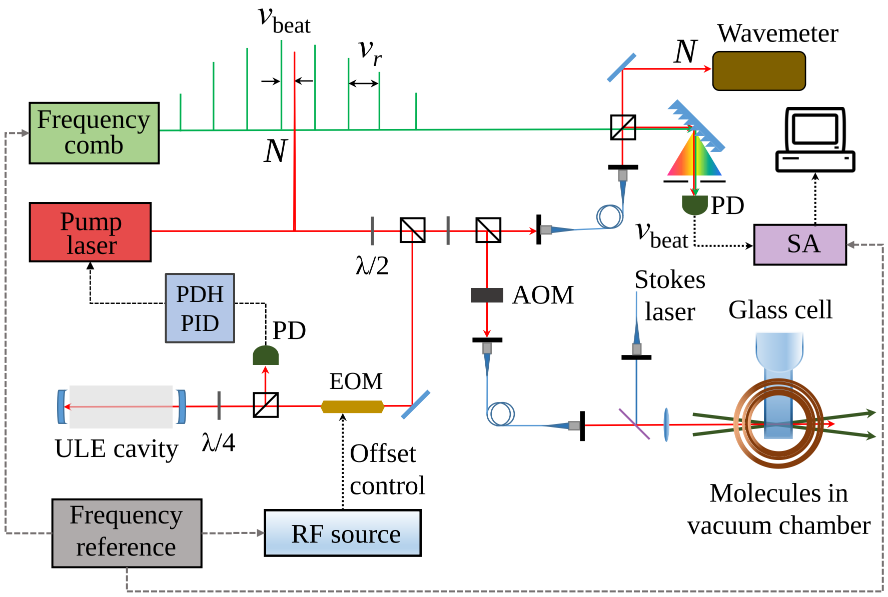

Figure 6.3: Schematic diagram of the experiment to carry out spectroscopy while recording the beat note (ν_{beat}) of the STIRAP lasers with the optical frequency comb. The beat signal between each STIRAP laser and the nearest comb line (N) is detected on a photodiode which is connected to a spectrum analyzer (SA). Both STIRAP lasers are frequency stabilized to a common ULE cavity using the Pound-Drever-Hall method [143]. Continuous tuning of each laser is provided by varying the RF driving frequency of a broadband fibre-coupled electro-optic modulator (EOM). The light reaching the molecules is offset in frequency by 80 MHz from that sent to the frequency comb by an acousto-optic modulator (AOM) which modulates the intensity of the light. Further details of the frequency stabilization and tuning of the STIRAP lasers are in chapter 3. The frequency comb, spectrum analyzers and EOM driver are all referenced to the same 10 MHz GPS disciplined oscillator. The figure shows the setup for the pump laser; the setup for the Stokes laser is identical.

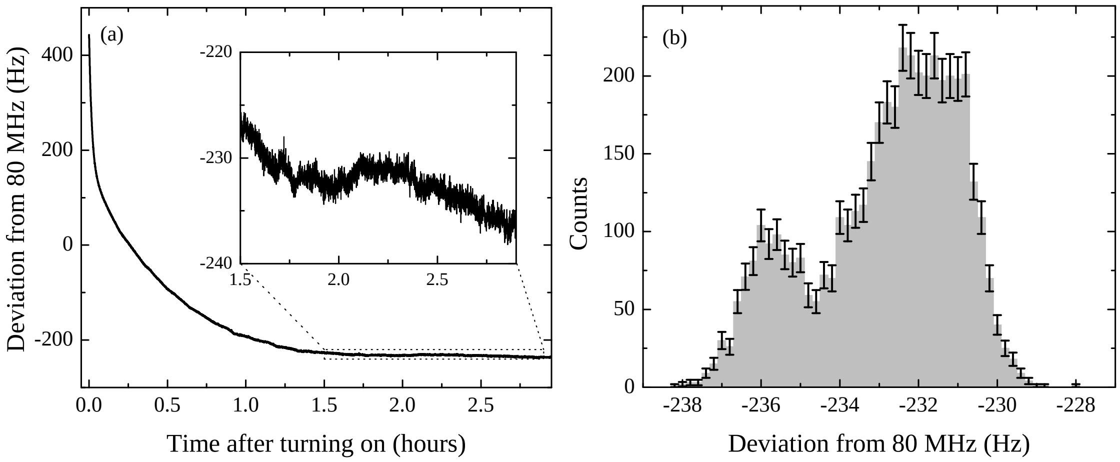

Figure 6.4: AOM driver frequency stability and warm-up time, measured on a counter. (a) The drive frequency settles to just below the nominal 80 MHz after about 2 hours. (b) Histogram of the last 1.5 hours of (a). The frequency distribution has a standard deviation of 1.8 Hz. From this data we conclude that the frequency instability is far smaller than the other errors in the binding energy measurement.

6.2 AOM frequency stability

The light reaching the molecules is offset from that sent to the frequency comb by a pair of acousto-optic modulators (AOMs), at +80 MHz and −80 MHz for the pump and Stokes respectively. These provide the analog intensity ramps for STIRAP, and are driven by ISOMET 532B fixed-frequency driver/amplifiers. These cause a constant frequency shift of the light sent to the atoms compared to that measured with the frequency comb. This shift is nominally 80 MHz, but the frequency is created by a VCO which has a specified accuracy of ±0.005% or ±4 kHz. We therefore make a separate measurement of the driving frequency of each AOM directly on a counter. In figure 6.4 we see that the pump AOM has an offset of −232.3(1) Hz from the nominal 80 MHz. A similar measurement of the Stokes AOM driver gave an offset of −705.4(3) Hz. The statistical uncertainty on this offset is negligible. We also see that the frequency takes several hours to stabilise after turning on, probably from the VCO heating up. The AOM drivers were left on for at least 12 hours overnight before each binding energy measurement to let them stabilise.

6.3 Energy difference measurement

Maximum STIRAP transfer efficiency is achieved when the laser frequencies meet the two-photon resonance condition, while any common detuning of both lasers has relatively little effect on the efficiency [22, 158]. By scanning their frequency difference and observing where we get maximum transfer efficiency, we determine the energy difference between the initial state $|F\rangle$ and final state $|G\rangle$.

To measure the energy difference, we fix the frequency of the pump laser on resonance with the Feshbach and intermediate states. We then vary the frequency of the Stokes laser and measure the efficiency of the STIRAP transfer. The beat notes of both lasers with the optical frequency comb are measured throughout. For each data point we subtract the pump and Stokes absolute frequencies measured with the comb, and add the shifts from the AOMs, to get an absolute frequency difference. This gives us a peak as a function of Stokes frequency, which we fit with a Gaussian to determine the energy difference between the initial and final states, as shown in figure 6.5. The optimal Stokes frequency is determined over ~ 4 hours.

The precision with which we can locate the two-photon resonance is limited by the shot-to-shot noise in the number of molecules which we produce. This noise results in the vertical error bars seen in figure 6.5. The uncertainties in the detuning (the horizontal error bars) are too small to be seen. A Gaussian fit gives an uncertainty on the centre of the spectroscopic feature of around ±8 kHz.

We found the same frequency difference between the pump and Stokes transition, within our experimental uncertainty, when using $|\Omega' = 0, v' = 35, J' = 1\rangle$ as an alternative intermediate state. This measurement was carried out using two-photon spectroscopy (where both the pump and Stokes light are pulsed on simultaneously) as the coupling strengths are not high enough for efficient STIRAP transfer. The experimental procedure for the two-photon spectroscopy of the ground state is discussed in chapter 4. This method, and the different transition strengths and

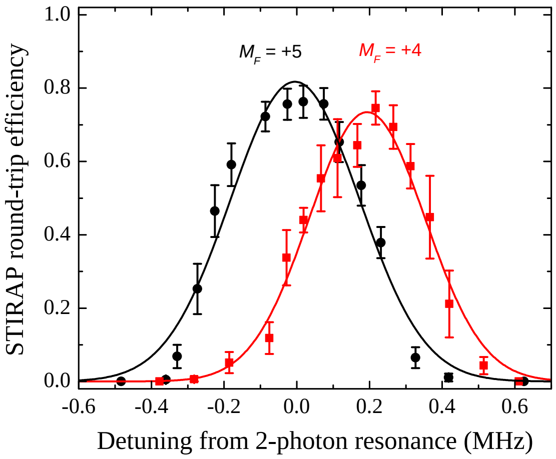

Figure 6.5: STIRAP transfer to different hyperfine sub-levels. The STIRAP round-trip transfer efficiency changes with the frequency difference of the pump and Stokes lasers for horizontal (black) and vertical (red) Stokes polarizations at a magnetic field of ~ 181.5 G. Black circles show the transfer to the $M_F = +5$ state, while red squares show the $M_F = +4$ state. Gaussian fits give a separation between the states of 0.194(10) MHz.

linewidths, results in a much wider spectroscopic signal, leading to uncertainties two orders of magnitude larger on the two-photon resonance.

6.4 Field calibration

If we wish to account for the Zeeman shift of the states, we must measure the magnetic field. We do this before and after each complete measurement using the microwave transition frequency between the $|f = 3, m_f = +3\rangle$ and $|4, +4\rangle$ states in atomic Cs. Figure 6.6 shows a typical field calibration. We prepare a sample of Cs atoms under identical conditions to the molecules. We drive transitions between the $|F = 3, m_F = 3\rangle$ and $|4, 4\rangle$ states of the $6S_{1/2}$ level using a 500 ms pulse of microwave radiation. We choose this transition because the states have opposite magnetic moments and thus the largest differential shift, giving the greatest precision in the field measurement. After the microwave pulse, we apply a field gradient and turn off the optical potential for 15 ms. This separates the $|3, 3\rangle$ and $|4, 4\rangle$ atoms by the Stern-Gerlach effect. We detect both states and fit Gaussians

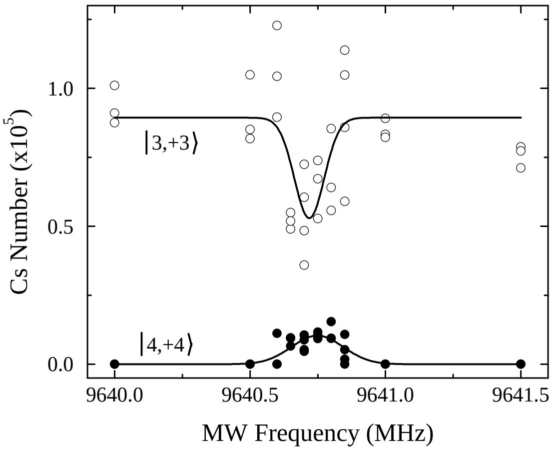

Figure 6.6: A typical field calibration. Microwaves drive the $|F = 3, m_F = +3\rangle \rightarrow |4, +4\rangle$ transition in Cs and we fit Gaussians to the populations of each to determine the transition centre. We measure a transition frequency of 9640.74(1) MHz, giving a magnetic field of 181.539(4) MHz. This is one of two field calibrations for the first line of table 6.2.

to the populations of each to get the transition frequency. This method makes it easy to locate the transition as the $|4, 4\rangle$ state is otherwise unpopulated. The zero background on the $|4, 4\rangle$ data also lets us remove one parameter in the fit, increasing the precision of the measurement.

6.5 Binding energy calculation

We will now combine the measured energy difference and magnetic field with theoretical models to determine the energy difference between the degeneracy-weighted centres of the atomic and molecular hyperfine manifolds. We must correct for several shifts which are included in our measurement: the atomic hyperfine splittings, the Zeeman shifts of the $|1, 1\rangle$ and $|3, 3\rangle$ atomic states, the binding energy of the Feshbach molecule relative to these atomic states, and the molecular ground-state hyperfine splitting and Zeeman shift. The binding energy is then

$$\begin{aligned} D_0 = \; & \nu_{\text{Stokes}} - \nu_{\text{pump}} \\ & + \text{RbCs hyperfine} \\ & - \text{RbCs Zeeman} \\ & + \text{Feshbach binding energy} \\ & + \text{Rb Zeeman} + \text{Cs Zeeman} \\ & + \text{Rb hyperfine} + \text{Cs hyperfine}. \end{aligned} \tag{6.1}$$

Using the letters defined in figure 6.1(d):

$$D_0 = A - B + C + D + E + F \tag{6.2}$$

These are shown diagrammatically in figure 6.1(d). The effects of all of these shifts are summarised in table 6.1, and we will discuss each of them below.

The Cs ground-state hyperfine splitting at zero field comes directly from the definition of the second, while the Rb splitting has been measured to < 100 µHz [162]. These are weighted by the degeneracies of the atomic hyperfine states to give the distance to the $5^2S_{1/2} + 6^2S_{1/2}$ centre. The atomic Zeeman splittings are calculated from the standard atomic Hamiltonian. The electron spin, electron orbital and nuclear g-factors are the CODATA recommended values [163]. We assume that the theoretical errors on these models are negligible.

We estimate the binding energy of the Feshbach state with respect to the $|1, 1\rangle + |3, 3\rangle$ threshold by combining the measurements and the coupled-channel model of reference [66], as shown in figure 6.7. There are 9 experimental points for the $|-6(2, 4)d(2, 4)\rangle$ state between 181.4 G and 181.9 G , and the coupled-channel model systematically underestimates the binding energies by 0.09(4) kHz. We correct for this deviation by fitting a global offset to the model in figure 6.7. This fitting has an experimental uncertainty of 0.04 MHz, which is shown in table 6.1 but is not included in the statistical error bars in figure 6.8.

The $J = 0$ rovibrational ground state has 4 hyperfine levels with nuclear spins $I = 2, 3, 4, 5$. In the presence of a magnetic field, these are split into 32 hyperfine and Zeeman states originating from the nuclear spin coupling to the magnetic field. These energy levels were calculated using the molecular Hamiltonian and

Source	Correction (MHz)	Error (MHz)
$\nu_{\mathrm{Stokes}} - \nu_{\mathrm{pump}}$	114 258 363.067	0.006
Feshbach binding energy	1.838	0.04
Rb Zeeman	194.084	
Cs Zeeman	134.353	
RbCs Zeeman	0.734	
Total Zeeman		0.013
Cs hyperfine	$\frac{9}{16} \times 9\,192.631\,770$	$\equiv 0$
Rb hyperfine	$\frac{5}{8} \times 6\,834.682\,611$	$< 10^{-10}$
RbCs hyperfine (I=5)	0.091	
Binding energy D_0	114 268 135.23	0.04

Table 6.1: All the corrections, and their respective experimental errors, which must be added to each measurement of the energy difference $\nu_{\mathrm{Stokes}} - \nu_{\mathrm{pump}}$ to give the binding energy with respect to the degeneracy-weighted hyperfine centroids of the free atoms and the RbCs rovibrational ground state. The uncertainty in the Zeeman shift is from the uncertainty in the measured magnetic field. Additional systematic uncertainties apply as explained in the text. The values shown are from the second measurement in figure 6.8 at a magnetic field 181.538(6) G driving a transition to the $M_F = 5$ hyperfine ground state. In section 6.6 we take an average of five such measurements.

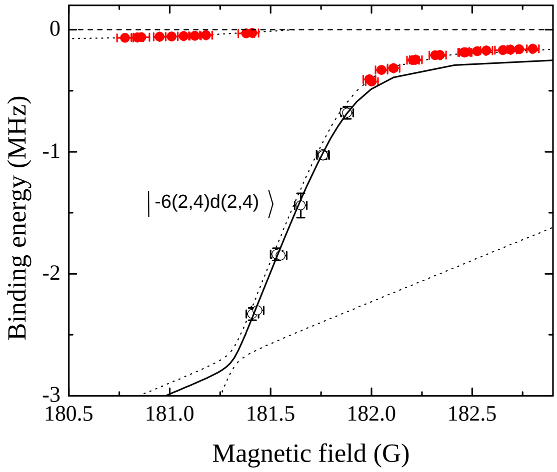

Figure 6.7: The calculated positions of the highest-lying bound states for ^{87}RbCs (dotted lines) together with the positions measured by free-bound magnetic-field modulation spectroscopy. The solid black line shows the relevant state fitted with a global offset. The measurements included in the analysis of the required shifts of the calculated values (see main text) are coloured black, and the other data points in the set are coloured red. There are 9 points included in the fitting; some of them nearly overlap. Experimental data taken from Takekoshi *et al.* [66].

parameters in reference [126] and are plotted in figure 6.1(c). We subtract both the hyperfine and the Zeeman shifts to give the binding energy of the ground-state hyperfine centroid, i.e. the zero of the energy axis in figure 6.1(c).

There are also theoretical uncertainties associated with the model of the ground-state hyperfine structure. The hyperfine splitting of the $I = 2, 3, 4, 5$ states is determined almost entirely by the scalar nuclear spin-spin coupling constant c_4, which was calculated using density-functional theory (DFT) by Aldegunde *et al.* [126]. We estimate that the uncertainty on c_4 is ±30%, giving an uncertainty of ±27 kHz on the position of the $I = 5$ state relative to the degeneracy-weighted hyperfine centroid. The Zeeman shift is determined by the nuclear shielding constants, also from DFT [126], but we estimate that the uncertainties in these shieldings cause an uncertainty of only ±1 kHz. These uncertainties are included as a separate "theoretical" uncertainty in the final value of the ground-state binding energy.

We selectively address different hyperfine sublevels of the rovibrational ground state by changing the polarization of the Stokes laser [79] while keeping the pump laser polarization fixed parallel to the quantization axis. The weakly bound state from which we begin our STIRAP transfer has a total angular momentum projection quantum number $M_F = +4$. In the case of Stokes polarization parallel to the quantization axis, we drive π transitions and address a ground state where the M_F value is unchanged. If, on the other hand, the Stokes polarization is perpendicular to the quantization axis, we drive $\sigma^{\pm}$ transitions and address ground states with either $M_F = +3$ or $M_F = +5$.

In figure 6.5, we see the effect of scanning the Stokes laser frequency on the efficiency of STIRAP transfer for both parallel and perpendicular polarizations. The coupling strengths to the hyperfine ground states are such that we have sufficient laser power to populate only two of the available hyperfine states, which are separated in energy by 0.194(10) MHz. The measured energy difference, in combination with knowledge of the states accessible with different Stokes polarizations, allows us to identify the two states with $M_F = +5$ and $M_F = +4$ as indicated in figure 6.1(c), agreeing with previous results [79]. Weak couplings to the $M_F = +3$ states mean we have not been able to observe them. Both of these Zeeman states correspond to the $I = 5$ hyperfine state. Because of mixing between the $I = 4$ and $I = 5$ states in a magnetic field, the measured splitting of 0.194(10) MHz has some dependence on the spin-spin coupling constant c_4. It corresponds to a value $c_4 = 0.023(7)$ MHz, which agrees within its error bars with the value of 0.01734 MHz from DFT calculations [126] and is also consistent with our attribution of an uncertainty of 30% to the latter value. We note that at a field of ~ 181.5 G the $M_F = +5$ state is the lowest-energy sublevel, as shown in figure 6.1(c).

We must also consider the effect of the uncertainty in the magnetic field. We have considered the atomic and molecular Zeeman shifts separately above, but with the uncertainty in the field they must be considered together. We multiply the uncertainty in the field by the difference in magnetic moment between the Feshbach and ground states to give the associated uncertainty in the binding energy. This is shown in table 6.1, and is added to the uncertainty from the frequency difference measurement above to give the total statistical uncertainty on the binding energy.

6.6 Measurement campaign

We have repeated the measurement outlined in section 6.5 five times on different days, and observed similar results for the energy difference each time, within experimental errors. In this section, we combine these measurements to give a value for the binding energy D_0. All five measurements are summarised in figure 6.8, and the precise values for each measurement are shown in table 6.2.

The measurement shown in red in figure 6.8 uses the $|\Omega' = 0, v' = 35, J' = 1\rangle$ intermediate state. The polarisations are such that we expect to address the $M_F = 3, 5$ states, but the large spectroscopic linewidth means this measurement does not resolve the ground-state hyperfine structure. The main purpose of this measurement is to confirm that we have identified the frequency comb tooth correctly. The other four measurements use the $|\Omega' = 1, v' = 29, J' = 1\rangle$ state in the coupled $A^1\Sigma^+ + b^3\Pi$ potential. Of these, three are measured with the $M_F = 5$ ground-state hyperfine level, and one uses the $M_F = 4$ state.

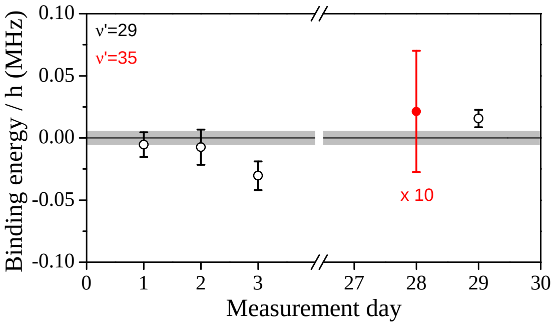

Figure 6.8: Binding energy of the ^{87}RbCs molecule measured on different days, with experimental error bars. Statistical error bars are shown; additional systematic uncertainties apply as explained in the text. The vertical scale is offset by the mean value of 114 268 135.237 MHz. The grey shaded region represents the 5 kHz experimental error on the mean. Black (red) data points show the binding energy calculated from two-photon spectroscopy via $|\Omega' = 1, v' = 29, J' = 1\rangle$ ($|\Omega' = 0, v' = 35, J' = 1\rangle$) as the intermediate state. The $|\Omega' = 0, v' = 35, J' = 1\rangle$ measurement and error bar have been divided by 10 for clarity. The larger experimental errors in two-photon spectroscopy via the $|\Omega' = 0, v' = 35, J' = 1\rangle$ state are due to the poor signal-to-noise ratio of the molecular spectroscopy signal.

Polarization	M_F	$\nu_{\text{Stokes}} - \nu_{\text{pump}}$ (MHz)	B (G)	D_0/h (MHz)
V_P, V_S	4	114 258 362.874(8)	181.542(3)	114 268 135.232(10)
V_P, H_S	5	114 258 363.067(6)	181.538(6)	114 268 135.230(14)
V_P, H_S	5	114 258 363.075(8)	181.552(4)	114 268 135.207(12)
V_P, H_S*	5	114 258 363.2(5)	181.510(3)	114 268 135.4(5)
V_P, H_S	5	114 258 363.048(5)	181.519(2)	114 268 135.253(7)

Table 6.2: Summary of each independent measurement of the binding energy in the ground state. Both the magnetic field and the polarization of the pump light are vertical (V_P). The Stokes light may be either vertical (V_S) or horizontal (H_S) to access ground-state hyperfine levels with either $M_F = 4$ or $M_F = 5$. For each measurement we show the absolute frequency difference measured for each laser ($\nu_{\text{Stokes}} - \nu_{\text{pump}}$), the magnetic field during that measurement (B), and the binding energy of the ground state at zero field (D_0). Statistical uncertainties are shown; additional systematic uncertainties apply as explained in the text. An asterisk* indicates a measurement using two-photon spectroscopy via the intermediate $|\Omega' = 0, v' = 35, J' = 1\rangle$ state. All other measurements rely on optimization of the round-trip STIRAP efficiency via the intermediate $|\Omega' = 1, v' = 29, J' = 1\rangle$ state.

Following the procedure in the previous sections, we calculate a value for the binding energy for each measurement. Taking a weighted mean we get a final value for the binding energy of ^{87}RbCs of

$$\begin{aligned} D_0 &= h \times 114\,268\,135.24(4)(3)\ \text{MHz} \\ &= hc \times 3811.574\,714\,0(13)(9)\ \text{cm}^{-1}. \end{aligned}$$

The first uncertainty arises from the experimental error and the second one arises from the theoretical uncertainties in the ground-state hyperfine structure. Our experimental measurements of the energy difference between the initial Feshbach state and the final ground state are one order of magnitude more precise than the total uncertainty.

This value is a 500-fold improvement in accuracy over previous measurements averaging 3811.5759(8) cm^{-1} [80, 142]. The most precise determinations of a molecular binding energy we know of are precisions of $\Delta E/E \sim 10^{-8}$. These are in $^{40}\mathrm{K}^{87}\mathrm{Rb}$, which is measured with 8×10^{-9} precision at a finite magnetic field [78], and H_2 with 1×10^{-8} precision [164]. It has been suggested that the H_2 binding energy could be measured to 5×10^{-11} with current techniques [165]. Our fractional uncertainty is 4×10^{-10}, and improved models and measurements of the Feshbach and ground-state structure could reduce this as far as 5×10^{-11}.

6.7 Conclusions

We have measured the binding energy of the ^{87}RbCs molecule using an optical frequency comb based on difference-frequency generation [159, 166]. The results for different intermediate states $\sim$ 1.65 THz apart agree within their experimental uncertainties and we are able to resolve the nuclear Zeeman splitting of the molecular ground state. The accuracy of our ground-state binding energy measurement is limited by uncertainties in the theoretical models of the molecular structure. This is, to our knowledge, the most accurate determination to date of the dissociation energy of a molecule. The ability to measure molecular transitions with high precision is also highly relevant to proposed searches for variations in fundamental constants [7, 167–174].

Chapter 7

A 1064 nm lattice potential for ^{87}RbCs molecules

Using the 1550 nm trap to hold our ground-state molecules restricts the experiments we can do for two reasons. First, to achieve the 88% transfer to the ground state in chapter 5, we had to turn off the optical trap and make the transfer in free space. This means the STIRAP transfer pulses must be carefully synchronised with the optical trap turning off to within ~ 100 µs, which is difficult when the forward and reverse transfer are separated by ~ 1 s and the FPGA clock only has a specified accuracy of ~ 1 part in 10^4. Second, it is possible the transfer heats the sample, as the Feshbach and ground states have different predicted polarisabilities (see table 7.1) and hence experience different trapping frequencies. In our lifetime measurements, we change the trapping beam powers to compensate for this, but again this increases the complexity of the experimental sequence.

To remove these issues, we have built and are testing a new trap at 1064 nm, which has several advantages over the 1550 nm trap. We also note that the group of H. C. Nägerl in Innsbruck [79] use a 1064 nm trap and have achieved transfer efficiencies of 90% using the same molecular transitions. In this chapter we present our progress in loading molecules into a 1064 nm trapping potential and 1D lattice.

We have tested two iterations of the trap along similar beam paths, with light derived from two different lasers, with different intended purposes. In the first iteration, we used a 50 W multimode 1064 nm fibre laser to create a trap with a much larger volume than the 1550 nm trap. This laser broke part-way through testing, but showed some curious results which are presented in section 7.3 for comparison. The second iteration uses a 2 W non-planar ring oscillator [176] to make a trap with a similar size to the 1550 nm trap. The lower power means the maximum trapping potential is shallower, but the single-mode, narrow linewidth laser lets us make a lattice potential. The details of this lower power setup and results from it form the bulk of this chapter in sections 7.4 onwards.

7.1 Design considerations

When designing a new trap for the molecules, we had several considerations and constraints. First, the setup must be installed alongside our original 1550 nm trap with minimal changes to the existing equipment. Second, the new and old traps must have similar a similar geometry and orientation, to simplify transfer between the old and new traps, and also so that the STIRAP beams can pass directly along the long axis of both traps and address the entire molecular sample with a high Rabi frequency. It also means the long axis of the trap is perpendicular to the imaging axis, which makes aligning the trap and determining the trap frequencies easier. Third, we would like to turn the trapping potential into a lattice, to increase the trapping frequency along one or more directions, giving higher densities. Fourth, we need to use a wavelength far from the 980 nm and 1550 nm STIRAP wavelengths, to minimise the AC stark shifts that disrupt the transfer in the original trap (see sections 5.1 and 5.2).

7.2 Optical design

We choose to build the trap using lasers at 1064 nm for several reasons. First, high-power, high-stability turnkey Nd:YAG lasers are readily available, and they give better beam profiles and higher reliability than systems based on, for example, tapered amplifiers. Fibre amplifiers are also readily available, offering ~ 50 W of narrow-linewidth light[1]. Second, at 1064 nm the ^{87}RbCs Feshbach and ground

---

[1] *e.g.* Nufern NUA-1064-PB-0050-D0 or IPG Photonics YAR-50K-LP-SF

	1550 nm	1064 nm
^{87}Rb [177]	424.7(7)	686.9(9)
Cs [177]	572(1)	1162(2)
^{87}RbCs Feshbach state [137]	996.4	1846.8
^{87}RbCs ground state [137]	870.71	1848.7

Table 7.1: Polarisabilites of the species in our experiment at the trapping wavelengths we use. All are in atomic units (a_0^3). Note that 1064 nm is very near the magic wavelength for the Feshbach and ground states where the polarisabilities, and thus trap frequencies, are the same. The errors on the atomic polarisabilities are taken from [177].

states have nearly identical polarisabilities as shown in table 7.1. This means the STIRAP transfer should not alter the potential and there should be no rethermalisation. Third, the polarisabilities are generally higher for all species, meaning higher trap depths and frequencies are possible with the same laser power.

As shown in figure 7.1, we use a bow tie layout, where the trapping beam passes through the cell twice, allowing us to recycle the power and increase the intensity of each beam. The beams nearly counterpropagate and the first beam is vertically polarised. A single $\lambda/2$ waveplate between the first and second passes is rotated to set the polarisation of the second beam parallel or perpendicular to the first. The main disadvantages of the bowtie configuration are a fixed ratio between the beam powers, which is $\neq 1$ because of loss in the optics between the beams, and more difficult alignment since the second beam must be aligned with the first already in place and trapping atoms.

The 1064 nm trapping beams run “inside” the old 1550 nm beams, as shown in figure 7.1. The beams intersect at $2\theta = 14°$, compared to $22°$ for the 1550 nm trap. The shallow intersection angle gives a long, thin trap with the ratio of the axial and radial trapping frequencies being $\omega_r/\omega_z = 7.7$. As with the 1550 nm trap, the STIRAP beams propagate along the longest axis of the trap, giving the smallest possible molecular target. This means the STIRAP beams can be tightly focussed to give the highest intensities and Rabi frequencies, and the STIRAP optics do not have to be changed to target the new trap.

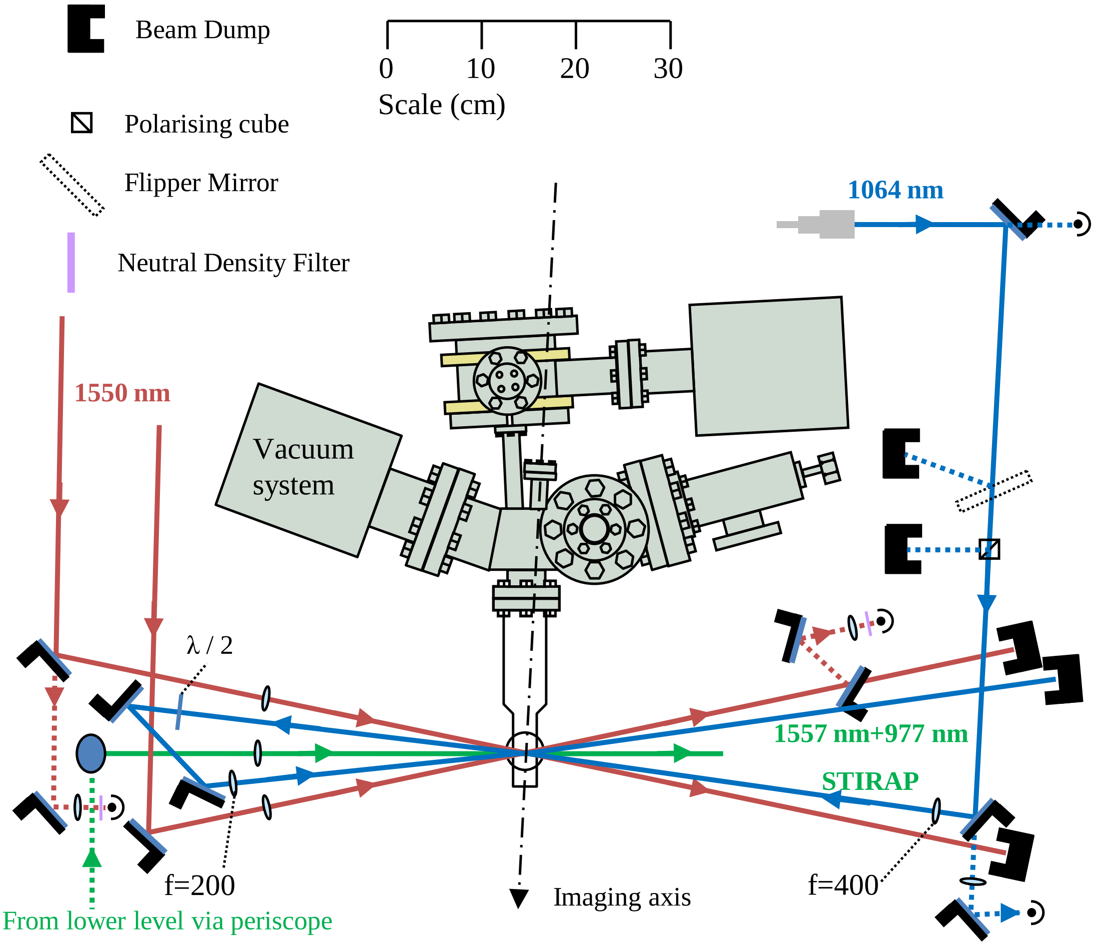

Figure 7.1: Optical layout of the new optical trap. Blue: new 1064 nm optical lattice/harmonic trap. Red: old 1550 nm harmonic trap. Green: STIRAP beams, aligned with the long axis of both traps.

7.3 Initial large trap design

This trap was originally intended for use with ^{85}Rb. A larger, higher power trap would increase the loading efficiency from the magnetic trap and allow us to reach higher atom numbers and phase space densities than was possible in the 1550 nm potential [92]. We also hoped to use it as a reservoir trap for ^{87}Rb, loading the original (smaller) 1550 nm potential from this larger trap, increasing the numbers of both ^{87}Rb and Cs and thus the molecule numbers after magnetoassociation. All the work here uses ^{87}Rb which is well-suited to evaporative cooling and thus easier to use for aligning and testing.

We used a 50 W multimode fibre laser at 1070 nm (IPG Photonics YLR50-LP). This provided a vertically polarised, 1 mm radius fibre-coupled beam, focussed to a $\sim$ 160 μm waist at the trap centre by an f = 400 mm lens. A second lens, f = 200 mm in the $4f$ configuration, refocused the light to a second spot of the same size. The layout is as shown in figure 7.1, except we used a high-power AOM (Isomet M1135-T80L) after the fibre to control the power. During the measurements here, the beam power was not actively stabilised, to allow maximum power and thus the deepest trapping potential.

To load the large-volume reservoir trap, we turned on a single beam, or a two-beam crossed trap, at $\sim$ 40 W at the beginning of the RF evaporation stage in the magnetic trap. After the RF evaporation, we ramped down the magnetic trap to just below the 30 G/cm levitation gradient for ^{87}Rb in 1 s, loading the atoms into the optical trap in the $|F = 1, m_F = -1\rangle$ state. We note this sequence was not heavily optimised for high atom numbers or low temperatures.

We aligned the trap to overlap with the original 1550 nm trap, so we could use the larger 1064 nm trap as a reservoir to increase loading. The 1550 nm trap itself is postioned 80 μm below the field zero of the quadrupole trap to avoid Majorana losses from spin-flips at the field zero.

We aligned the first pass of the beam using a single-beam magneto-optical hybrid potential with the ^{87}Rb atoms in the $|1, -1\rangle$ state. The atoms were confined radially by the 1064 nm beam, and confinement along the single beam was provided by the magnetic quadrupole gradient. We placed the trap 80 μm below the field

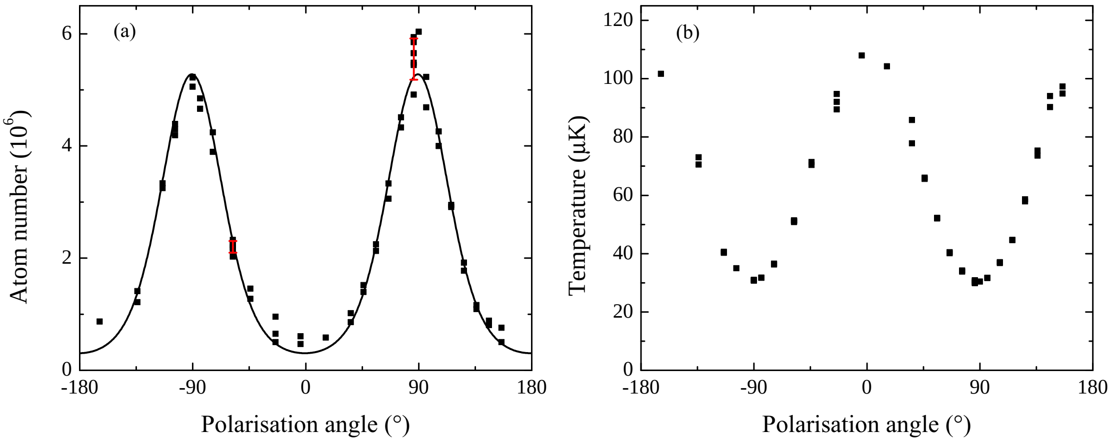

Figure 7.2: Effect of polarisation angle on trap loading, for a multimode laser. (a) Loss of atoms after a 1s hold in the multimode laser trap, for varying angles between the polarisations of the two beams. Error bars are shown for $\theta = -56°$ and $\theta = 86°$ where 6 data points were taken for each. The line is a fit to equation 7.2, a simple empirical loss-rate model. (b) Temperature variation over the same experiment. We see that the temperature is much higher and the atom number much lower when the beam polarisations are parallel.

zero of the magnetic quadrupole trap, overlapped with the 1550 nm trap. For the second pass, we used RF adiabatic rapid passage to transfer the ^{87}Rb atoms into the $|1,1\rangle$ high-field-seeking state, as in the 1550 nm trap. For this state the magnetic quadrupole field is anticonfining along the beams, preventing the formation of a single-beam trap. The only way to form a trap was then by overlapping the two beams, so that the magnetic anticonfinement along each beam was "blocked off" by the other beam. This resulted in a two-beam crossed trap overlapped with the 1550 nm trap.

We saw a strong dependence of the atom number on the polarisation angle between the two beams. In figure 7.2, we loaded Rb atoms in the $|1,+1\rangle$ state into a levitated trap and looked at the number remaining after a 1 s hold. We rotated the polarisation of the second beam with a waveplate, and saw that the atom number drops by more than an order of magnitude when the beam polarisations were parallel.

The cause of this loss is not clear. One explanation could be interference between the two beams, with the multimode spectrum of the laser causing a time-varying weak lattice structure which heated the atoms. We also see a large change in temperature in figure 7.2. We note that the 1 s hold in the trap may not have been long enough to thermalise in the trap. However, the dramatic rise in temperature for parallel beam polarisations is qualitatively consistent with the sample being heated by weak interference between the beams.

We can investigate this process by modelling the variation in atom number (N) with some loss process given by

$$\frac{dN}{dt} = -NAI_0\cos^2\theta \tag{7.1}$$

where $I_0 =$ is the "accidental" lattice intensity when the angle θ between the two beam polarisations is zero, and A is some empirical loss rate. Solving this equation gives the form

$$N = N_0\exp(-AI_0t\cos^2\theta). \tag{7.2}$$

We see a fit to this equation in figure 7.2, with reasonable agreement to the data. We note that the beam powers were not fixed during this measurement as the control loop was saturated to give the highest power and load large atom numbers. Modelling the temperature of the cloud would be considerably more complex, but the lattice-heating mechanism could be examined by looking for a reduction in the effect when the power was controlled by a servo loop, or by shifting the frequency between the passes using an AOM to remove any interference patterns.

There are other mechanisms that could cause such loss, for example Lauber *et al.* [178] use a similar system and see the trapping laser pumping atoms from $F = 1 \rightarrow F = 2$. Detecting the $F = 2$ state independently would show if this hyperfine-changing mechanism were responsible. As we image on the $F = 2 \rightarrow F = 3$ cooling transition, this would be quite easy to implement in our system by leaving the repump beams off during imaging. This would mean any $F = 1$ atoms are not moved to $F = 2$, and the imaging would detect only the atoms already in $F = 2$.

This trapping potential is no longer in use. If it were reinstalled, particularly for use with ^{85}Rb, determining the mechanism of this loss would be crucial. Despite these problems, attempts to transfer atoms to the old 1550 nm trap, using the 1064 nm trap as a loading reservoir, tentatively showed higher numbers and phase-space densities in ^{87}Rb than were possible with the original smaller potential, suggesting that larger, denser two-species and molecular samples might be possible. At this moment, we are not pursuing this route.

7.4 Combination lattice / trap design

For the second iteration of this 1064 nm trap, we wanted the option to turn the 3D harmonic potential into a 1D lattice. Since lattice potentials are formed from the interference of two beams, it was necessary to switch to a single mode, narrow-linewidth laser. This also has the advantage of removing the fast loss we saw in section 7.3. As a tradeoff, we have less power available, so the beam must be focussed to a smaller waist to reach useful trap depths.

The new trap uses a commercial Nd:YAG non-planar ring oscillator, the Innolight Mephisto (now sold by Coherent inc.). This uses a single Nd:YAG crystal, shaped and coated so that the faces of the crystal form a lasing ring cavity. A magnetic field around the crystal causes Faraday rotation of the light around the ring cavity, and the output coupler coating on one crystal face has a slight polarisation sensitivity. This makes the laser operate in only one (circular) polarisation and in one direction round the ring cavity, which removes spatial hole burning [176]. It produces up to 2 W of CW 1064 nm light. The monolithic design, with the laser cavity contained entirely in the gain crystal, leads to a simple laser which is extremely insensitive to vibrations and air movement and has a free-running linewidth of ~ 1 kHz. In fact, the intrinsic stability of these lasers is so high that this exact model is used (with further stabilisation and mode cleaning) as the master laser for the Advanced LIGO gravitational wave detectors [179] which recently detected gravitational waves for the first time [180].

The optical layout to generate the light for the bowtie lattice is shown in figure 7.3. The output of the NPRO laser is elliptically polarised, so it is corrected to linear with a $\lambda/4$ waveplate, before passing through an optical isolator. A pair of lenses collimate and resize the beam, and two $\lambda/2$ waveplates and polarising beam split-

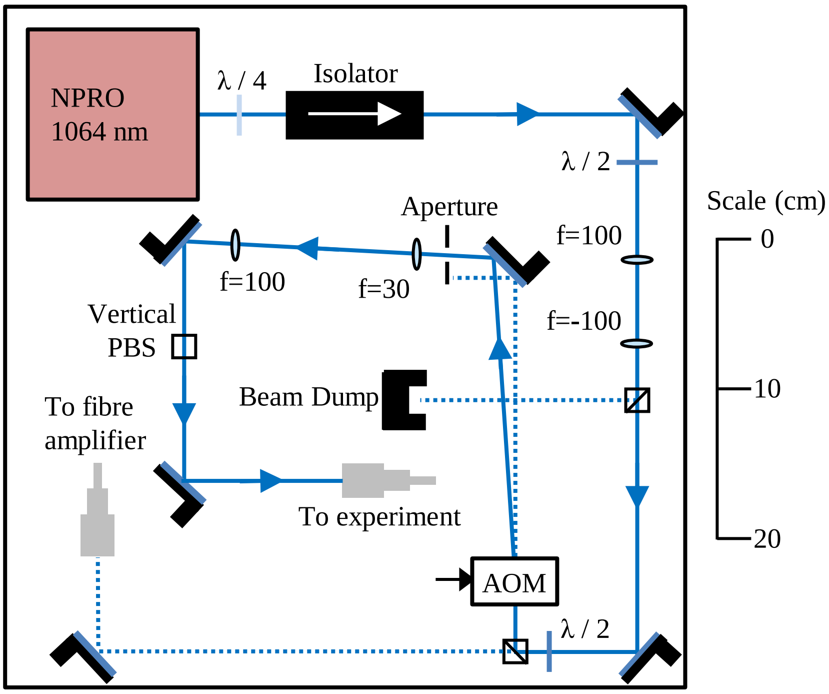

Figure 7.3: Optical layout to derive light for the lattice. The master laser is a narrow-linewidth commercial non-planar ring oscillator at 1064 nm. The system provides 0.5 W of 1064 light through a polarisation-maintaining fibre, with an AOM for analog intensity control. A spare beam is available to pass to a 30 W fibre amplifier for future experiments.

ters (PBS) allow us to adjust the power sent to the experiment. Up to 90% of the light is diffracted into the negative first order of an AOM (Isomet M1080-T80L at 80 MHz) which allows us to vary the power continuously. A vertical PBS then purifies the polarisation before the light is injected into a polarisation-maintaining fibre (Thorlabs P3-1064PM-FC-2) with $> 80\%$ efficiency and sent to the main experiment. We can couple up to 0.5 W of light out of the fibre, limited by the damage thresholds of the fibre end faces.

The optics to shape the light into the trapping potential are shown in figure 7.1. The fibre coupling cleans the mode and turns pointing stabilities into power fluctuations which can be actively stabilised. The output from this fibre is larger than from the original fibre laser, so the $f = 400$ mm lens now focuses the beams to a 96 μm waist. However, the divergence of the beam is different, so the focuses are not aligned axially with the position of the trap. As in the large reservoir trap, the beams intersect at $2\theta = 14^\circ$. This gives a lattice spacing a of

$$a = \frac{\lambda}{2\cos\theta} = 536 \text{ nm}. \tag{7.3}$$

7.4.1 Intensity control

We actively control the power of the beams using a feedback loop. The leaked light transmitted through the final mirror before the vacuum chamber is focused onto a photodiode (PD) and the signal sent through an integral feedback circuit to the amplitude modulation voltage on the fixed-frequency driver for the AOM before the fibre. The photodiode is after the fibre and a polarising cube, so the servo loop stabilises the trapping beams against power fluctuations caused by polarisation drifts. The system can control the power over a wide dynamic range, remaining linear from the full power of ~ 0.5 W down to 100 μW. We also include a mirror on a motorised flipper mount to divert all the power to a beam dump. This means the AOM can stay on at full power for most of the experimental sequence, staying warm and reducing fluctuations in efficiency from thermal effects. Typically the AOM switches off and the flipper mirror moves out of the beam around 1 s before the trap needs to switch on.

In section 7.5.3 we calibrate the lattice depth using short (~ 1 μs) pulses. Unfortunately the bandwidth of our servo limits our switching times to ~ 30 μs. To make shorter pulses, we bypass the servo with a high-speed switch (DG419), to send a fixed voltage from a power supply to the AOM. The pulse length is then limited in principle by the AOM switching time of 200 ns, and in practice by the 0.9 μs update rate of the FPGA control system (see section 1.5.4). Because the power is not servoed during the pulse, this method implicitly relies on the stability of the AOM and fibre alignment to produce consistent pulses across many experimental runs. We therefore monitor the pulse length and intensity during the experimental sequence using a 15 MHz photodiode on the light leaked through the first mirror after the fibre. Over 40 experimental cycles taking roughly one hour, the pulse intensity varied with a standard deviation of 0.9%.

7.5 Calibration

If we wish to use the trap, and particularly if we want to calculate temperatures and phase-space densities, it is essential to know the trap vibrational frequencies f_{trap}. These can be calculated from the beam size and power and the atomic polarisability, as in [136]. However it is useful to measure them directly, to check that the trap is correctly aligned and performing as expected. For our system, there are three ways to calibrate the potential: parametric heating, direct observation of trap oscillations or Kapitza-Dirac diffraction from a lattice. In this work, we demonstrate the latter two.

In parametric heating, the intensity of the trap is modulated at some frequency f. When $f = 2f_{\text{trap}}$, the atoms are heated and lost from the trap [181]. This requires some prior expectation for the aspect ratio of the trap, as the method does not distinguish axial from radial modes. This is usually obvious from the beam geometry, or it can be estimated from simulations. It also requires careful choice of the atom temperatures and beam powers to get high-quality data.

The second method is to measure the trap frequencies directly, by offsetting the atoms from the trap centre and then watching them oscillate in the harmonic potential. Our trapping beams are 60 μm across, so these (harmonic) oscillations will be only a few µm, smaller than our imaging resolution. However, if we let the atoms oscillate for some time and then expand in time-of-flight for several ms, their oscillating momentum is mapped onto spatial coordinates, greatly increasing the apparent movement. This provides a very direct measurement of the trap frequency. However, this method cannot be applied easily to the high trapping frequencies and periodic traps of a lattice potential.

The final method is Kapitza-Dirac diffraction. Here we match the polarisations of the two beams to create a 1D lattice potential, and create a BEC to put all the atoms in a single, well-defined momentum state. If we pulse on the lattice for a short time, it acts a diffraction grating and excites part of the BEC to discrete non-zero momentum states, in integer multiples of $2\hbar k$, whose relative populations can be predicted numerically [182] and fitted to the lattice depth. However, this method can only determine the potential along the lattice direction. Also, since any misalignent between the beams reduces the intensity of the interference pattern, this method inherently relies on the two lattice beams being well-aligned.

7.5.1 Direct oscillations

We measure the trap frequencies directly by inducing oscillations in the trap. We load a sample of ^{87}Rb atoms into the magnetically levitated crossed trap, then turn off the magnetic levitation gradient for 2 ms, and switch it back on. This gives the atoms an impulse so they oscillate vertically at the trap frequency. We release the atoms from the trap and allow them to expand and fall for 20 ms before imaging them, which maps the velocity distribution onto the spatial coordinates. We fit the vertical position with the equation

$$y(t) = A\sin(2\pi f t + \phi)e^{-t/T}. \tag{7.4}$$

We see these oscillations in figure 7.4. The exponential decay $e^{-t/T}$ accounts empirically for damping of the oscillations, which is caused by anharmonicity of the potential. We include the phase ϕ because the method to induce the oscillations gives two consecutive impulses and so the start time for the oscillations is not well-known. In subsequent experiments we have ramped the magnetic levitation down

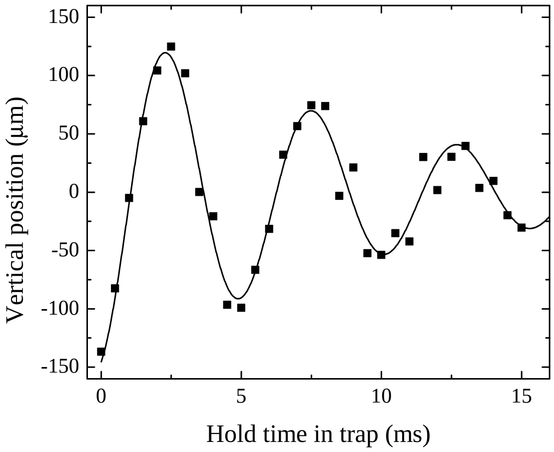

Figure 7.4: Vertical oscillations in the two-beam crossed optical trap at 1064 nm, after a 20 ms ballistic expansion to map velocity onto initial position. The solid line is a fit to equation 7.4, yielding a vertical trap frequency of $f_z = 192(2)$ Hz.

adiabatically, followed by a single sudden jump which gives a well-defined phase $\phi = 0$. The fitted vertical trap frequency is 192(2) Hz.

We can estimate the size of the trapping beams from these measured trap frequencies, using a numerical model of the optical and magnetic potential based on [136], which has been tested in several experiments using ^{87}Rb, ^{85}Rb and ^{133}Cs [77, 127]. We measure a vertical trapping frequency in a single-beam trap of 76(1) Hz at a power of 0.9 W. From this, we estimate the $1/e^2$ radius of the first beam as 110 µm. We then use the vertical frequency in the two-beam crossed trap (figure 7.4) to estimate the second beam waist as 72 µm. The difference between the two sizes is because the first focus is not aligned axially with the atomic sample.

7.5.2 Kapitza-Dirac diffraction theory

Here, we outline the numerical model we use for diffraction of a BEC from a lattice, based on calculations of the band-structure in a sinusoidal periodic lattice. We note that some groups approximate the momentum state populations analytically using Bessel functions [183, 184]. This approximation is only valid in the Raman-Nath regime where atomic motion during the interaction with the lattice is negligible, here meaning the pulses are shorter than a few µs [185]. Despite this, these approximate models have been used effectively in several BEC lattice experiments [183, 186, 187]. However, the full band-structure calculations provide a more complete description which covers all regimes, and they are sufficiently tractable that they can be solved on a desktop computer. They also predict the diffraction patterns correctly over much longer times and thus can give more precise calibrations. This theory is outlined in [182] and discussed in detail in [188, 189].

We consider our lattice as a periodic potential:

$$V(x) = V_0 \cos^2(kx) \tag{7.5}$$

where V_0 is the lattice depth and, for counterpropagating beams, $k = 2\pi/\lambda$ and the lattice period is $a = \lambda/2$. We rescale the energy in terms of the recoil energy $E_r = \hbar^2 k^2/2m$, using $V_0 = sE_r$ and $E = \epsilon E_r$. We treat the lattice beams as plane waves and do not consider the harmonic confinement from the Gaussian profile of the beam. From here, we can write the time-independent Schrödinger equation

$$-\frac{1}{k^2}\frac{d^2\psi(x)}{dx^2} + s\cos^2(kx)\psi(x) = \epsilon\psi(x). \tag{7.6}$$

To solve this, we start with Bloch's theorem [190] that the eigenfunctions of any periodic potential can be written as

$$\psi_{n,q}(x) = e^{iqx/\hbar} \cdot u_{n,q}(x), \tag{7.7}$$

a product of a plane wave $e^{iqx/\hbar}$ and a function $u_{n,q}(x)$ which has the same periodicity as the lattice. Here n is the band index, an ordering of solutions by increasing energy, which exists for all values of the quasimomentum q. We put this ansatz into equation 7.6 to get an equation for $u_{n,q}(x)$,

$$-\frac{1}{k^2}\left[-\frac{q^2}{\hbar^2} + \frac{2iq}{\hbar}\frac{d}{dx} + \frac{d^2}{dx^2}\right]u_{n,q}(x) + s\cos^2(kx)u_{n,q}(x) = \epsilon_{n,q}u_{n,q}(x). \tag{7.8}$$

Since $u_{n,q}(x)$ has the same periodicity as the lattice, we can expand the periodic function $u_{n,q}(x)$ as a Fourier series:

$$u_{n,q}(x) = \sum_{l=-\infty}^{\infty} c_{l,n,q} e^{i2lkx}. \tag{7.9}$$

This means the Bloch wavefunctions are

$$\psi_{n,q}(x) = \sum_{l=-\infty}^{\infty} c_{l,n,q} e^{ix(2lk+q/\hbar)} = \sum_{l=-\infty}^{\infty} c_{l,n,q} \left|\phi_{2\hbar lk+q}\right\rangle \tag{7.10}$$

which we note has momentum $2l\hbar k + q$. If we insert 7.9 into 7.8 and compare terms with the same e^{i2lkx} term, we get a Hamiltonian which can be written in matrix form:

$$\sum_{l=-\infty}^{\infty} H_{l,l'} \cdot c_{l,n,q} = \epsilon_{n,q} c_{l,n,q} \tag{7.11}$$

where

$$H_{l,l'} = \begin{cases} \left(2l + \frac{q}{\hbar k}\right)^2 + \frac{s}{2} & \text{if } l = l' \\ -s/4 & \text{if } |l - l'| = 1 \\ 0 & \text{otherwise} \end{cases} . \tag{7.12}$$

We can solve this system of equations, for some finite range of l, to find the eigenenergies and eigenstates of the lattice. In general, each eigenstate is some linear combination of momentum states l with energy $\epsilon_{n,q}$.

To calibrate our lattice, we consider the case of non-adiabatic loading, where the lattice is switched on suddenly, and off some time t later. We consider the BEC as a plane wave, $|\phi_q\rangle = e^{iqx/\hbar}$ with momentum q. If we suddenly switch on the lattice, this state is projected onto the Bloch states $|n, q\rangle = \psi_{n,q}(x)$:

$$|\Psi(t = 0)\rangle = \sum_{n=0}^{\infty} |\Psi_n(t = 0)\rangle = \sum_{n=0}^{\infty} |n, q\rangle \langle n, q|\phi_q\rangle . \tag{7.13}$$

We can use equation 7.10 to find $\langle n, q|\phi_q\rangle$:

$$\langle n, q|\phi_q\rangle = \sum_{l=-\infty}^{\infty} c^*_{l,n,q} \langle \phi_{2\hbar kl+q}|\phi_q\rangle = c^*_{0,n,q}. \tag{7.14}$$

We can then evolve each eigenstate in time according to the energies we calculate from 7.11:

$$\begin{aligned} |\Psi_n(t)\rangle &= |\Psi_n(t = 0)\rangle\, e^{-i\epsilon_{n,q}\hbar k^2 t/2m} && (7.15) \\ &= c^*_{0,n,q} |n, q\rangle\, e^{-i\epsilon_{n,q}\hbar k^2 t/2m}. && (7.16) \end{aligned}$$

When we switch the lattice off at some time t, the states are projected back onto the plane-wave basis:

$$\begin{aligned} |\Psi_n(t)\rangle &= \sum_{n=0}^{\infty} c^*_{0,n,q} c_{l,n,q} e^{-i\epsilon_{n,q}\hbar k^2 t/2m} |\phi_{2\hbar kl+q}\rangle && (7.17) \\ &\equiv \sum_{n=0}^{\infty} b_{l,n,q} |\phi_{2\hbar kl+q}\rangle . && (7.18) \end{aligned}$$

The $b_{l,n,q}$ coefficients give the fractional population in each band and momentum state, and are known from diagonalising equation 7.12. However, in a typical lattice experiment, we resolve the momentum distribution of the atoms by allowing the BEC to expand in time-of-flight. This means we can resolve the different momentum states l, but we have no way to distinguish the bands n and must take the total population in all bands, even though in principle our model can produce the population in each. The population with momentum $2l\hbar k$ is then given by

$$P(l) = \left| \sum_{n=0}^{\infty} b_{l,n,q} \right|^2 \tag{7.19}$$

We can understand the complicated time-dependence of the populations intuitively as interference between the bands, whose phases evolve sinusoidally at different rates according to equation 7.16, giving an increasingly complex structure as more bands and momentum states are populated and start to interfere.

In practical terms, we build this model using Python, with the SciPy package which has libraries for linear algebra and matrix manipulation [191]. The lattice spacing and atomic mass are fixed and the experimental populations in each momentum state l at an arbitrary series of times are read from a .csv file. We fit two parameters: the total atom number N and the dimensionless lattice depth s (recall $V_0 = sE_R$ is the lattice depth), using a nonlinear least-squares fit. All momentum states are fitted simultaneously, with positive and negative states treated independently. In our system we have a static lattice and BEC, meaning $q = 0$ and the populations in positive and negative l states are identical, but in general this is not true if the lattice beams are detuned and the lattice potential moves, or if the BEC has some initial momentum. The program could easily be adapted to fit data where $q \neq 0$. A fit to a typical data series, such as those shown in figure 7.6, takes a few seconds on a normal desktop computer[2].

We calculate the statistical uncertainty on the fitted s and N from the diagonal elements of the covariance matrix of the fit, scaled to the residual variance and divided by the degrees of freedom in the fit. This assumes all the datapoints have identical uncertainties, which in some cases may not be true. In cases such as figure 7.6 where the fit is good, this is a valid method. When the simulation is

---

[2] Intel i3-3220 CPU @ 3.3GHz, 4GB RAM for all simulations presented here.

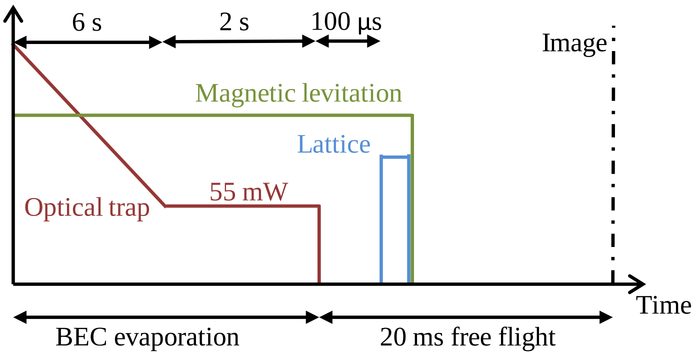

Figure 7.5: Sketch of the experimental sequence for Kapitza-Dirac diffraction (not to scale). A BEC is released from the optical trap and exposed to a short pulse of the lattice potential. 20 ms of free flight separates the discrete momentum states for imaging and detection.

not a good fit to the data, scaling by the residual variance is no longer a valid statistical method to determine the errors on s and N. This could be examined more thoroughly by repeating each pulse length several times to give error bars on each point, and weighting the fit accordingly, with minimal changes to the code. However the large amount of experimental data needed to create statistically significant error bars on such a complex set of data mean this is not practical.

7.5.3 Kapitza-Dirac diffraction Results

To demonstrate Kapitza-Dirac diffraction, we first create a BEC of ^{87}Rb in the 1550 nm trap by loading a levitated optical trap as normal with the atoms in the $|F = 1, m_F = 1\rangle$ state, ramping both beams down to 55 mW in 6 s and holding at this power for 2 s to let the atoms reach equilibrium. This makes a BEC of 2×10^5 atoms with no measureable thermal fraction, enough for this measurement. We can make much larger BECs of $\sim 1 \times 10^6$ atoms [95], but the long MOT loading times needed for this would make the measurement tedious, and the smaller BECs were enough to get high-quality data. We detune the imaging beam from resonance by 6.10(7) MHz, reducing the optical density of the BEC by $5\times$. This means the dense atomic samples do not absorb all the probe light and thus ensures the atom numbers are accurate.

We turn off the trapping beams, leaving the magnetic gradient on to levitate the atoms and, after 100 μs, pulse the lattice at a fixed power as explained in section 7.4.1. The minimum pulse length is 0.9 μs from the time resolution of our FPGA control system. We switch off the levitation gradient and let the BEC expand and fall for 20 ms, completely separating the $2l\hbar k$ momentum states before imaging. Typical images of the separated momentum states are shown in figure 7.6(c).

We measure the number of atoms in each momentum state, and normalise them to the total number in each shot with a global fit to all the momentum states, by summing along the vertical lines of pixels in figure 7.6(c). We observe some s-wave scattering between the momentum states which removes the some of the atoms from the momentum wavepackets and creates a spherical shell of scattered atoms, as described in [192–194]. This shell forms a flat background on the fits to the individual cloud numbers, but only covers some of the momentum states and thus cannot be removed from the fit to the total number. This means the total number is overestimated by a few percent compared to the sum of the individual clouds. We therefore include the total number as a free parameter in the model, and renormalise the data to the fitted total population for clarity.

In figure 7.6, we see that the model gives an excellent fit to the momentum state populations. For figure 7.6(a) we use a lattice power of 0.131 W and fit $s = 45.7(1)$, giving $V_0 = 4.19(1)$ μK. In figure 7.6(b), $P = 0.488$ W and we fit $s = 203(1)$, $V_0 = 18.6(1)$ μK. We see small deviations from the model which increase at later times, which are probably from dephasing due to the Gaussian profile of the lattice beams, which would cause a varying lattice depth across the BEC. However, the model is clearly a good description of the diffraction.

We can compare the fitted depths to numerical simulations based on the intensity and atomic polarisability. We use the beam sizes estimated from the direct measurements of the radial trapping frequencies in section 7.5.1. This predicts $V_0 = 3.42$ μK for figure 7.6(a) and $V_0 = 13.35$ μK for figure 7.6(b), compared to 4.19(1) μK and 18.6(1) μK measured with Kapitza-Dirac diffraction. The substantial discrepancy between these is most probably from poor knowledge of the beam sizes, which in the early setup were not precisely aligned in the axial direction.

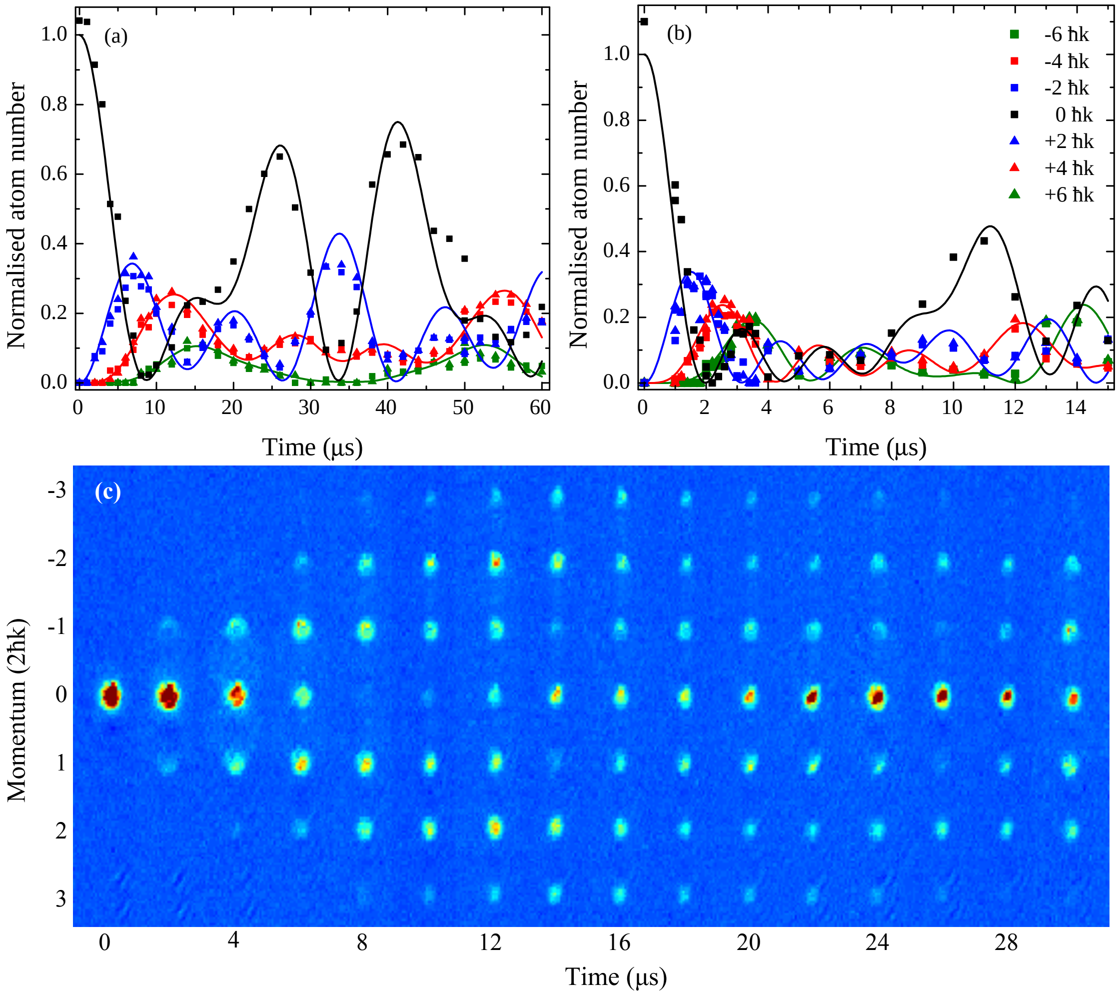

Figure 7.6: Kapitza-Dirac diffraction of a BEC from a 1D lattice. (a): $V_0 = 45.7(1)E_R$ using 0.13 W. (b): $V_0 = 203(1)E_R$ using 0.49 W. In (b), higher momentum orders up to $l = 7$ are omitted for clarity. Note all the curves in each graph are fitted to two free parameters, the total atom number N_0 and the lattice depth s. (c): Diffracting BECs with varying pulse length, showing the clear separation of the discrete momentum states. These are the same data as graph (a). Each image shows roughly $1.5 \times 0.2\ \text{mm}^2$ and has been rotated by 90° so the lattice axis is shown vertically.

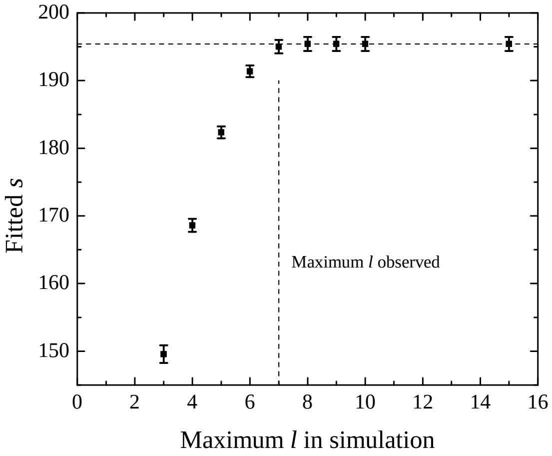

Figure 7.7: Fitted s for the data in figure 7.6(b), varying the highest momentum state $|2l\hbar k\rangle$ in the simulation. We see the fitted value does not change significantly when we include all the momentum states observed in the diffraction patterns.

7.5.4 Maximum L in simulation

In the Kapitza-Dirac theory in section 7.5.2, and in [188], we see that the oscillations in the momentum-state populations could be understood as interference between the different eigenstates (bands). In principle, all momentum states contribute to this interference. However, if a band or momentum state is not populated, the effect of the interference will be small and it will not affect the population. It is therefore useful to establish how many momentum states we must include to give an accurate picture of the diffraction. We test this using the experimental data from figure 7.6(b), and fitting a value for s using a limited range $-l_{\mathrm{max}} < l < l_{\mathrm{max}}$, as shown in figure 7.7. We note that in this data the largest momentum state we could detect was $\pm 14\hbar k$ $(l = 7)$. When we increase from $l_{max} = 7 \rightarrow 8$, the fitted value changes by less than the statistical error. By $l_{max} = 9 \rightarrow 10$, the relative change is $\Delta s = 3 \times 10^{-6}$. From this we conclude that we only need to include a few states above the largest l observed. For the fits in figure 7.6 we include $|l| \leq 15$.

7.5.5 Polarisation alignment

Our trap design allows us to switch between a simple harmonic potential and a 1D lattice, just by rotating the waveplate between the two beams. By making the polarisation orthogonal, we remove the interference between the beams and thus the lattice. We can use the Kapitza-Dirac diffraction to find the polarisation angle where there is no interference. This could be done dynamically during an experimental run using variable waveplates or motorised rotation mounts if needed, though we have not currently implemented this. To ensure the polarisations are orthogonal, we produce diffraction peaks as in section 7.5.3, using a 1 µs pulse of lattice light at $\sim$ 0.5W, populating the $\pm 2\hbar k$ and $\pm 4\hbar k$ momentum states. We rotate the waveplate until all the diffraction peaks disappear, and we can set the angle between the beam polarisations to better than ±1°. When setting the polarisation to maximise the lattice, one could search for the point where the diffraction into higher momentum states is maximised, but we find it is more precise to find the minimum and rotate the waveplate by exactly 45°.

7.6 Loading molecules into a lattice

Here we demonstrate loading Feshbach molecules into a lattice potential, as a proof of principle. We hope in future to transfer such molecules to the ground state using STIRAP, as demonstrated in the 1550 nm trap in chapter 5, and use the lattice potential to achieve higher molecular densities.

The 1550 nm optical trap and 1064 nm lattice potentials are very different shapes, with lattice trap frequencies $\sim$ 60 kHz, making it difficult to transfer the molecules adiabatically. We therefore use a very fast transfer. From a levitated sample of Feshbach molecules in the $|-2\rangle$ state, we switch the 1550 nm trap off and switch the lattice potential on to 440 mW per beam. We measure the molecular lifetime in the lattice potential in figure 7.8.

We see a fast drop in the molecule number immediately after loading the lattice in 13(4) ms, followed by a 0.4(1) s slow decay. The initial fast loss may be caused by thermalisation in the new potential, followed by slow loss from molecular collisions

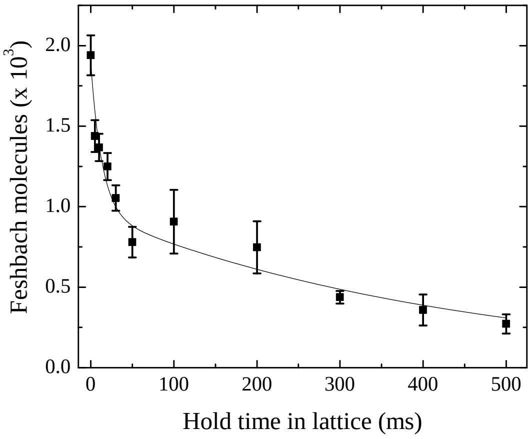

Figure 7.8: Lifetime of a sample of Feshbach molecules in a 1D lattice. The solid line shows a double exponential with decay times of 13(4) ms and 0.4(1) s

and seen in the conventional trap - the slow decay time is consistent with the decay time we measure in a 1064 nm harmonic trap in figure 7.9. It is likely that further optimisation of the transfer to the lattice would reduce this thermalisation and give larger samples in the lattice. One might expect the decay rate to drop when only one molecule remains in each lattice sheet, but since the molecular cloud radius is ~ 6 µm along the lattice axis, and occupies only around 200-300 lattice sheets, this cannot explain the slow decay which starts at around 1000 molecules.

7.7 Loading molecules into a 1064nm 3D trap

To create molecules in the 1064 nm trap, we might first load an atomic mixture that has been precooled in the 1550 nm trap and then create the molecular sample by magnetoassociation. However, this is problematic because the magnetoassociation efficiency is critically dependent on the phase-space density (PSD) [67]. Transferring between the traps will inevitably heat the atoms. While an adiabatic transfer would not decrease the PSD, the loss of molecules would decrease the PSD, which would reduce the association efficiency. Also, Cs atoms have high 3-body loss rates, so the time taken to transfer between the traps would reduce

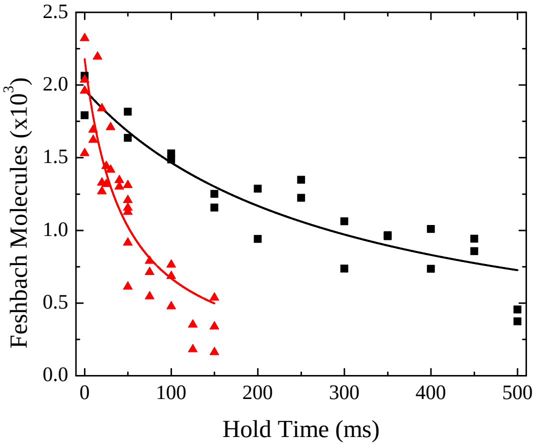

Figure 7.9: Lifetime of Feshbach molecules in the 1064 nm trap. We compare the lifetimes in the $|-2(1,3)d(0,3)\rangle$ (black) and $|-6(2,4)d(2,4)\rangle$ (red) states. Fitting a two-body loss model gives decay rates of $L_2 = 2.5(5) \times 10^{-10}$ cm^3/s and $L_2 = 1.5(3) \times 10^{-9}$ cm^3/s.

the Cs number further [77]. We therefore choose to load the 1064 nm trap after the magnetoassociation to maximise the molecule numbers after loading.

When loading the molecules into a 1064 nm harmonic trap, we used a slightly different trap geometry. We added a telescope after the fibre in figure 7.1, decreasing the size of both trapping beam focuses to 60(4) µm and positioning the beam waist precisely at the atomic cloud. This increased the maximum depth of the trap and gave a more symmetric harmonic potential.

We start with a sample of molecules in the $|-2(1,3)d(0,3)\rangle$ Feshbach state, held in the magnetically levitated 1550 nm optical trap at 200 mW. We ramp up the 1064 nm trap up to 400 mW in 175 ms, adiabatically heating the sample. Once the 1064 nm trap is at maximum power, it dominates the potential from the 1550 nm trap and magnetic levitation gradient, so these are turned off simultaneously in 10 ms without significantly heating the sample. This leaves around 2000 molecules in a pure 1064 nm trap. Because of the shallow angle between the two 1064 nm beams, the new potential is much longer, decreasing the molecular density.

In figure 7.9, we estimate the lifetime of the molecules in the $|-2(1,3)d(0,3)\rangle$ and $|-6(2,4)d(2,4)\rangle$ Feshbach states as 0.46(5) s and 75(8) ms respectively. For the latter, we transfer the molecules to the 1064 nm trap as before, and then increase the magnetic field to 181.6 G.

A more robust comparison uses a two-body decay model [79]. We assume a Gaussian spatial distribution, and that the sample remains in (quasi)thermal equilibrium at a temperature T. The rate equation for the density of the ground-state molecules n is then

$$\frac{dn}{dt} = -L_2 n^2. \tag{7.20}$$

We introduce the effective volume

$$V_{\text{eff}} = \left(\frac{4\pi k_B T}{m\bar{\omega}^2}\right)^{3/2}, \tag{7.21}$$

where

$$\bar{\omega} = (\omega_x \omega_y \omega_z)^{1/3} \tag{7.22}$$

is the geometric mean trapping frequency. This allows us to rewrite equation 7.20 using the total atom number

$$\frac{dN}{dt} = -\frac{L_2}{V_{\text{eff}}} N^2. \tag{7.23}$$

This has an analytic solution of the form

$$N = \frac{1}{Ct + D}, \tag{7.24}$$

where $C = L_2/V_{\text{eff}}$ is the loss rate and $N_0 = 1/D$ is the initial number. Figure 7.9 shows fits with this function, and we calculate $L_2 = 2.5(5) \times 10^{-10}$ cm^3/s and $L_2 = 1.5(3) \times 10^{-9}$ cm^3/s for the $|{-2}(1,3)d(0,3)\rangle$ and $|{-6}(2,4)d(2,4)\rangle$ states respectively. We note that the loss rate is considerably higher for the $|{-6}(2,4)d(2,4)\rangle$ state. A similar analysis for the $|{-6}(2,4)d(2,4)\rangle$ state in the 1550 nm trap (figure 1.4) gives $L_2 = 1.8(4) \times 10^{-9}$ cm^3/s, consistent with the rate in the 1064 nm trap. This shows that the longer 75(8) ms lifetime in the 1064 nm trap (compared to 23(2) ms in the 1550 nm trap) is due to the higher temperature and lower trapping frequencies, which reduces the density and collision rate.

We measure the temperature of the dissociated molecules by time-of-flight (TOF) expansion. After they are dissociated into atoms, the trapping potential is suddenly turned off and they are allowed to expand and fall in free space. The width of the cloud expands as

$$\sigma^2 = \sigma_0^2 + \frac{k_{\text{B}} T}{m} t^2. \tag{7.25}$$

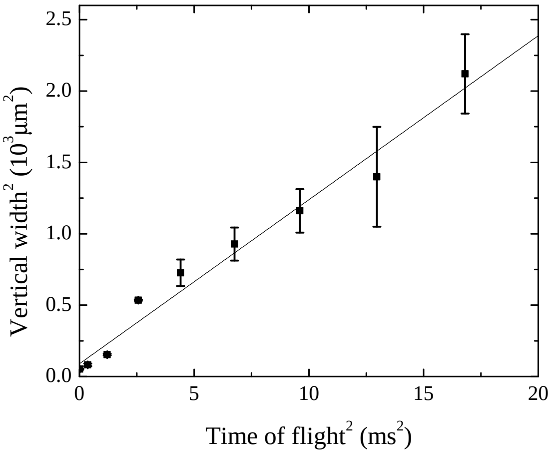

Figure 7.10: Determining the temperature of the Feshbach molecules in the 1064 nm trap. The molecules are dissociated into atoms, released from the trap and allowed to expand in free space. The size of the cloud of Cs atoms is measured after various expansion times. The solid line is a linear fit, which yields a temperature of 1.9(1) μK. The time of flight is limited by the small molecule number and low optical depth at long times.

We square the width and time of flight and make a linear fit, and calculate the temperature from the gradient $k_\mathrm{B}T/m$. This method is described in detail in [97].

Expansion of Feshbach molecules from the 1064 nm trap is shown in figure 7.10. For large atomic samples, the maximum possible TOF is the time for the atoms to fall out of the camera frame. For the molecules, the low numbers and long trapping potential mean the optical density of the cloud is only 0.1, and this reduces further as the molecules expand, so beyond 4 ms the cloud is too sparse to fit a reliable width. From the expansion rate we measure a temperature of 1.9(1) μK. The temperature is measured after the molecules are dissociated and we cannot rule out heating from the dissociation process, so we must take this measurement as an upper bound on the temperature.

Before the magnetoassociation, the atoms have a temperature of 300 nK. Most of the heating comes from the transfer of the molecules to the 1064 nm unlevitated trap, which has a much longer aspect ratio than the 1550 nm trap.

7.8 Conclusions

In this chapter, we have developed and characterised a new, versatile trapping potential at 1064 nm. We have found good agreement between theoretical calculations and measurements of the trap frequencies. We developed the models and techniques for calibrating lattices using Kapitza-Dirac diffraction, and found reasonable agreement with other measures of the trap parameters. We showed loading of Feshbach molecules into both a harmonic trap and a 1D lattice, with lifetimes in both traps remaining long enough for future experiments.

In chapter 5 we demonstrated well-understood and fully characterised STIRAP transfer, and we are now ready to attempt this in our new 1064 nm trapping potential. As 1064 nm is near the magic wavelength with equal polarisabilities for the Feshbach and ground state molecules (table 7.1), we expect the transfer to cause minimal heating and loss, leading to longer lifetimes and colder samples. This opens prospects for measuring the molecular polarisability and confirming theoretical models [135, 137], and for testing theories of ultracold molecular scattering and four-atom complex formation [6].

Chapter 8

Conclusions and outlook

The main result of this thesis is the creation and trapping of ^{87}RbCs molecules in the electronic, rovibrational and hyperfine ground state, at a temperature of 1 μK.

In chapter 3, we built a laser system to create continuously tunable light at two widely separated wavelengths with a linewidth of < 1 kHz. We measured the frequency stability with reference to a frequency comb, and developed a novel method to measure the free spectral range and finesse of the cavity, giving a well-calibrated relative frequency scale on a kHz level over several GHz.

In chapter 4, we demonstrated this laser system with one- and two-photon spectroscopy of ^{87}RbCs molecules. This allowed us to identify the rovibrational and hyperfine ground state, and make precision measurements of the rotational constant and permanent electric dipole moment.

In chapter 5 we transferred the molecules from a weakly-bound Feshbach state to the rovibrational ground state using STIRAP, and selectively populated multiple hyperfine states. A numerical model of the transfer process, including a Monte Carlo simulation of the laser linewidth, agreed excellently with experimental measurements. The molecules had a lifetime of 0.89(6) s in the optical trap, and could be detected for over 1.5 s.

In chapter 6 we referenced the lasers to a frequency comb, and made the most precise measurement of any molecular binding energy to date, with a fractional uncertainty of 4×10^{-10}.

v''	J''	Frequency (GHz)	Strength	v''	J''	Frequency (GHz)	Strength
0	0	306 831.02	1.000	3	0	302 403.62	41.30
0	2	306 828.08	1.000	3	2	302 400.68	41.30
1	0	305 348.69	7.511	4	0	300 940.87	37.02
1	2	305 345.78	7.513	4	2	300 937.96	37.01
2	0	303 872.90	24.11	5	0	299 484.72	11.82
2	2	303 869.97	24.11	5	2	299 481.81	11.81

Table 8.1: Predicted transition strengths and frequencies from the $|v' = 29, J' = 1\rangle$ level of the $A^1\Sigma^+ + b^3\Pi$ potential to the low-lying $X^1\Sigma^+$ rovibrational levels. The transition strengths are normalised to the $v'' = 0$, $J'' = 0$ transition which is used in this Thesis. Data from [122], based on [123].

Finally in chapter 7, we built a new optical potential using 1064 nm light, which we used to trap a sample of Feshbach molecules in a periodic lattice potential. This allowed us to develop and test the tools and methods to characterise such potentials, for use in future lattice experiments.

8.1 Outlook

8.1.1 Further measurements of molecular properties

There are still measurements that could be made to characterise the molecular structure of ^{87}RbCs further. For example, the low-lying vibrational structure has yet to be studied experimentally in detail. In this thesis we have only studied the $v'' = 0$ rovibrational level of the ground-state potential, and studies using Fourier transform spectroscopy resolve relatively few low-lying vibrational transition [88]. Predictions have been made for the positions and relative transition strengths of the higher levels [122, 123], and are shown in table 8.1. We are in a position to test these predictions directly and at high precision. The main limitation is the tuning range of our lasers. The Stokes laser can be tuned roughly between 330 THz and 304 THz. It should be possible to measure the position and strength of the transitions to the $v'' = 1$ states using the same intermediate state as in chapter 5.

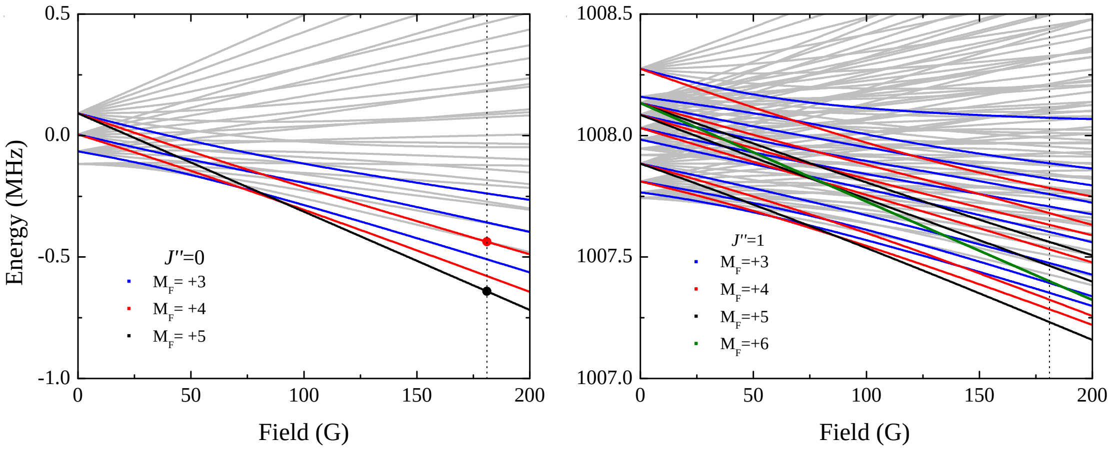

Figure 8.1: Hyperfine and Zeeman structure of the $X^1\Sigma^+$, $v'' = 0$, $J'' = 0, 1$ rovibrational states, calculated by Aldegunde *et al.* [126]. $J'' = 0$ (left): The highlighted lines are the $m_F = 3, 4, 5$ states which selection rules would allow to us populate with STIRAP. The dotted lines are the magnetic field at which we do the STIRAP transfer, and the dots show the states we have populated (see figure 6.5). $J'' = 1$ (right): Microwaves may allow us to transfer from the $J'' = 0$, $m_F = 4, 5$ states to the $J'' = 1$, $m_F = 3, 4, 5, 6$ states.

The $v'' = 2$ state lies at the edge of the range of our Stokes laser if we use the same $v' = 29$ pump transition, so the available power is limited. However, the transition strength is predicted to be 25× larger so the power available should be sufficient despite this. Identifying a different intermediate state at a higher pump frequency, which also has suitably strong transitions to the ground and Feshbach states, would allow us to reach higher vibrational levels.

Another prospective measurement is to increase the precision of the rotational constant, B_0, of the ground state. Our measurement of B_0 is currently limited by the unresolved hyperfine structure of the $J'' = 2$ state. A measurement of the Stokes transition using STIRAP transfer to the $J'' = 2$ state, as we have done for $J'' = 0$ in figure 6.5, would allow us to identify the hyperfine states.

The rotational and hyperfine structure of the ground state could be determined more accurately using microwave spectroscopy. Driving $J'' = 0 \rightarrow J'' = 1$ transitions would let us identify a larger number of hyperfine states in $J'' = 1$, which could be fitted with the hyperfine structure models in figure 8.1. This would give accurate measures of the rotational constant B_0 and the various nuclear properties and coupling constants, which can be compared with calculations from density functional theory [126]. In KRb, and NaK, π-pulses were used to populate $J'' = 1$, and then a second photon was used to reach many hyperfine states in $J'' = 0$ [195, 196]. The same method should be possible in ^{87}RbCs. Driving a $\pi/2$-pulse can also put the molecules in a superposition of $1/\sqrt{2}\left(|J''=0\rangle + |J''=1\rangle\right)$, which has a non-zero electric dipole moment in the laboratory frame with no external electric field, unlike the pure $|J''=0\rangle$ state [26].

Our binding energy measurement in chapter 6 is limited by the precision to which the binding energy of the Feshbach state is known, and this is taken from coupled channel calculations [66]. If these binding energies could be measured more precisely, for example by RF spectroscopy on an atomic mixture, the binding energy uncertainty could be improved. Measurement and confirmation of the hyperfine structure models in the molecular ground state would also improve the accuracy of the binding energy. However, the latest theoretical predictions of the binding energy [152] are far less precise than our current measurement, so it is not clear what would be gained from the extra precision.

It has been proposed [167] that precision spectroscopy of certain molecules could be used to make sensitive measurements of the variation of fundamental constants, particularly the electron-proton mass ratio [7, 168, 169] and the fine-structure constant [7, 170]. Previous studies have focused on microwave transitions [170, 171] and high-lying vibrational states [172–174]. Using an optical frequency comb reference, the high precision afforded by measurements on ultracold molecules can in principle be extended to arbitrary vibrational states. The demonstration that molecular transitions in the optical domain can be measured with fractional uncertainties below 10^{-10} represents an important step toward measuring the variation of fundamental constants in ultracold molecules.

8.1.2 Physics with dipolar molecules

One prediction of the dynamic properties of a bulk sample of molecules in a harmonic trap is the effect of loss by “sticky collisions” [6]. This involves formation of long-lived, weakly-bound two-molecule complexes which are susceptible to losses from collisions with unbound molecules. These processes can be modelled numerically with simple rate equations, and the rates have been predicted using multichannel quantum defect theory. It may be possible to observe these loss rates, and their predicted change with electric field, if the technical problems with observing molecule loss at high electric fields can be solved.

A possible alternative method is to remove the unbound molecules with the Stokes laser once the complexes have formed. This mechanism should then cause the complexes to dissociate, so some unbound molecules "reappear". This can be interpreted as an equilibrium reaction, where we disturb the system by removing the product species and then allowing the reaction to return to equilibrium.

This model is only applicable to non-reactive molecules such as ^{87}RbCs, while for reactive species such as KRb the predicted loss rates are dominated by reactive collisions [6]. ^{87}RbCs offers a potential for comparison between reactive and non-reactive species, by populating the $v'' = 1$ vibrational level. The single quanta of vibrational energy is enough to make the molecule reactive and drastically change the collision dynamics.

The two-body, three-body and complex formation mechanisms all make predictions about the changing number of molecules. For example, the three body loss rate γ is related to the more general 3-body loss coefficient L_3 by

$$\gamma = L_3 \left(\frac{m\omega^2}{2\pi k_\mathrm{B}} \right)^3 . \tag{8.1}$$

We see that the loss rate γ depends on the geometric mean trapping frequency ω. This can be simulated [136] as for atomic samples, but we need to know the dynamic polarisability of the molecules at the trapping wavelength (1550 nm in this case). The lifetime of our ground state molecular sample is 0.89(6) s, which should be long enough to measure the trapping frequencies in the optical potential by parametric heating. Comparisons with atomic samples under identical conditions for which the polarisabilities are well-known [177] would allow us to measure the polarisability of the molecule. This would confirm theoretical predictions of these values ([137], based on [197]. See table 7.1).

All these processes are more easily visible at higher molecular densities. Ideally, we would increase the ground-state molecule number, which would simultaneously increase our signal-to-noise ratio for the lifetime measurements. Further improvements to the STIRAP transfer may be possible, for example by synchronising the transfer to the 50 Hz mains frequency to reduce shot-to-shot magnetic field noise. However, the current transfer efficiency is 88%, so the effect of this would be marginal. Our previous work has shown 5000 Feshbach molecules can be created if the system is carefully optimised [67], which would give an increase by a factor of 2. Any further improvement above this would likely be from larger, denser atomic samples, leading to better Feshbach association efficiency. The reservoir trap described in section 7.3 could improve this substantially, however reimplementing it would be a considerable effort.

A more effective way to improve the density would be to compress the molecules into a smaller trap, such as the lattice potential described in section 7.4. We are currently redesigning the lattice potential to make the trapping beams intersect at a wider angle, to give a less elongated trap. This will increase the lattice site spacing, but only by roughly 10%. It will also let us retroreflect each beam, to give a 2D lattice which would further increase the density.

8.2 New magnetic transport setup

Eventually we would like to load the molecules into a 3D lattice, to study spin-lattice models [26] and quantum many-body dynamics [27]. However, the optical access in our experiment is severely limited by the twelve MOT beams, and installing a 3D lattice would be extremely difficult. Also, the rubidium dispensers in our vacuum chamber have been operating for many years and are likely nearly empty. We are therefore planning a new vacuum chamber and experiment, which will combine the best features of the RbCs experiment with the magnetic transport technique developed for our neighbouring ^{85}Rb BEC experiment [127, 198]. By moving the atoms away from the MOT chamber, we will gain the optical access needed to build a 3D lattice, image the atoms and molecules along several orthogonal axes, and potentially add a quantum gas microscope for single-site imaging of the lattice [199].

8.3 Concluding remarks

By creating a sample of ultracold polar molecules, we have achieved the original long-term goal of the Durham Rb-Cs project as it was laid out over ten years ago. However, this does not mean the research project is finished. In fact, this is arguably where the most interesting physics starts! Ultracold molecular physics is a fascinating and almost unexplored field which promises to grow and mature in coming years. Being in the vanguard of this exhilarating advance offers many possible directions for the experiment and an exciting new era for ultracold physics.

Bibliography

[1] L. D. Carr, D. DeMille, R. V. Krems, and J. Ye, *Cold and ultracold molecules: science, technology and applications*, New J. Phys. **11**, 055049 (2009).

[2] D. S. Jin and J. Ye, *Introduction to Ultracold Molecules: New Frontiers in Quantum and Chemical Physics*, Chem. Rev. **112**, 4801 (2012).

[3] M. Lemeshko, R. V. Krems, J. M. Doyle, and S. Kais, *Manipulation of molecules with electromagnetic fields*, Mol. Phys. **111**, 1648 (2013).

[4] S. Ospelkaus *et al.*, *Quantum-State Controlled Chemical Reactions of Ultracold Potassium-Rubidium Molecules*, Science **327**, 853 (2010).

[5] R. V. Krems, *Cold controlled chemistry*, Phys. Chem. Chem. Phys. **10**, 4079 (2008).

[6] M. Mayle, G. Quéméner, B. P. Ruzic, and J. L. Bohn, *Scattering of ultracold molecules in the highly resonant regime*, Phys. Rev. A **87**, 012709 (2013).

[7] V. V. Flambaum and M. G. Kozlov, *Enhanced Sensitivity to the Time Variation of the Fine-Structure Constant and m_p/m_e in Diatomic Molecules*, Phys. Rev. Lett. **99**, 150801 (2007).

[8] T. A. Isaev, S. Hoekstra, and R. Berger, *Laser-cooled RaF as a promising candidate to measure molecular parity violation*, Phys. Rev. A **82**, 052521 (2010).

[9] J. J. Hudson *et al.*, *Improved measurement of the shape of the electron*, Nature **473**, 493 (2011).

[10] D. DeMille, *Quantum Computation with Trapped Polar Molecules*, Phys. Rev. Lett. **88**, 067901 (2002).

[11] L. Santos, G. V. Shlyapnikov, P. Zoller, and M. Lewenstein, *Bose-Einstein Condensation in Trapped Dipolar Gases*, Phys. Rev. Lett. **85**, 1791 (2000).

[12] M. A. Baranov, M. Dalmonte, G. Pupillo, and P. Zoller, *Condensed Matter Theory of Dipolar Quantum Gases*, Chem. Rev. **112**, 5012 (2012).

[13] J. F. Barry, D. J. McCarron, E. B. Norrgard, M. H. Steinecker, and D. DeMille, *Magneto-optical trapping of a diatomic molecule*, Nature **512**, 286 (2014).

[14] D. J. McCarron, E. B. Norrgard, M. H. Steinecker, and D. DeMille, *Improved magnetooptical trapping of a diatomic molecule*, New J. Phys. **17**, 035014 (2015).

[15] E. B. Norrgard, D. J. McCarron, M. H. Steinecker, M. R. Tarbutt, and D. DeMille, *Submillikelvin Dipolar Molecules in a Radio-Frequency Magneto-Optical Trap*, Phys. Rev. Lett. **116**, 063004 (2016).

[16] V. Zhelyazkova *et al.*, *Laser cooling and slowing of CaF molecules*, Phys. Rev. A **89**, 053416 (2014).

[17] R. Glöckner, A. Prehn, B. G. U. Englert, G. Rempe, and M. Zeppenfeld, *Rotational Cooling of Trapped Polyatomic Molecules*, Phys. Rev. Lett. **115**, 233001 (2015).

[18] M. Zeppenfeld *et al.*, *Sisyphus cooling of electrically trapped polyatomic molecules*, Nature **491**, 570 (2012).

[19] G. Quéméner and P. S. Julienne, *Ultracold Molecules under Control!*, Chem. Rev. **112**, 4949 (2012).

[20] T. Köhler, K. Góral, and P. S. Julienne, *Production of cold molecules via magnetically tunable Feshbach resonances*, Rev. Mod. Phys. **78**, 1311 (2006).

[21] C. Chin, R. Grimm, P. Julienne, and E. Tiesinga, *Feshbach resonances in ultracold gases*, Rev. Mod. Phys. **82**, 1225 (2010).

[22] K. Bergmann, H. Theuer, and B. W. Shore, *Coherent population transfer among quantum states of atoms and molecules*, Rev. Mod. Phys. **70**, 1003 (1998).

[23] J. G. Danzl *et al.*, *Quantum Gas of Deeply Bound Ground State Molecules*, Science **321**, 1062 (2008).

[24] J. G. Danzl *et al.*, *An ultracold high-density sample of rovibronic ground-state molecules in an optical lattice*, Nat. Phys. **6**, 265 (2010).

[25] F. Lang, K. Winkler, C. Strauss, R. Grimm, and J. H. Denschlag, *Ultracold Triplet Molecules in the Rovibrational Ground State*, Phys. Rev. Lett. **101**, 133005 (2008).

[26] B. Yan *et al.*, *Observation of dipolar spin-exchange interactions with lattice-confined polar molecules*, Nature **501**, 521 (2013).

[27] K. R. A. Hazzard *et al.*, *Many-Body Dynamics of Dipolar Molecules in an Optical Lattice*, Phys. Rev. Lett. **113**, 195302 (2014).

[28] K.-K. Ni *et al.*, *Dipolar collisions of polar molecules in the quantum regime*, Nature **464**, 1324 (2010).

[29] A. Chotia *et al.*, *Long-Lived Dipolar Molecules and Feshbach Molecules in a 3D Optical Lattice*, Phys. Rev. Lett. **108**, 080405 (2012).

[30] C. J. Foot, *Atomic Physics (Oxford Master Series in Atomic, Optical and Laser Physics)*, 1st ed. (Oxford University Press, USA, 2005).

[31] M. D. Di Rosa, *Laser-cooling molecules*, Eur. Phys. J. D **31**, 395 (2004).

[32] B. Hemmerling *et al.*, *Laser slowing of CaF molecules to near the capture velocity of a molecular MOT*, preprint arXiv:1603.02787v1 (2016).

[33] M. T. Hummon *et al.*, *2D Magneto-Optical Trapping of Diatomic Molecules*, Phys. Rev. Lett. **110**, 143001 (2013).

[34] A. L. Collopy, M. T. Hummon, M. Yeo, B. Yan, and J. Ye, *Prospects for a narrow line MOT in YO*, New J. Phys. **17**, 055008 (2015).

[35] B. G. U. Englert *et al.*, *Storage and Adiabatic Cooling of Polar Molecules in a Microstructured Trap*, Phys. Rev. Lett. **107**, 263003 (2011).

[36] A. Prehn, M. Ibrügger, R. Glöckner, G. Rempe, and M. Zeppenfeld, *Optoelectrical Cooling of Polar Molecules to Submillikelvin Temperatures*, Phys. Rev. Lett. **116**, 063005 (2016).

[37] J. Lim, M. D. Frye, J. M. Hutson, and M. R. Tarbutt, *Modeling sympathetic cooling of molecules by ultracold atoms*, Phys. Rev. A **92**, 053419 (2015).

[38] S. Tokunaga *et al.*, *Prospects for sympathetic cooling of molecules in electrostatic, AC and microwave traps*, Eur. Phys. J. D **65**, 141 (2011).

[39] H. J. Metcalf and P. van der Straten, *Laser Cooling and Trapping* (Springer, 2002).

[40] J. L. Carini *et al.*, *Production of ultracold molecules with chirped nanosecond pulses: Evidence for coherent effects*, Phys. Rev. A **87**, 011401 (2013).

[41] J. L. Carini, S. Kallush, R. Kosloff, and P. L. Gould, *Enhancement of Ultracold Molecule Formation Using Shaped Nanosecond Frequency Chirps*, Phys. Rev. Lett. **115**, 173003 (2015).

[42] S. D. Kraft *et al.*, *Formation of ultracold LiCs molecules*, J. Phys. B **39**, S993 (2006).

[43] S. Dutta, J. Lorenz, A. Altaf, D. S. Elliott, and Y. P. Chen, *Photoassociation of ultracold LiRb* molecules: Observation of high efficiency and unitarity-limited rate saturation*, Phys. Rev. A **89**, 020702 (2014).

[44] J. Lorenz, A. Altaf, S. Dutta, Y. P. Chen, and D. S. Elliott, *Formation of deeply bound ultracold LiRb molecules via photoassociation near the* Li $2S_{1/2}$ + Rb $5P_{3/2}$ *asymptote*, Phys. Rev. A **90**, 062513 (2014).

[45] A. Altaf *et al.*, *Formation of ultracold $^7Li\ ^{85}Rb$ molecules in the lowest triplet electronic state by photoassociation and their detection by ionization spectroscopy*, J. Chem. Phys. **142** (2015).

[46] C. Haimberger, J. Kleinert, P. Zabawa, A. Wakim, and N. P. Bigelow, *Formation of ultracold, highly polar $X^1\Sigma^+$ NaCs molecules*, New J. Phys. **11**, 055042 (2009).

[47] D. Wang *et al.*, *Photoassociative Production and Trapping of Ultracold KRb Molecules*, Phys. Rev. Lett. **93**, 243005 (2004).

[48] F. Munchow, C. Bruni, M. Madalinski, and A. Gorlitz, *Two-photon photoassociation spectroscopy of heteronuclear YbRb*, Phys. Chem. Chem. Phys. **13**, 18734 (2011).

[49] K. Aikawa *et al.*, *Coherent Transfer of Photoassociated Molecules into the Rovibrational Ground State*, Phys. Rev. Lett. **105**, 203001 (2010).

[50] A. J. Kerman, J. M. Sage, S. Sainis, T. Bergeman, and D. DeMille, *Production and State-Selective Detection of Ultracold RbCs Molecules*, Phys Rev. Lett. **92**, 153001 (2004).

[51] E. R. Hudson, N. B. Gilfoy, S. Kotochigova, J. M. Sage, and D. DeMille, *Inelastic Collisions of Ultracold Heteronuclear Molecules in an Optical Trap*, Phys. Rev. Lett. **100**, 203201 (2008).

[52] J. M. Sage, S. Sainis, T. Bergeman, and D. DeMille, *Optical Production of Ultracold Polar Molecules*, Phys. Rev. Lett. **94**, 203001 (2005).

[53] S. Jochim *et al.*, *Bose-Einstein Condensation of Molecules*, Science **302**, 2101 (2003).

[54] M. Greiner, C. A. Regal, and D. S. Jin, *Emergence of a molecular Bose-Einstein condensate from a Fermi gas*, Nature **426**, 537 (2003).

[55] M. W. Zwierlein *et al.*, *Observation of Bose-Einstein Condensation of Molecules*, Phys. Rev. Lett. **91**, 250401 (2003).

[56] K. E. Strecker, G. B. Partridge, and R. G. Hulet, *Conversion of an Atomic Fermi Gas to a Long-Lived Molecular Bose Gas*, Phys. Rev. Lett. **91**, 080406 (2003).

[57] J. Cubizolles, T. Bourdel, S. J. J. M. F. Kokkelmans, G. V. Shlyapnikov, and C. Salomon, *Production of Long-Lived Ultracold* Li_2 *Molecules from a Fermi Gas*, Phys. Rev. Lett. **91**, 240401 (2003).

[58] S. Jochim *et al.*, *Pure Gas of Optically Trapped Molecules Created from Fermionic Atoms*, Phys. Rev. Lett. **91**, 240402 (2003).

[59] K. Xu *et al.*, *Formation of Quantum-Degenerate Sodium Molecules*, Phys. Rev. Lett. **91**, 210402 (2003).

[60] C. A. Regal, C. Ticknor, J. L. Bohn, and D. S. Jin, *Creation of ultracold molecules from a Fermi gas of atoms*, Nature **424**, 47 (2003).

[61] S. Dürr, T. Volz, A. Marte, and G. Rempe, *Observation of Molecules Produced from a Bose-Einstein Condensate*, Phys. Rev. Lett. **92**, 020406 (2004).

[62] J. Herbig *et al.*, *Preparation of a Pure Molecular Quantum Gas*, Science **301**, 1510 (2003).

[63] C. Ospelkaus *et al.*, *Ultracold Heteronuclear Molecules in a 3D Optical Lattice*, Phys. Rev. Lett. **97**, 120402 (2006).

[64] A.-C. Voigt *et al.*, *Ultracold Heteronuclear Fermi-Fermi Molecules*, Phys. Rev. Lett. **102**, 020405 (2009).

[65] F. M. Spiegelhalder *et al.*, *All-optical production of a degenerate mixture of* $^6\mathrm{Li}$ *and* $^{40}\mathrm{K}$ *and creation of heteronuclear molecules*, Phys. Rev. A **81**, 043637 (2010).

[66] T. Takekoshi *et al.*, *Towards the production of ultracold ground-state RbCs molecules: Feshbach resonances, weakly bound states, and the coupled-channel model*, Phys. Rev. A **85**, 032506 (2012).

[67] M. P. Köppinger *et al.*, *Production of optically trapped* $^{87}RbCs$ *Feshbach molecules*, Phys. Rev. A **89**, 033604 (2014).

[68] C.-H. Wu, J. W. Park, P. Ahmadi, S. Will, and M. W. Zwierlein, *Ultracold Fermionic Feshbach Molecules of* $^{23}\mathrm{Na}^{40}\mathbf{K}$, Phys. Rev. Lett. **109**, 085301 (2012).

[69] M.-S. Heo *et al.*, *Formation of ultracold fermionic NaLi Feshbach molecules*, Phys. Rev. A **86**, 021602 (2012).

[70] F. Wang *et al.*, *Formation of ultracold NaRb Feshbach molecules*, New J. Phys. **17**, 035003 (2015).

[71] S. Kotochigova, P. S. Julienne, and E. Tiesinga, *Ab initio calculation of the KRb dipole moments*, Phys. Rev. A **68**, 022501 (2003).

[72] S. Stellmer, B. Pasquiou, R. Grimm, and F. Schreck, *Creation of Ultracold* Sr_2 *Molecules in the Electronic Ground State*, Phys. Rev. Lett. **109**, 115302 (2012).

[73] P. S. Zuchowski and J. M. Hutson, *Reactions of ultracold alkali-metal dimers*, Phys. Rev. A **81**, 060703 (2010).

[74] M. Aymar and O. Dulieu, *Calculation of accurate permanent dipole moments of the lowest* $^{1,3}\Sigma^+$ *states of heteronuclear alkali dimers using extended basis sets*, J. Chem. Phys. **122** (2005).

[75] G. Igel-Mann, U. Wedig, P. Fuentealba, and H. Stoll, *Ground-state properties of alkali dimers XY (X, Y=Li to Cs)*, J. Chem. Phys. **84**, 5007 (1986).

[76] J. Deiglmayr, M. Aymar, R. Wester, M. Weidemller, and O. Dulieu, *Calculations of static dipole polarizabilities of alkali dimers: Prospects for alignment of ultracold molecules*, J. Chem. Phys. **129**, (2008).

[77] D. J. McCarron, H. W. Cho, D. L. Jenkin, M. P. Köppinger, and S. L. Cornish, *Dual-species Bose-Einstein condensate of* ^{87}Rb *and* ^{133}Cs, Phys. Rev. A **84**, 011603 (2011).

[78] K.-K. Ni *et al.*, *A High Phase-Space-Density Gas of Polar Molecules*, Science **322**, 231 (2008).

[79] T. Takekoshi *et al.*, *Ultracold Dense Samples of Dipolar RbCs Molecules in the Rovibrational and Hyperfine Ground State*, Phys. Rev. Lett. **113**, 205301 (2014).

[80] P. K. Molony *et al.*, *Creation of Ultracold* ^{87}Rb^{133}Cs *Molecules in the Rovibrational Ground State*, Phys. Rev. Lett. **113**, 255301 (2014).

[81] J. W. Park, S. A. Will, and M. W. Zwierlein, *Ultracold Dipolar Gas of Fermionic* ^{23}Na^{40}K *Molecules in Their Absolute Ground State*, Phys. Rev. Lett. **114**, 205302 (2015).

[82] M. Guo *et al.*, *Creation of an Ultracold Gas of Ground-State Dipolar* ^{23}Na^{87}Rb *Molecules*, Phys. Rev. Lett. **116**, 205303 (2016).

[83] M. Gröbner *et al.*, *A new quantum gas apparatus for ultracold mixtures of K and Cs and KCs ground-state molecules*, J. Mod. Opt. (2016).

[84] S. L. Kemp *et al.*, *Production and characterization of a dual species magneto-optical trap of cesium and ytterbium*, Rev. Sci. Instrum. **87**, 023105 (2016).

[85] M. Borkowski *et al.*, *Scattering lengths in isotopologues of the RbYb system*, Phys. Rev. A **88**, 052708 (2013).

[86] A. Khramov *et al.*, *Ultracold Heteronuclear Mixture of Ground and Excited State Atoms*, Phys. Rev. Lett. **112**, 033201 (2014).

[87] W. Dowd *et al.*, *Magnetic field dependent interactions in an ultracold Li-Yb($^3P_2$) mixture*, New J. Phys. **17**, 055007 (2015).

[88] C. Fellows, R. Gutterres, A. Campos, J. Vergs, and C. Amiot, *The RbCs* $X^1\Sigma^+$ *Ground Electronic State: New Spectroscopic Study*, J. Mol. Spec. **197**, 19 (1999).

[89] C. L. Blackley *et al.*, *Feshbach resonances in ultracold* ^{85}Rb, Phys. Rev. A **87**, 033611 (2013).

[90] H.-W. Cho *et al.*, *Feshbach spectroscopy of an ultracold mixture of* ^{85}Rb *and* ^{133}Cs, Phys. Rev. A **87**, 010703 (2013).

[91] D. J. McCarron, *A Quantum Degenerate Mixture of Rb and Cs*, PhD thesis, Durham University, UK, 2011.

[92] D. L. Jenkin, *Feshbach spectroscopy of an ultracold Rb-Cs mixture*, PhD thesis, Durham University, UK, 2012.

[93] M. P. Köppinger, *Creation of ultracold RbCs molecules*, PhD thesis, Durham University, UK, 2014.

[94] L. P. Yatsenko, V. I. Romanenko, B. W. Shore, and K. Bergmann, *Stimulated Raman adiabatic passage with partially coherent laser fields*, Phys. Rev. A **65**, 043409 (2002).

[95] D. L. Jenkin *et al.*, *Bose-Einstein condensation of* ^{87}*Rb in a levitated crossed dipole trap*, Eur. Phys. J. D **65**, 11 (2011).

[96] H. W. Cho, D. J. McCarron, D. L. Jenkin, M. P. Köppinger, and S. L. Cornish, *A high phase-space density mixture of* ^{87}*Rb and* ^{133}*Cs: towards ultracold heteronuclear molecules*, Eur. Phys. J. D **65**, 125 (2011).

[97] M. L. Harris, *Realisation of a Cold Mixture of Rubidium and Caesium*, PhD thesis, Durham University, UK, 2008.

[98] Y.-J. Lin, A. R. Perry, R. L. Compton, I. B. Spielman, and J. V. Porto, *Rapid production of* ^{87}*Rb Bose-Einstein condensates in a combined magnetic and optical potential*, Phys. Rev. A **79**, 063631 (2009).

[99] T. Wiles, *Dynamics of bright solitary matter-waves*, PhD thesis, Durham University, 2013.

[100] T. Lahaye, C. Menotti, L. Santos, M. Lewenstein, and T. Pfau, *The physics of dipolar bosonic quantum gases*, Rep. Prog. Phys. **72**, 126401 (2009).

[101] A. V. Gorshkov *et al.*, *Tunable Superfluidity and Quantum Magnetism with Ultracold Polar Molecules*, Phys. Rev. Lett. **107**, 115301 (2011).

[102] A. Micheli, G. K. Brennen, and P. Zoller, *A toolbox for lattice-spin models with polar molecules*, Nat. Phys. **2**, 341 (2006).

[103] M. Mayle, B. P. Ruzic, and J. L. Bohn, *Statistical aspects of ultracold resonant scattering*, Phys. Rev. A **85**, 062712 (2012).

[104] K. Bergmann, N. V. Vitanov, and B. W. Shore, *Perspective: Stimulated Raman adiabatic passage: The status after 25 years*, J. Chem. Phys. **142**, 170901 (2015).

[105] J. R. Kuklinski, U. Gaubatz, F. T. Hioe, and K. Bergmann, *Adiabatic population transfer in a three-level system driven by delayed laser pulses*, Phys. Rev. A **40**, 6741 (1989).

[106] U. Gaubatz, P. Rudecki, S. Schiemann, and K. Bergmann, *Population transfer between molecular vibrational levels by stimulated Raman scattering with partially overlapping laser fields. A new concept and experimental results*, J. Chem. Phys. **92**, 5363 (1990).

[107] J. L. Sørensen *et al.*, *Efficient coherent internal state transfer in trapped ions using stimulated Raman adiabatic passage*, New J. Phys. **8**, 261 (2006).

[108] D. Møller, J. L. Sørensen, J. B. Thomsen, and M. Drewsen, *Efficient qubit detection using alkaline-earth-metal ions and a double stimulated Raman adiabatic process*, Phys. Rev. A **76**, 062321 (2007).

[109] M. Hennrich, T. Legero, A. Kuhn, and G. Rempe, *Vacuum-Stimulated Raman Scattering Based on Adiabatic Passage in a High-Finesse Optical Cavity*, Phys. Rev. Lett. **85**, 4872 (2000).

[110] C. D. Panda *et al.*, *Stimulated Raman adiabatic passage preparation of a coherent superposition of ThO* $H^3\Delta_1$ *states for an improved electron electric-dipole-moment measurement*, Phys. Rev. A **93**, 052110 (2016).

[111] S. Longhi, *Adiabatic passage of light in coupled optical waveguides*, Phys. Rev. E **73**, 026607 (2006).

[112] S. Longhi, G. Della Valle, M. Ornigotti, and P. Laporta, *Coherent tunneling by adiabatic passage in an optical waveguide system*, Phys. Rev. B **76**, 201101 (2007).

[113] J. Klein, F. Beil, and T. Halfmann, *Robust Population Transfer by Stimulated Raman Adiabatic Passage in a* Pr^{3+}:$\mathrm{Y_2SiO_5}$ *Crystal*, Phys. Rev. Lett. **99**, 113003 (2007).

[114] J. Klein, F. Beil, and T. Halfmann, *Experimental investigations of stimulated Raman adiabatic passage in a doped solid*, Phys. Rev. A **78**, 033416 (2008).

[115] B. Bransden and C. Joachain, *Physics of Atoms and Molecules* (Prentice Hall, 2003).

[116] B. P. Straughan and S. Walker, *Spectroscopy* volume 2 (Chapman and Hall, 1976).

[117] J. M. Hollas, *Modern Spectroscopy* (Wiley, 2003).

[118] J. M. Brown and A. Carrington, *Rotational spectroscopy of diatomic molecules* (Cambridge University Press, 2003).

[119] W. Stwalley, *Efficient conversion of ultracold Feshbach-resonance-related polar molecules into ultracold ground state* $(^1\Sigma^+, v = 0, J = 0)$ *molecules*, Eur. Phys. J. D **31**, 221 (2004).

[120] S. Kotochigova and E. Tiesinga, *Ab initio relativistic calculation of the RbCs molecule*, J. Chem. Phys. **123**, (2005).

[121] M. Debatin, *Creation of Ultracold RbCs Ground-State Molecules*, PhD thesis, University of Innsbruck, 2013.

[122] A. Stalyarov, personal communication, 2015.

[123] S. N. Yurchenko, L. Lodi, J. Tennyson, and A. V. Stolyarov, *Duo: A general program for calculating spectra of diatomic molecules*, Comp. Phys. Comm. **202**, 262 (2016).

[124] W. Demtröder, *Atoms, Molecules, and Photons* (Springer, 2006).

[125] D. A. Jennings *et al.*, *High-resolution spectroscopy of HF from* 40 *to* 1100 cm^{-1}*: Highly accurate rotational constants*, J. Mol. Spec. **122**, 477 (1987).

[126] J. Aldegunde, B. A. Rivington, P. S. Żuchowski, and J. M. Hutson, *Hyperfine energy levels of alkali-metal dimers: Ground-state polar molecules in electric and magnetic fields*, Phys. Rev. A **78**, 033434 (2008).

[127] A. L. Marchant, S. Händel, S. A. Hopkins, T. P. Wiles, and S. L. Cornish, *Bose-Einstein condensation of* ^{85}*Rb by direct evaporation in an optical dipole trap*, Phys. Rev. A **85**, 053647 (2012).

[128] K. E. Strecker, G. B. Partridge, A. G. Truscott, and R. G. Hulet, *Formation and propagation of matter-wave soliton trains*, Nature **417**, 150 (2002).

[129] A. L. Marchant *et al.*, *Controlled formation and reflection of a bright solitary matter-wave*, Nat. commun. **4**, 1865 (2013).

[130] J. M. Hutson, BOUND computer program, version 5 , distributed by Collaborative Computational Project No. 6 of the EPSRC (1993).

[131] J. M. Hutson, *FIELD computer program, version 1*, 2011.

[132] H. T. C. Stoof, J. M. V. A. Koelman, and B. J. Verhaar, *Spin-exchange and dipole relaxation rates in atomic hydrogen: Rigorous and simplified calculations*, Phys. Rev. B **38**, 4688 (1988).

[133] J. M. Hutson and S. S. Greene, MOLSCAT computer program, version 14 , distributed by Collaborative Computational Project No. 6 of the EPSRC (1994).

[134] M. L. González-Martínez and J. M. Hutson, *Ultracold atom-molecule collisions and bound states in magnetic fields: Tuning zero-energy Feshbach resonances in He-NH* ($^3\Sigma^-$), Phys. Rev. A **75**, 022702 (2007).

[135] R. Vexiau *et al.*, *Optimal trapping wavelengths of* Cs_2 *molecules in an optical lattice*, Eur. Phys. J. D **65**, 243 (2011).

[136] R. Grimm, M. Weidemüller, and Y. B. Ovchinnikov, *Optical Dipole Traps for Neutral Atoms*, volume 42 of *Advances In Atomic, Molecular, and Optical Physics*, pp. 95 – 170, Academic Press, 2000.

[137] O. Dulieu, personal communication, 2014.

[138] O. Morsch and M. Oberthaler, *Dynamics of Bose-Einstein condensates in optical lattices*, Rev. Mod. Phys. **78**, 179 (2006).

[139] D. R. Meacher, *Optical lattices-crystalline structures bound by light*, Contemp. Phys. **39**, 329 (1998).

[140] K. Aikawa *et al.*, *Narrow-linewidth light source for a coherent Raman transfer of ultracold molecules*, Opt. Express **19**, 14479 (2011).

[141] U. Schünemann, H. Engler, R. Grimm, M. Weidemüller, and M. Zielonkowski, *Simple scheme for tunable frequency offset locking of two lasers*, Rev. Sci. Instrum. **70**, 242 (1999).

[142] M. Debatin *et al.*, *Molecular spectroscopy for ground-state transfer of ultracold RbCs molecules*, Phys. Chem. Chem. Phys. **13**, 18926 (2011).

[143] E. D. Black, *An introduction to Pound-Drever-Hall laser frequency stabilization*, Am. J. Phys. **69**, 79 (2001).

[144] W.-K. Lee, H. S. Moon, and H. S. Suh, *Measurement of the absolute energy level and hyperfine structure of the* ^{87}Rb $4D_{5/2}$ *state*, Opt. Lett. **32**, 2810 (2007).

[145] H. S. Moon, W. K. Lee, L. Lee, and J. B. Kim, *Double resonance optical pumping spectrum and its application for frequency stabilization of a laser diode*, Appl. Phys. Lett. **85**, 3965 (2004).

[146] T. Okoshi, K. Kikuchi, and A. Nakayama, *Novel method for high resolution measurement of laser output spectrum*, Electron. Lett. **16**, 630 (1980).

[147] L. Richter, H. Mandelberg, M. Kruger, and P. McGrath, *Linewidth determination from self-heterodyne measurements with subcoherence delay times*, IEEE J. Quant. Electron. **22**, 2070 (1986).

[148] G. D. Domenico, S. Schilt, and P. Thomann, *Simple approach to the relation between laser frequency noise and laser line shape*, Appl. Opt. **49**, 4801 (2010).

[149] T. Puppe *et al.*, *Characterization of a DFG comb showing quadratic scaling of the phase noise with frequency*, Opt. Lett. **41**, 1877 (2016).

[150] F. Lang *et al.*, *Dark state experiments with ultracold, deeply-bound triplet molecules*, Farad. Discuss. **142**, 271 (2008).

[151] M. J. Mark *et al.*, *Dark resonances for ground-state transfer of molecular quantum gases*, Appl. Phys. B **95**, 219 (2009).

[152] Y. Yang, X. Liu, Y. Zhao, L. Xiao, and S. Jia, *Rovibrational Dynamics of RbCs on its Lowest 1,3+ Potential Curves Calculated by Coupled Cluster Method with All-Electron Basis Set*, J. Phys. Chem. A **116**, 11101 (2012).

[153] K.-K. Ni, *A Quantum Gas Of Polar Molecules*, PhD thesis, University of Colorado, USA, 2009.

[154] N. Kosugi, S. Matsuo, K. Konno, and N. Hatakenaka, *Theory of damped Rabi oscillations*, Phys. Rev. B **72**, 172509 (2005).

[155] A. Daniel *et al.*, *Damping of local Rabi oscillations in the presence of thermal motion*, Phys. Rev. A **87**, 063402 (2013).

[156] D. A. Steck, *Rubidium 87 D Line Data,* available online `http://steck.us/alkalidata` (revision 2.1.4), 2010.

[157] J. Johansson, P. Nation, and F. Nori, *QuTiP 2: A Python framework for the dynamics of open quantum systems*, Comput. Phys. Commun. **184**, 1234 (2013).

[158] P. D. Gregory *et al.*, *A simple, versatile laser system for the creation of ultracold ground state molecules*, New J. Phys. **17**, 055006 (2015).

[159] H. Telle, *EP1594020 - Method for generating an offset-free optical frequency comb and laser apparatus therefor*, 2005.

[160] T. Fuji, A. Apolonski, and F. Krausz, *Self-stabilization of carrier-envelope offset phase by use of difference-frequency generation*, Opt. Lett. **29**, 632 (2004).

[161] E. Benkler, H. R. Telle, A. Zach, and F. Tauser, *Circumvention of noise contributions in fiber laser based frequency combs*, Opt. Express **13**, 5662 (2005).

[162] S. Bize *et al.*, *High-accuracy measurement of the ^{87}Rb ground-state hyperfine splitting in an atomic fountain*, EPL **45**, 558 (1999).

[163] P. J. Mohr, D. B. Newell, and B. N. Taylor, *CODATA Recommended Values of the Fundamental Physical Constants: 2014*, preprint arXiv:1507.07956 (2014).

[164] J. Liu *et al.*, *Determination of the ionization and dissociation energies of the hydrogen molecule*, J. Chem. Phys. **130**, 174306 (2009).

[165] D. Sprecher, C. Jungen, W. Ubachs, and F. Merkt, *Towards measuring the ionisation and dissociation energies of molecular hydrogen with sub-MHz accuracy*, Farad. discuss. **150**, 51 (2011).

[166] D. Fehrenbacher *et al.*, *Free-running performance and full control of a passively phase-stable Er:fiber frequency comb*, Optica **2**, 917 (2015).

[167] D. DeMille *et al.*, *Enhanced Sensitivity to Variation of m_e/m_p in Molecular Spectra*, Phys. Rev. Lett. **100**, 043202 (2008).

[168] T. Zelevinsky, S. Kotochigova, and J. Ye, *Precision Test of Mass-Ratio Variations with Lattice-Confined Ultracold Molecules*, Phys. Rev. Lett. **100**, 043201 (2008).

[169] E. Reinhold *et al.*, *Indication of a Cosmological Variation of the Proton-Electron Mass Ratio Based on Laboratory Measurement and Reanalysis of* H_2 *Spectra*, Phys. Rev. Lett. **96**, 151101 (2006).

[170] E. R. Hudson, H. J. Lewandowski, B. C. Sawyer, and J. Ye, *Cold Molecule Spectroscopy for Constraining the Evolution of the Fine Structure Constant*, Phys. Rev. Lett. **96**, 143004 (2006).

[171] S. Truppe *et al.*, *A search for varying fundamental constants using hertz-level frequency measurements of cold CH molecules*, Nat. Commun. **4**, 2600 (2013).

[172] B. H. McGuyer *et al.*, *High-precision spectroscopy of ultracold molecules in an optical lattice*, New J. Phys. **17**, 055004 (2015).

[173] B. H. McGuyer *et al.*, *Precise study of asymptotic physics with subradiant ultracold molecules*, Nat Phys **11**, 32 (2015).

[174] S. Taie, S. Watanabe, T. Ichinose, and Y. Takahashi, *Feshbach-Resonance-Enhanced Coherent Atom-Molecule Conversion with Ultranarrow Photoassociation Resonance*, Phys. Rev. Lett. **116**, 043202 (2016).

[175] I. G. Hughes and T. P. A. Hase, *Measurements and their uncertainties: a practical guide to modern error analysis* (Oxford University Press, 2010).

[176] T. J. Kane and R. L. Byer, *Monolithic, unidirectional single-mode Nd:YAG ring laser*, Opt. Lett. **10**, 65 (1985).

[177] M. S. Safronova, B. Arora, and C. W. Clark, *Frequency-dependent polarizabilities of alkali-metal atoms from ultraviolet through infrared spectral regions*, Phys. Rev. A **73**, 022505 (2006).

[178] T. Lauber, J. Küber, O. Wille, and G. Birkl, *Optimized Bose-Einstein-condensate production in a dipole trap based on a 1070-nm multifrequency laser: Influence of enhanced two-body loss on the evaporation process*, Phys. Rev. A **84**, 043641 (2011).

[179] P. Kwee *et al.*, *Stabilized high-power laser system for the gravitational wave detector advanced LIGO*, Opt. Express **20**, 10617 (2012).

[180] LIGO Scientific Collaboration and Virgo Collaboration, B. P. Abbott *et al.*, *Observation of Gravitational Waves from a Binary Black Hole Merger*, Phys. Rev. Lett. **116**, 061102 (2016).

[181] S. Friebel, C. D'Andrea, J. Walz, M. Weitz, and T. W. Hänsch, CO_2*-laser optical lattice with cold rubidium atoms*, Phys. Rev. A **57**, R20 (1998).

[182] J. H. Denschlag *et al.*, *A Bose-Einstein condensate in an optical lattice*, J. Phys. B **35**, 3095 (2002).

[183] R. E. Sapiro, R. Zhang, and G. Raithel, *Atom interferometry using Kapitza-Dirac scattering in a magnetic trap*, Phys. Rev. A **79**, 043630 (2009).

[184] R. E. Sapiro, *Bose-Einstein condensate experiments in optical lattices*, PhD thesis, The University of Michigan, 2010.

[185] P. L. Gould, G. A. Ruff, and D. E. Pritchard, *Diffraction of atoms by light: The near-resonant Kapitza-Dirac effect*, Phys. Rev. Lett. **56**, 827 (1986).

[186] Y. B. Ovchinnikov *et al.*, *Diffraction of a Released Bose-Einstein Condensate by a Pulsed Standing Light Wave*, Phys. Rev. Lett. **83**, 284 (1999).

[187] G. K. Campbell *et al.*, *Photon Recoil Momentum in Dispersive Media*, Phys. Rev. Lett. **94**, 170403 (2005).

[188] H. K. Andersen, *Bose-Einstein condensates in optical lattices*, PhD thesis, Quantop, Department of Physics and Astronomy, University of Aarhus, 2008.

[189] M. Greiner, *Ultracold quantum gases in three-dimensional optical lattice potentials*, PhD thesis, LMU, 2003.

[190] C. Kittel, *Introduction to solid state physics* (Wiley, 2005).

[191] E. Jones *et al.*, *SciPy: Open source scientific tools for Python*, 2001–, [Online; accessed 2016-02-12].

[192] M. Greiner, I. Bloch, O. Mandel, T. W. Hänsch, and T. Esslinger, *Bose–Einstein condensates in 1D- and 2D optical lattices*, Appl. Phys. B **73**, 769 (2001).

[193] Y. B. Band, M. Trippenbach, J. P. Burke, and P. S. Julienne, *Elastic Scattering Loss of Atoms from Colliding Bose-Einstein Condensate Wave Packets*, Phys. Rev. Lett. **84**, 5462 (2000).

[194] A. P. Chikkatur *et al.*, *Suppression and Enhancement of Impurity Scattering in a Bose-Einstein Condensate*, Phys. Rev. Lett. **85**, 483 (2000).

[195] S. Ospelkaus *et al.*, *Controlling the Hyperfine State of Rovibronic Ground-State Polar Molecules*, Phys. Rev. Lett. **104**, 030402 (2010).

[196] S. A. Will, J. W. Park, Z. Z. Yan, H. Loh, and M. W. Zwierlein, *Coherent Microwave Control of Ultracold* ^{23}Na^{40}K *Molecules*, Phys. Rev. Lett. **116**, 225306 (2016).

[197] M. Deis *et al.*, *Polarizability of ultracold* Rb_2 *molecules in the rovibrational ground state of* $a^3\Sigma_u^+$, New J. Phys. **17**, 065019 (2015).

[198] S. Händel, A. L. Marchant, T. P. Wiles, S. A. Hopkins, and S. L. Cornish, *Magnetic transport apparatus for the production of ultracold atomic gases in the vicinity of a dielectric surface*, Rev. Sci. Instrum. **83** (2012).

[199] L. W. Cheuk *et al.*, *Quantum-Gas Microscope for Fermionic Atoms*, Phys. Rev. Lett. **114**, 193001 (2015).